Ultrafast laser-induced nanostructuring of metals in regular patterns

Chen Li

Jean Monnet University – Saint-Étienne

Ultrafast laser-induced nanostructuring of metals in regular patterns

by

Chen LI

Thesis presented in partial fulfillment of the requirements for
the degree of Doctor of Philosophy
in the subject of Optics, photonics and hyperfrequencies.

Defended on the 22 May 2016 before the committee:

Prof. Yong-feng LU	(University of Nebraska-Lincoln, USA)	President
Prof. Ya CHENG	(East China Normal University)	Rapporteur
Prof. Tian-qing JIA	(East China Normal University)	Rapporteur
Dr. Jean-Philippe COLOMBIER	(Jean Monnet University, Saint-Étienne)	Examinator
Prof. Jianjun YANG	(Nankin University)	Examinator
Prof. Guanghua CHENG	(University of Chinese Academy of Sciences, XIOPM)	Co-director
Dr. Razvan STOIAN	(Jean Monnet University, Saint-Étienne)	Director
Dr. Wen-hui FAN	(University of Chinese Academy of Sciences, XIOPM)	Invited
Prof. Qing Pan	(National Natural Science Foundation of China)	Invited

Université Jean Monnet – Saint-Étienne

L'école doctorale "Sciences, Ingénierie, Santé"

Nanostructuration des métaux par motifs réguliers induits par laser ultrabref

par

Chen LI

Thése présentée pour obtenir le grade de Docteur en Sciences en spécialité Optique, photonique et hyperfréquences.

Soutenue le 22 Mai 2016 devant le jury composé de:

Prof. Yong-feng LU	(Université Nebraska-Lincoln, USA)	President
Prof. Ya CHENG	(Université normale de la Chine de l'Est)	Rapporteur
Prof. Tian-qing JIA	(Université normale de la Chine de l'Est)	Rapporteur
Dr. Jean-Philippe COLOMBIER	(Université Jean Monnet, Saint-Étienne)	Examinateur
Prof. Jianjun YANG	(Université Nankin)	Examinateur
Prof. Guanghua CHENG	(Université de l'Académie chinoise des sciences , XIOPM)	Co-directeur
Dr. Razvan STOIAN	(Université Jean Monnet, Saint-Étienne)	Directeur
Dr. Wen-hui FAN	(Université de l'Académie chinoise des sciences, XIOPM)	Invité
Prof. Qing Pan	(Fondation nationale des sciences naturelles de Chine)	Invité

Abstract

Femtosecond laser-induced periodic surface structures (fs-LIPSS) attract the scientific and technical attention due to the ability to produce nanostructures below the optical wavelength. These are essential for surface engineering and treatment, notably in tribology, wettability, mechanics, marking and counterfeiting. Depending on the regime of laser interaction, particularly on the laser fluence, pulse number and material type, ultrashort pulses can induce the low- and high-spatial-frequency-LIPPS (LSFL and HSFL), with the orientation perpendicular ($\perp$E) or parallel ($\parallel$E) to the laser polarization. Considering their potential in the nano-manufacturing, this work focuses on potential mechanisms for LIPSS formation, especially HSFL formation on the metallic alloys.

In order to investigate the transient optical indices of excited materials in fs-LIPSS formation, we first developed time-resolved ellipsometry to measure dynamic optical indices of excited materials. Thus we gain insights in the dynamics of the dielectric function where this is intrinsically related to the electronic configuration and lattice structure. First principle simulations are then used to reveal how the electronic configuration changes during the excitation, responsible for the transient optical indices. The effects of transient optical indices are considered in the LIPSS formation mechanisms.

Based on the experiments of fs-LIPSS formations on six different materials, involving metal tungsten, semiconductor silicon, dielectric fused silica, single-crystal superalloy CMSX-4, amorphous alloy Zr-BMG and its corresponding crystal alloy Zr-CA, we investigate the LIPSS formation mechanisms in the electromagnetic domain by finite-difference time-domain (FDTD) simulations, related to the electromagnetic energy distribution followed by the dynamics of optical excitation, evolving topologies with pulse number and materials.

We focus on the electromagnetic origin of LIPSS formation and reveal a potential primary factor for LIPSS formation. LIPSS formation can be explained by deposited energy modulation on surface via electromagnetic effects. The energy modulation mainly comes from the interference between incident laser and scattered surface wave (for LSFL($\perp$E)), being complemented by the interference between scattered surface waves (for HSFL($\perp$E)). Specially, for HSFL ($\parallel$E) on Zr-CA, we proposed that the formation scenarios rely on individual anisotropic field-enhancement processes. The evolving surface topology with laser pulse number leads to a feedback-driven energy modulation deposited on surface.

Résumé

Les structures périodiques de surface induites par laser femtoseconde(fs-LIPSS) attirent l'attention scientifique et technique en raison de la possibilité de produire des nanostructures en dessous de la longueur d'onde optique. Ces éléments sont essentiels pour l'ingénierie de surface et les procédés, notamment en tribologie, mouillabilité, la mécanique, le marquage et la lutte contre la contrefaçon. Selon le régime d'interaction laser, en particulier la fluence du laser, le nombre d'impulsionset le type de matériaux, les impulsions ultracourtes peuvent induire des basses et des hautes fréquences spatiales-LIPSS (LSFL et HSFL), avec l'orientation perpendiculaire ($\perp$E) ou parallèle ($\parallel$ E) à la polarisation du laser. Compte tenu de leur potentiel pour la nano-fabrication, ce travail se concentre sur les mécanismes potentiels de formation des LIPSS, en particulier la formation des HSFL sur les alliages métalliques.

Afin d'étudier les indices optiques transitoires de matériaux excités dans la formation fs-LIPSS, nous avons d'abord développé de l'ellipsométrie résolue en temps afin de mesurer les indices optiques dynamiques des matériaux excités. Ainsi, nous avons obtenu un aperçu de la dynamique de la fonction diélectrique intrinsèquement liée à la configuration électronique et au réseau cristallin. Des simulations de premiers principes sont ensuite utilisées pour révéler la façon dont la configuration électronique change au cours de l'excitation, responsable d'indices optiques transitoires. Les effets des indices optiques transitoires sont pris en compte dans les mécanismes de formation de LIPSS.

Sur la base d'expériences de formations des fs-LIPSS sur six matériaux différents, incluant du tungstène métallique, du silicium semiconducteur, de la silice fondue diélectrique,unsuperalliage monocristallin CMSX-4, un alliage amorphe de Zr-BMG et son alliage cristallin correspondant Zr-CA, nous étudions les mécanismes de formation des LIPSS dans le domaine électromagnétique par des simulations de différences finies dans le domaine temporel (FDTD), liées à la distribution d'énergie électromagnétique suivie par la dynamique de l'excitation optique et par l'évolution dela topologie avec le nombre d'impulsions et les matériaux.

Nous nous concentrons sur l'origine électromagnétique de la formation des LIPSS et révélons un facteur principal potentiel de leur formation. Elle peut être expliquée par la modulation de l'énergie déposée sur la surface par des effets électromagnétiques. La modulation de l'énergie provient principalement de l'interférence

entre le laser incident et les ondes de surface diffusées (pour LSFL (⊥ E)), complétée par l'interférence entre les ondes de surface diffusées (pour HSFL (⊥E)). Spécialement, pour HSFL (∥ E) sur Zr-CA, nous avons proposé que les scénarios de formation reposent sur des processus individuels d'exaltation anisotrope du champ. La topologie de surface, évoluant avec le nombre d'impulsions laser,induit une modulation d'énergie déposée sur la surface définieet amplifiée par la rétroaction.

Contents

the groove · 114
6.5.3 FDTD simulations on the effect of a linear groove · 115
6.6 FDTD simulation for HSFL formation · · · · · · · · · · 118
6.6.1 HSFL(⊥E) on CMSX-4 · · · · · · · · · · · · · · · · · 118
6.6.2 HSFL (∥E) on CA · 122
6.7 FDTD simulation for LIPSS formation on fused silica · 130
6.8 Conclusion · 132

7 Conclusions and perspectives **135**
7.1 Conclusion · 135
7.2 Perspectives · 137

Bibliography **139**

Chapter 1

Introduction

Nanomanufacturing is the industrial-scale manufacture of nanotechnology-based objects, with emphasis on low cost and reliability. This involves scaled-up, reliable, and cost-effective manufacturing of nanoscale materials, structures, devices, and systems. Nanomanufacturing can improve the properties of materials, making them stronger, lighter, more durable, with new functions and capacities. In case of surface relevant examples include water-repellent, anti-reflective, self-cleaning, ultraviolet- or infrared-resistant, antifog, antimicrobial, scratch-resistant, electrically conductive functionalized surface and so on [NNI16]. Among nanomanufacturing technologies, ultrafast lasers offer an excellent capacity for time-effective fabrication, provided that the nanoscale can be reliably achieved.

Since the invention of the laser in 1960 [Mai60], laser sources showed a rapid and continuous development. Now laser sources can achieve a wide range of wavelengths from ultraviolet to infrared, output modes from continuous wave to ultrashort pulses, and even ultra-high peak powers of 10^{22} W/cm^2, up to the field of relativistic optics. Due to the multiple choices in the large domain of energy, time and space, laser can satisfy the requirement of the manufacturing in the range of macro-scale. Among several laser sources of choice, ultrafast lasers, especially the femtosecond lasers (fs), created a new scientific field devoted to ultrafast phenomena. This investigates atomic motion, phase transitions or the formation and breaking of chemical bonds in the time domain of electronic excitation, beyond the more standard equilibrium aspects of physics, chemistry and biology. Due to the ultrafast characteristic, fs laser pulses directly excite the electronic system which occurs much faster than the relaxation in the atomic system. The specific time decoupling between excitation and relaxation allows to precisely control the interaction and to produce modifications on a micro scale. Alongside nonlinear aspects, this is equally the prerequisite of bypassing the diffraction limit and achieving nanoscale fabrication.

As a consequence of its ultrashort pulse duration, fs laser allows to concentrate laser energy of only few μJ to intensity values of tens of TW/cm^2, beyond the destruction threshold of any material. Furthermore, the high intensities of fs laser open the way to examine previously unknown phenomena.

In the field of manufacturing, fs laser has several advantages: Almost all the solid materials can be structured with femtosecond lasers, such as metals, semiconductors, dielectrics, polymers, or biological tissues, no matter if the solid material is transparent or opaque, hard or fragile; Because the surrounding areas in the fs laser machining are not affected, the post-processing is not needed; A variety of micro-scale and nano-scale structures can be fabricated in one-step procedure, for example, holes, grooves and laser induced periodic surface structure (LIPSS). More recently, with the increase of mean output power in commercial fs lasers, fs laser becomes an important instrument for nanomanufacturing in the industry [Wan11].

A major axis in the research field of ultrafast laser nanomanufacturing is the material surface processing. A variety of precise micro-scale and nano-scale structures can be fabricated by fs laser ablation on surfaces, given the ability to localize energy on scales similar to the radiation wavelength. A prominent example is the spectacular appearance of laser induced periodic surface structures (LIPSS) seen as a grating-like damage on the material surface irradiated with spatially and temporally coherent sources. Observed almost 50 years ago [Bir65], they are today subject of increased attention due to a number of scientific and technological reasons, among them their universality and ability to localize energy below the optical wavelength. LIPSS are generally scaling with the laser wavelength, though several classes of periodicities are observed [BMJ$^+$14, SYP$^+$83, BRK11], and mostly respond and align according to the direction of the exciting electric field. LIPSS provides a fast, precise and low-cost tool for surface micro/nano-structuring. From a practical view, the generation of regular nanoscale pattern in LIPSS can have applications in surface engineering and treatment, notably in tribology, wettability, mechanics, marking and counterfeiting [VG13, HVG12, DSS$^+$10, BKH$^+$15]. Given their potential in functionalizing materials, this work will focus on potential mechanisms for LIPSS formation.

The formation mechanism of LIPSS and their similitude with nanopatterns generated by other forms of irradiation (e.g. ion beams [VRV$^+$15]) or with natural upscale phenomena are still under debate, putting forward the challenge of bringing together coherent irradiation-related features and non-coherent growth mechanisms and material movement. Several mechanisms were suggested to explain the formation of LIPSS, including probably the most comprehensive approach-the generalized scattering and interference (Sipe) model [SYP$^+$83], optical transients models coupled to the scattering approach [BRK11], surface plasmon polariton (SPP) mediated LIPSS formation [MM08, DTS$^+$12, OTN$^+$11, MM12], or

macroscopic self-organization of unstable matter [VRV+15]. They involve optical coupling via transient optical indices, the onset of scattering sources and energy deposition with the fulfillment of synchronism and conservation laws, leading eventually to an ordered material movement. A hypothesis with a large acceptance is based on the interference of the incident laser radiation with surface-scattered electromagnetic waves, which, in the case of metals may take the form of surface plasmon polaritons [BRK11, OTN+11], but other forms of scattered waves are not excluded (note the existence of electromagnetic field structures " radiation remnants " in the Sipe model [SYP+83]). SPP induced formation theory is based on the interference of the incident laser field with laser induced SPPs for metals, however, SPPs are excited under the condition of phase-matching, difficult to fulfill for flat surfaces or for a range of materials where the optical indices do not support SPP. From here appears the necessity of taking into consideration the role of residual roughness [SRO+12, AKO+14] and, equally, its generation and evolution with laser irradiation, notably its role in assisting fulfilling momentum conservation laws for a large range of wave vectors but equally the role of individual scattering centers.

The present work aims at responding to questions related to electromagnetic energy distribution and will focus on the dynamics of optical excitation, evolving topologies with irradiation dose, and electromagnetic simulations. Several materials mapping metallic, semiconducting and dielectric behaviors are used; emphasizing as well multielement materials and particularly alloys in amorphous and crystalline states.

In order to investigate the transient optical indices of excited materials in LIPSS formation, we first developed time-resolved techniques to follow dynamics of excited materials. Thus we gain insights in the dynamics of the dielectric function where this is intrinsically related to the electronic configuration and lattice structure. First principle simulations are then used to reveal how the electronic configuration changes during the excitation, responsible for the transient optical indices.

Observing the LIPSS formation mechanisms, experiments of ripples formation on metal, semiconductor and dielectrics were carried out. Then the morphology of LIPSS is observed and analyzed to investigate the role of surface micro/nano-structures in the LIPSS formation.).

The first question relates to the distribution of electromagnetic energy on surfaces. In order to investigate the role of micro/nano-structures in LIPSS formation, finite-difference time-domain (FDTD) method [Yee66] is used to calculate the inhomogeneous electromagnetic energy distribution on surface. A comparative view is given with respect to the traditional Sipe model. In the electromagnetic domain, LIPSS formation originates from the interference between all kinds of electromagnetic waves on surface, including surface scattered wave, incident laser, surface plasmon polaritons (SPP) and composite diffractive evanescent wave [GA06, LM7]. We have tried to elucidate the main scattering phenomena leading to LIPSS. Scattered electromagnetic wave (SEW) originates

from the nano-protuberances on surface, emulated here as nanoparticles on surface. The scattering characteristics of nanoparticles in different materials led us to associate scattering to surface rough topologies and to indicate the role of localized surface plasmons (LSP) on metal nanoparticles [Mai07]. Several geometries allowed us to build coherent scattering scenarios for overall modulated energy fields. Particular paths to low- and high-spatial-frequency-LIPPS (LSFL and HSFL) formation are outlined.

The thesis is structured as follows:

Chapter 2 reviews general aspects of laser-induced periodic surface structures (LIPSS). At first we review LIPSS reported on different solids upon near-infrared fs-laser pulse irradiation. However, LIPSS formation mechanisms are not yet fully understood and still under debate until now and we draw attention on the open questions in the field. Several LIPSS formation theories with merits and defects are introduced, including Sipe theory, FDTD-EM approach, self-organization model of unstable matter and LIPSS formation respectively mediated with surface plasmon polariton (SPP), second harmonic generation (SHG) as well as transient optical properties during irradiation. We equally introduce material transformations under LIPSS, related to the permanent changes of the material in the chemistry, composition, crystal structure and surface morphology. At last, we show the applications of LIPSS in material surface processing, including surface wetting, tribology, modification of optical properties, marking and coding, light trapping and emitting, as well as bio-medical application.

In Chapter 3, we review main physical phenomena in laser ablation related to electronic excitation and relaxation. With a focus on optical coupling, at first we introduce the optical properties of solids briefly. Next, we discuss various complex processes in the ultrafast laser-matter interaction. Then the transient responses of metals and semiconductors to ultrafast laser are reviewed to show the complex processes related to the electronic configuration and lattice structure, such as the photo-excitation of s/p- and d-electrons, electron-electron thermalization, intraband and interband transitions, changes of electronic configuration, electron-lattice thermalization, lattice disorder and so on.

In Chapter 4, the experimental system of time-resolved ellipsometry is built and experimental details are introduced. Finally, the measured results on the dielectric functions and optical dynamics of single-crystal silicon, tungsten and Zr-based bulk metal glass (Zr-BMG) are introduced and discussed respectively.

Chapter 5 describes the experiments of fs-LIPSS on six different materials, involving metal tungsten, semiconductor silicon, dielectric fused silica, single-crystal superalloy CMSX-4, amorphous alloy Zr-BMG and its corresponding crystal alloy Zr-CA. Then the morphology of LIPSS is observed and analyzed with scanning electron microscopy (SEM) and atomic force microscope (AFM). In addition, for Zr-BMG, the structural changes within LIPSS are measured by electron back-scatter diffraction (EBSD). Finally, LIPSS characteristics for six materials are respectively analyzed and summarized, providing the experimental results for the investigating the LIPSS formation mechanism.

In Chapter 6, at first, FDTD method is briefly introduced and then it is used to simulate the case of Sipe theory. Secondly, localized surface plasmons in nanostructures, their effect on scattering electromagnetic wave, as well as the roles of micro/ nano-structures in LIPSS formation are introduced and analyzed by FDTD simulations. Next, the formation mechanisms of LSFL and HSFL on several superalloys are respectively analyzed and discussed. Finally, LIPSS formation on fused silica is analyzed by FDTD simulations.

Finally, the conclusion part of Chapter 7 resumes the main experimental results and the discussion section, putting forward a synthesis of the proposed LIPSS formation scenarios. The perspectives section offers an emphasis on the fundamental questions about the experiments and FDTD simulations regarding LIPSS formations, as well as on the associated applications as well.

Chapter 2

General aspects of LIPSS

In this chapter, general aspects of laser-induced periodic surface structures (LIPSS) are introduced. At first we discuss various complex processes in the ultrafast laser-matter interaction. We underline the role of optical and structural transients and their role in ripple formation. Selected types of LIPSS reported on different solids upon near-infrared fs-laser pulse irradiation are summarized. Then several LIPSS formation theories with their merits and defects are discussed. Next, we introduce material transformations under LIPSS, related to the permanent changes of the material in the chemistry, composition, crystal structure and surface morphology. Finally, we review some potential applications of LIPSS in material surface processing and consequences in optics and mechanics.

2.1 Introduction of LIPSS

The laser induced periodic surface structures (LIPSS) represent a regular succession of structures resembling a grating arrangement, spontaneously generated by coherent laser radiation on material surfaces; some examples of LIPSS are shown in Fig. 2.1. In 1965, Birnbaum firstly observed the phenomenon of ripples induced by a ruby laser on semiconductor surfaces， which is consisted of regular patterns of cracks and a system of parallel grooves (spacing of about 1 μm) [Bir65]. This was the beginning of a prolific research field with respect to formation mechanisms and applications fields. In the following years LIPSS were created and observed on many kinds of solid materials for a range of laser pulse durations. This suggests that we are in the presence of a universal phenomenon induced by light,

forming equally the object of study of this work. More recently, ultrashort pulsed radiation has received a specific attention for its potential in determining rippled surfaces, following the idea that nonlinear excitation and electronic non-equilibrium can induce novel interaction features. In particular, femtosecond (fs) laser-induced ripples show a range of orientation and periodicities that go on scales, much smaller than laser wavelength [BNJ14]. Under the ultrafast laser ablation in the range from femtosecond to picosecond laser, we observe several types of regular ripple patterns: low-spatial-frequency LIPSS (LSFL), high-spatial-frequency LIPSS (HSFL), with the different orientation parallel ($\parallel$E) or perpendicular ($\perp$E) to the laser polarization. They appear on a wide range of materials depending on irradiation conditions and some indicative examples are pointed below. For example in Fig 2.1, LSFL($\perp$E) exist widely on metal tungsten, semiconductor single crystal silicon, bulk metal glass (BMG), crystal alloy (CA) from BMG and the superalloy CMSX-4. They characterize mostly metallic and low-bandgap materials. LSFL($\parallel$E) exist on a range of dielectrics and we observed them on fused silica (Fig. 2.1(c)). High spatial frequency structures are equally reported on various materials with periodicities (down to 100 nm), HSFL($\parallel$E) exist on the CA (Fig. 2.1(e)). Fig. 2.1(f) shows an example where HSFL($\perp$E) become visible on the superalloy CMSX-4. In addition, coarse macro-ripples (also called groove) are observed with the spatial periods of several microns much bigger than laser-wavelength, for example, grooves are observed on the silicon in Fig 2.1(b).

In general, LIPSS formation is affected by irradiation conditions, ambience and material state. The irradiation conditions include laser fluence, number of laser pulses, polarization state, incident angle, scanning speed, etc. Typical ambient conditions includes air, oxygen, vacuum, water, high refractive index liquid and other factors that can modify the properties around the interface. These factors exercise a complex influence as they affect light coupling and scattering, the dynamic aspect of nascent topologies and feedback issues. In this work, we investigated LIPPS formation in air environments. Material condition includes complex optical characteristics i.e. refractive index, surface roughness and thermal properties, such as thermal coefficients and transition points (melting point, vaporizing temperature, etc).

As a typical product of laser ablation or structuring, LIPSS formation involves a complex chain of physical processes related to the laser-material interaction; from laser excitation, energy deposition down to material movement and the development of

surface topologies. It equally involves a multiscale dynamics fixed by the optical and thermal material response. Brief presentations of excitation and transformation processes are introduced in the following chapter and we will focused here on characteristic features leading to ordered structured patterns.

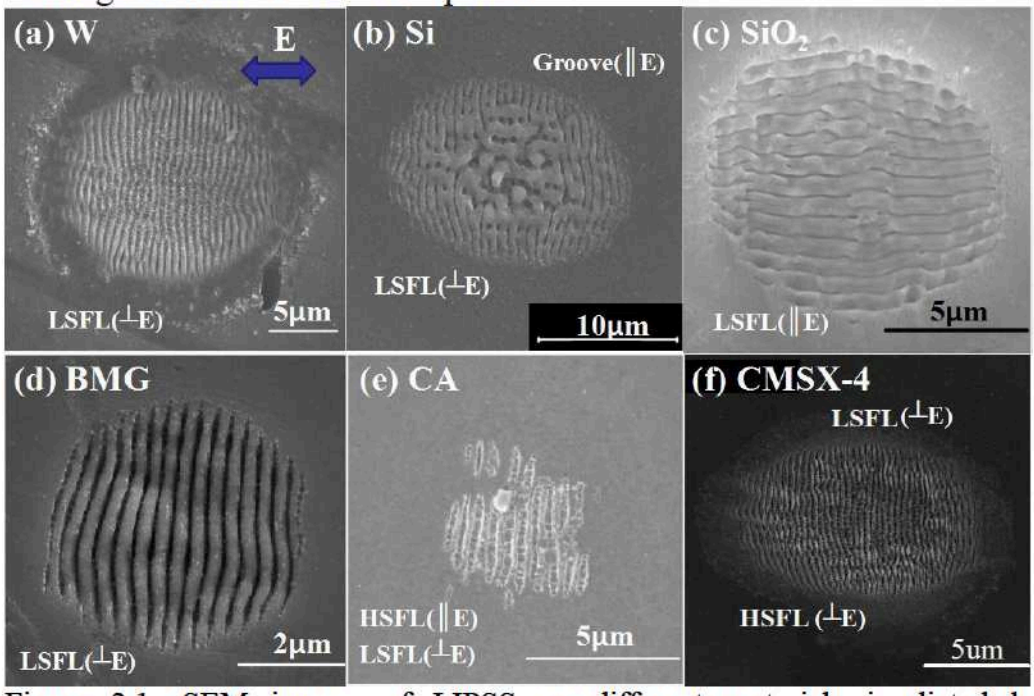

Figure 2.1: SEM images of LIPSS on different materials irradiated by linearly-polarized fs laser pulses: (a) metal tungsten; (b) semiconductor single crystal silicon; (c) Fused silica; (d) Bulk metal glass (BMG); (e) Crystal alloy (CA) from BMG; (f) CMSX-4.The laser polarization (E) direction is indicated in (a) with a double-head arrow. Note that different scales in each image.

2.2 Mechanisms of LIPSS

We have seen in the introductory part that LIPSS is a universal phenomenon on almost all the solids, including metals [DTS+12, GIK+11], semiconductors [BH03, BBK+02], dielectrics [CKR04, HCT+07], ceramics [DRW+03] and polymers [BBK99]. The continuous wave laser [KIA+11] and pulse lasers with long pulse duration can generate the classical ripples with periods of about the laser wavelength, which is often termed as low-spatial-frequency LIPSS (LSFL) [BNJ14]. Under the ultrafast laser ablation in the range from femtosecond to picosecond laser, except LSFL, fine nano-ripples are generated with the spatial periods much smaller than the half of applied laser wavelength, which is often termed as high-spatial-frequency LIPSS (HSFL) [BNJ14]. Furthermore, coarse macro-ripples with the spatial periods in a several microns range, as well as the arrays of conical features are generated in ultrafast laser

ablation [BBK+02]. Generally, LIPSS completely form after a certain number of pulses at the fluence near the single-pulse ablation threshold. The feedback process between incident laser and surface nanostructures plays an important role in the ripple formation [LCC+16]. The LIPSS orientation is controlled by the polarization of the laser electric field. However, surface defects also play an important role in LIPSS orientation [LCC+16].

Several LIPSS experiments on a wide range of materials under different laser wavelengths have been carried out and analyzed with intensive theoretical studies, however, LIPSS formation mechanisms are not yet fully understood and still under debate until now. Several mechanisms were suggested to explain the formation of LIPSS, including probably to most comprehensive approach – the generalized scattering and interference (Sipe) model [YPD+83, SYP+83], plasma mediated LIPSS formation [BNJ14, SHT+09, OHM+10], surface plasmon polariton (SPP) mediated LIPSS formation [HG10, VMG07, VG08b, CGB+12], and self-organization of unstable matter [VRV+15]. Part of LIPSS reported on different solids upon near-infrared fs-laser pulse irradiation and proposed formation mechanisms are summarized in table 2-1. The main LIPSS formation mechanisms are discussed in the following.

Table 2-1: Literature summary of LIPSS reported on different solids (metals, semiconductors and dielectrics) upon near-infrared fs-laser pulse irradiation (λ=740-800 nm, τ=25-160 fs, ν<5 kHz) and nearly normal incidence in air or vacuum, and proposed formation mechanisms. Lattice structure: c–single-crystalline, a–amorphous; LIPSS orientation: $\perp$: ripples aligned perpendicular to polarization, $\parallel$: ripples aligned parallel to polarization; LIPSS formation mechanism: Sipe: Sipe theory [SYP+83], SPP: surface plasmon polariton, roughness effect, heat effect, surface plasma, interference mechanism, Drude: Drude model for transient optical properties, CE: Coulomb explosion. Material classes: metal–red color, semiconductor–green color, dielectric–blue color.

Material	Λ_{LSFL} (nm)	Λ_{HSFL} (nm)	Reference and mechanisms
Al	500 - 530 ⊥	20 - 220	[YPD+83] Sipe model, [GIK+11, DTS+12]
Au	580 ⊥		[HG10, VMG07] SPP+roughness+heat [WG05, WG07]
Cu	500 - 700 ⊥	270-370 ⊥	[SHT+09] Surface plasma, [WG05, WG07]
Ni	750-760 ⊥	200 ∥	[GCP+11, CGB+12] SPP+Drude
Pt	550 - 700 ⊥		[HG10, VMG07] SPP+roughness+heat [OHM+10] surface plasma
Ti	500 - 700 ⊥	200 - 400 ⊥ 70 - 90 ∥	[OHM+10] surface plasma. [TAN+06] [BKH+12, GEI+09, VG07]. Interfernce+SPP
W	400 - 600 ⊥		[OHM+10], surface plasma [ZMW07]
Mo	470-720 ⊥		[OHM+10], surface plasma [VG08b] SPP+roughness+heat
CuZn	600-680 ⊥		[HZC+09] Interference+SPP
Steel 316L	660 ⊥		[DSS+10]
Steel X40Cr14	550-580 ⊥		[BVA+10]
c-InAs	700 ⊥		[BH03]
c-Si	560-730 ⊥		[BKH+12, BRK09, DIT+13] SPP, [YPD+83] Sipe model, [BK10, BRK11] Sipe model+Drude+SPP [BBK+02, WG07] [SRO+12, SRO+13] Sipe+Drude
c-InP	590 - 750 ⊥	330 - 360 ⊥	[CKR04, BMS05]
c-GaP	520 - 680 ⊥	150 - 175 ⊥	[HCT+07]
c-ZnO	630 - 730 ⊥	200 - 280 ⊥	[DRD+09]
diamond	750 ⊥	210 ∥	[WMF+03] [HZC+09] SPP+CE [HRK+12] Sipe+Drude
a-SiO_2	500 - 800 ∥	170 - 400 ⊥	[BKH+12, RDH+11, SLV+08, RR12], [BNJ14] Surface plasma
c-SiO2	460-900 ∥	170-450 ⊥	[HRK+12] Sipe model + Drude
graphite		70-170 ⊥	[HZC+09] SPP+CE
c-SiC	500 ⊥	250 ⊥	[YUK10]

2.2.1 The Sipe diffraction theory

For the classical LSFL ripples, Sipe theory has been widely accepted to describe the formation, based on the interference between the incident laser and surface-scattered electromagnetic wave [YPD+83, SYP+83]. J. E. Sipe et al developed the theory of LIPSS formation by associating the Fourier component of LIPSS with the corresponding Fourier component of inhomogeneous energy deposition beneath the surface [SYP+83]. Sipe theory describes the electric field intensity distribution created by a plane wave incident on a thin, rough surface selvedge region, whose height is much less than wavelength. The roughness of the surface selvedge region is characterized by shape factor s and filling factor F. Shape

factor s is the ratio of the correlation distance on the surface to the thickness of the selvedge, corresponding to the shape of nanoparticles which make up the rough surface. Filling factor F represents the fraction of the surface filled up with the nanoparticles.

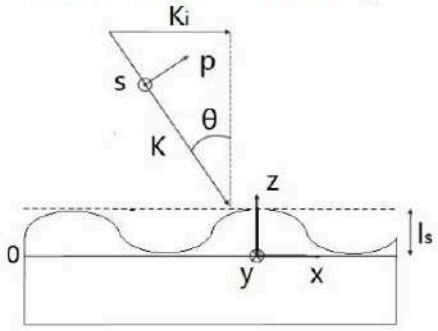

Figure 2.2: Drawing of laser beam incidence on rough surface in Sipe theory.

A sketch of the geometry of the laser beam incidence on a rough surface in Sipe theory is shown in Fig. 2.2. The region z>0 is air and the region z <0 represents the bulk material. The surface roughness is confined in a region of thickness l_s. The incident laser with s or p polarization carrying the wave vector K_L is incident on the rough surface at an angle of incidence θ, which has a component K_i in the horizontal plane. The LIPSS wave vector is $K=2\pi/\lambda$. Sipe theory provides an expression for the inhomogeneous energy deposition on the surface, which is proportional to $\eta(K, K_i)\times|b(K)|$, where the efficacy factor $\eta(K, K_i)$ describes the efficacy with which the roughness leads to an inhomogeneous energy absorption at K; $|b(K)|$ represents a measure of amplitude of the surface roughness at K. It is assumed that ripples grow where the absorbed energy is the largest. Because $|b(K)|$ varies slowly for a surface with homogeneously distributed roughness, the efficacy factor $\eta(K, K_i)$ exhibits sharp peaks at certain K, which determines the spatial ripple periodicity [SYP+83].

Sipe model based on a modulated energy deposition was in good agreement with many experimental results, such as LIPPS on metals [YPD+83, SYP+83], semiconductors [YPD+83, SYP+83, SRO+13] and dielectrics [HRK+12].

However, along with its strong predictive character on processing features, Sipe model itself has some limitations. Firstly, Sipe model is an approximate solution, in which the longitudinal component of the electromagnetic field is treated by a variational principle and the transverse component of the electromagnetic field is treated by a perturbation series. The accuracy of Sipe model is limited. Secondly, the physical nature of the electromagnetic field structures "radiation remnants" in Sipe model is still a question, which takes the place of the surface-scattered wave concept in the

semiconductor. Finally, for metal, the excitation of surface plasmons may take the place of radiation remnants in Sipe model. The relationship between radiation remnants and surface plasmons is not clear [SYP+83].

To overcome these problems in Sipe theory, other mechanisms are proposed, such as second harmonic generation (SHG) on surfaces [BH03], transient changes of the optical properties in the excited material during the laser pulse [WMF+03], as well as self-organization based on the instability of excited materials [VRV+15]. However, none of the above mentioned mechanisms can explain all characteristics of LIPSS.

2.2.2 Surface plasmon polariton (SPP) mediated LIPSS formation

In the Sipe theory, alternatively or in addition to surface-scattered electromagnetic waves on metal surface, surface plasmon polaritons (SPPs) may play an important role. Sipe *et al* [SYP+83] indicated that the formation of LSFL ripples on metals can, in particular conditions, be seen as deriving from the interference between the incident laser and SPPs where the former can be a type of surface scattered wave.

When a linearly polarized laser pulse is irradiated at the air-metal interface at the incident angle of θ, the period Λ of LIPSS formed due to the interference between the incident laser and the excited SPP is given by [FS82, ZFS82, SF86, VMG07]

$$\Lambda = \frac{\lambda}{\eta \pm \sin\theta} \tag{2-1}$$

$$\eta = \mathrm{Re}\sqrt{\frac{\varepsilon}{\varepsilon + 1}} \tag{2-2}$$

Here λ is the incident laser wavelength, η is the real part of the effective refractive index of the air-metal interface for surface plasmons, ε is the dielectric constant of the metal. Under the intense ultrafast irradiation, the effective refractive index may change and affect the scattered wave or surface plasmons.

C. Guo *et al* investigated fs-LIPSS on metal Pt and Au and found that both the calculated periods of Pt and Au are overestimated by about 30% in SPP theory, which was explained by the increase in the real part of the refractive index duo to the effects of surface nano- and micro-roughness, as well as a heating effect [VMG07].

M. Huang *et al* proposed the mechanisms of initial direct surface plasmon (SP)-laser interference and the subsequent grating-assisted SP-laser coupling to explain the LIPPS formation on all the solids including metals, semiconductors and dielectrics, which involve the grating-coupling mechanism leading to the decrease of spatial periods with the increase of groove depth. [HZC+09].

The theory of SPP-mediated LIPSS formation can explain some experiment results on metals [ZCL+15], for example, LSFL on metal Ni [GCP+11], Al and brass [YPD+83]. However, J. Z. P. Skolski *et al* 's investigation by FDTD simulations showed that the propagation of SPPs is not a necessary condition for LSFL formation, moreover, the grating-assisted SP-laser coupling mechanism proposed by M. Huang [HZC+09] seems inapplicable because the spatial periods of surface structures are same as the periods of energy modulation. This indicates a need for further experimental clarification and evidence towards the behavior of non-plasmonic metals, semiconductor and dielectric surfaces and the potential that they may support SPP during the irradiation by short-pulse laser around the damage-threshold fluence.

2.2.3 FDTD-electromagnetic (EM) approach

The finite-difference time-domain (FDTD) method can simulate light propagation, scattering and diffraction phenomena by solving Maxwell's equations numerically. The method was introduced by Yee in 1966[Yee66] and since then has been a powerful engineering tool for integrated and diffractive optics device simulations. J. Z. P. Skolski *et al* proposed the numerical method based on the finite-difference time-domain (FDTD) method to investigate qualitatively LIPSS formation on rough surface and the effect of inter-pulse feedback mechanisms [SRO+12, SRO+13, SRO+14], which is simplified as FDTD-EM approach here. Not including incubation effects and the thermodynamics of molten or ablated materials,ablation model (HAM) is used as rough surface model in this approach, shown in Fig 2.3(a). The FDTD method can provide electric field distributions in the vicinity of the surface, identifying thus electromagnetic effect in the definition of anisotropic energy absorption patterns. Present approaches takes into account the role of scattering from surface roughness and the creation of stationary field patterns with evanescent components. It will be shown in this work that the FDTD approach can take into account the effect of

polarization and topographic surface features, being thus a powerful instrument in LIPSS analysis [ZCL+15].

A recent advance in FDTD methods applied to LIPSS consists of the attempt of accounting for feedback effects. After the first laser pulse, the absorbed electromagnetic energy in the surface layer causes the modification of rough surface by material removal. After next laser pulse, the new surface morphology is used for subsequent FDTD simulation, leading to a new absorbed energy profile and a further modification of the rough surface. Hence, the feedback cycle can be iterated many times until expected LIPSS form. The sketch map of inter-pulse feedback mechanisms in FDTD simulations is shown in Fig. 2.3(b).

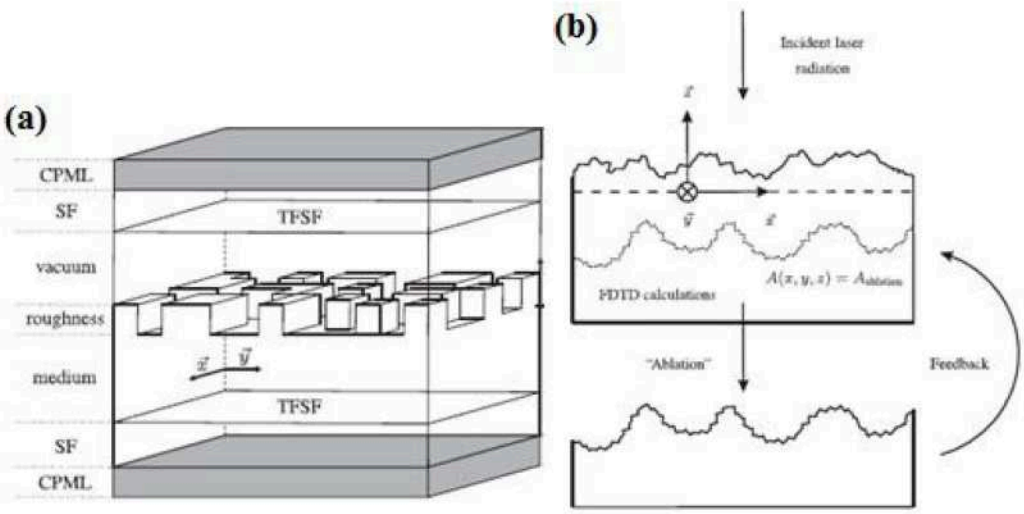

Figure 2.3: (a) holographic ablation model used in FDTD simulations. (b) Inter-pulse feedback mechanisms in FDTD simulations [SRO+14].

Some of the main conclusions derived from employing FDTD methods are emphasized here [SRO+14]:

(a) For LSFL formation, surface plasmon polaritons (SPPs) are not a necessary condition. The grating-assisted mechanism proposed in Ref. [HZC+09] can't explain the periodicity decreasing of LSFLs with increasing pulses because the spatial periods of surface structures are same as the periods of laser-induced energy modulation.

(b) HSFL orthogonal to the polarization looks like double frequency of LSFL in spatial frequency domain, which is a striking result of the FDTD-feedback simulations.

(c) Except HSFL on semiconductors and dielectrics, HSFLs parallel to the polarization can be expected on metals, which are in agreement with experimental results.

(d) Groove (micro-ripples) parallel to the polarization can be predicted by the approach. Grooves without LSFLs were not found.

However, the deficiencies of FDTD-feedback simulations are also listed in the following:

(a) HSFLs parallel to the polarization form only when Re(ñ)> Im(ñ), which is not in agreement with the experiment results on alloyed steel and titanium [SRO+14]. The reason may be from the algorithm chosen for the FDTD calculations depended on the optical properties of the medium. In cases where Re(ñ)<Im(ñ), the Yee algorithm is unstable [Kok12] and the auxiliary differential equation method was used [TH05].

(b) The FDTD-EM approach provides a rather embedded result of EM numerical calculations, that does not uncover the underlying physics of LIPSS formation, for example, HSFL orthogonal to the polarization with double frequency of LSFL in spatial frequency domain, grooves only with LSFL. Giving global field solutions, the access to sources and electronic currents is problematic.

(c) The FDTD-EM remains simplistic without the inclusion the complex processes, such as transient excitation, incubation effect, SHG [DRD+09] and self-organization based on material movement.

2.2.4 Self-organization model based on material instability

Inspired by the similarity of the laser-generated patterns with the patterns induced by energetic ions, self-organization model upon femtosecond laser ablation [RCH+02, RVV+11] is proposed according to the existing formation theory of ion-beam induced ripples [BH88] with a dependence on laser polarization related to an asymmetry in the ionized kinetic energy distribution [RVV+11], which supposes an active contribution of the irradiated unstable material. The absorbed laser energy causes an unstable surface region by the perturbation and softening of the crystal bonding, where self-organization is driven by competition between surface roughening due to erosion and smoothing, leading to LIPSS formation in the laser-modified area [RCB06, VRR10]. Spatial and temporal evolution of the perturbed surface can be represented by nonlinear equations of the Kuramoto-Sivashinsky type [KT76, Siv79]. Marangoni effect may also play a role in LIPSS formation. Marangoni effect cause the liquid flowing from the hotter to the cooler regions in the molten material because surface tension decreases with increasing temperature for most liquids [BKG+97], which is also called thermo-capillary convection [Get98].

Until now, self-organization model has estimated LIPSS formation, interaction times/number of incident pulses, as well as the relative influence of input energy on the ripple period [VRR10]. However, self-organization model is just a possible scenario and was not yet verified by experiments. It nevertheless positions itself as an alternative process to the coherent interference model involving surface waves.

2.2.5 Second harmonic generation (SHG)

Femtosecond laser ablation towards regular patterns may equally include some nonlinear effects generated at the surface, as among them second harmonic generation (SHG). SHG is related to the surface-generated symmetry breaking. It is still in debate if SHG might be involved in the formation of the HSFL, however its involvement was justified by the appearance of structures of higher periodicities. For example, J. Bonse's investigation revealed the SHG is generated in the regime of HSFL formation on ZnO by spectroscopic experiments [DRD+09]. However, other experiments on TiO_2 and Al_2O_3 surfaces confirmed that SHG does not affect ripple periodicity [BRŠ+11]. The inconsistencies of these results still promote a debate if SHG contributes to LIPSS formation.

2.2.6 Transient optical coupling for LIPSS

In order to explain the LIPSS spatial periods of subwavelength range in ultrafast laser ablation of various semiconductors, J. Bonse *et al* proposed an approach, which combines the Sipe theory with the transient excitation and the intra-pulse transient changes of the optical properties in the irradiated materials [BRK11]. Thus, with Drude-like free-electron contributions in the optical response, the real part of the dielectric function will go down, potentially allowing plasmonic excitation if the synchronism conditions permit. This approach is proposed to explain the LSFL formation on silicon originating in a spatially modulated energy deposition at the surface due to the interference between the incident laser beam and the excitation of surface plasmon polaritons on the dense free-electron-plasma in the excited material during the pulse. This approach and the role of the feedback upon the multi-pulse irradiation are shown in Fig. 2.4.

However, LIPSS formation on Ge can be explained by Sipe theory without transient optical properties [YPD+83]. In addition, it is an important question if transient changes of the optical properties

in the irradiated semiconductors could support SPPs in the pulse duration. And it needs strong experimental evidences that the intra-pulse transient changes of the optical properties in the irradiated materials contribute to the LSFL formation.

Due to the importance of the time-varying optical coupling during irradiation, the issue of optical transients will be detailed in the next chapter, in a general context of ultrafast laser-material interaction.

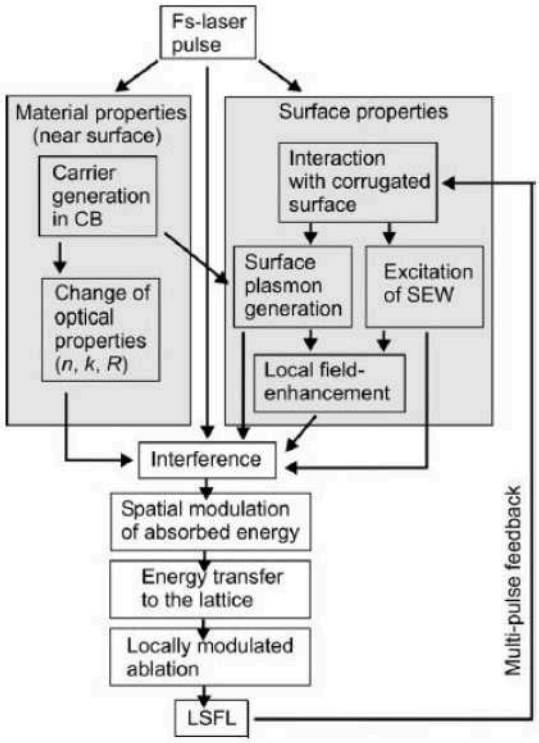

Figure 2.4: Scheme of physical processes involved in the formation of LSFL on silicon surface upon femtosecond laser pulse irradiation [HHR+15].

Recently, J. Bonse *et al* reported the experiments, in which LIPSS formations on fused silica, silicon and titanium were studied with linear, parallel or cross-polarized, two-color double-fs-pulse sequences (50 fs, 400 nm and 800 nm) under sub-threshold conditions in the temporal pulse delay (-10 ps < t< +10 ps) [HHR+15]. They concluded that LIPSS on silicon and titanium can be explained by a plasmonic mechanism. In contrast, LIPSS on fused silica can be explained by a non-plasmonic mechanism, in which the transient carrier profiles generated by laser pulses scatter into self-trapped excitons (STE) and color centers as a seed for incubation effects leading to locally modulated ablation.

All these observations show the multitude of hypotheses and scenarios in ripple formation, requiring thus novel physical insights to foster further understanding.

2.3 Materials transformations under LIPSS

Material response to laser irradiation usually results in permanent changes to the chemistry, composition, crystal structure and morphology of material surface.

For multi-component materials, the species in the surface layer may be depleted at different speeds in laser ablation in fluence regimes connected with inhomogeneous heating, leading to the changed chemical composition of the remaining material [MCR98].

In ultra-fast laser irradiation, the large temperature gradients induced by rapid heating generate thermal stresses and thermo-elastic acoustic waves, resulting in the mechanical response of the material, for example, hardening and warping [CFW+77]. When the material is heated above melting point, hydrodynamic motion can reshape the molten material. For example, convective and thermo-capillary forces can cause the retribution of molten material which frozen during solidification. Laser ablation is always accompanied by a dense vapor plume including atomic and molecular species, and solid and liquid clusters of material ejected from the irradiated surface. Recoil from the plume also generates shockwaves, resulting in plastic deformation and hardening of the material. The recoil can also expulse the remaining molten material. Residual heat left in the remaining material can cause further melting or other thermally activated processes.

After rapid heating, the condensation of plume material leads to the formation of clusters and nanoparticles at the surrounding areas of the ablated region. Rapid self-quenching of the material can freeze in defects, supersaturated solutes and metastable phases. Slower re-solidification can induce the recrystalization of the material.

Energy relaxation depends on the strength of electron-phonon coupling [CGF+12]. This shows an influence of the strength of the electron-phonon coupling on ripple formation.

Material responses and final properties are dependent on the laser parameters. For the desired application, final material properties after irradiation can be precisely controlled by choosing the appropriate laser parameters.

2.4 Applications of LIPSS in material surface processing

There are several conventional techniques for surface processing, for example, mechanical surface processing, sand blasting with Al_2O_3 particles or acid etching that roughen surface randomly but may contaminate the material [BLZ+11]. These are complex procedures and cannot process non-planar surfaces in the micro/nano-scale. Ion beam and electron beam milling which can fabricate nanostructures precisely but cost expensively and need the vacuum condition [SMZ+13].

Unlike conventional techniques, lasers provide a fast, non-contact, precise and clean alternative for surface processing in ambient conditions. As one of the major advantages, laser has the ability to precisely control deposited energy in desired regions and energy rates by many methods, for example, beam steering by galvanometric scanning mirrors, beam shaping with amplitude masks, refractive elements [RD96] and diffractive optical elements [MNK+98] as well as spatial light modulators [SHA+05]. Duo to the advantages, laser has been applied widely in the surface processing. Beyond the idea of accurate remote processing, the possibility of achieving multiscale structuring in periodic patterns is of interest. Thus, LIPSS provides a fast, precise and low-cost tool for surface micro/nano-structuring and the possibility to design hierarchical surfaces and models for structured contact interfaces in optics and mechanics. Some specific applications of LIPSS are discussed in the following.

2.4.1 Surface wetting

Inspired by the remarkable nature example of the lotus leaf, super-hydrophobic surfaces induced by hierarchical micro/nano-structures were demonstrated, as shown in Fig. 2.5(a, b) [Blo03, ZSB+08]. Except the hierarchical topography surface chemistry also contributes to the wettability, such as pH, H adsorption, oxidation, etc. LIPSS including hierarchical micro/nano-structures can thus precisely control the surface wetting characteristics with super-hydrophobic [BZS+09] or super-hydrophilic properties [VG10] by the choice of laser parameters. An example of laser-induced hydrophobicity is shown in Fig. 2.5(c, d) [BZS+09]. Laser surface processing has been widely in the applications for surface wetting, for example, self-cleaning

surfaces [BZS+09], micro fluidics [GVM+12], water proof and de-icing coatings for aviation [CNM+13].

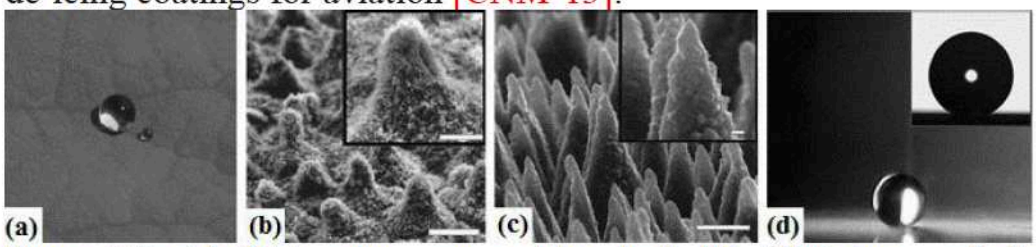

Figure 2.5: (a) Water drops on a lotus leaf. (b) SEM image of the micro-structures on the surface of a lotus leaf (scale bar 10 μm) and inset: nano-structures (scale bar 5 μm) [Blo03]. (c) SEM images of femtosecond laser textured Si surface showing micro-structures (scale bar 5μm) and inset: nano-structures (scale bar 1 μm) . (d) A water droplet on a laser-structured Si surface [BZS+09].

2.4.2 Tribology and microfluidics

For years, laser surface texturing (LST) has been used to enhance the tribological properties of material surface [DWC+15]. For instance, the structuring of cylinder walls in combustion engines serving as reservoirs for oil can prevent the breakdown of oil-film, resulting in significantly reduced particle emission [AK01]. In this case, ultrashort laser pulses can produce high quality shallow structures, for example, LIPSS, without recast layers and burr [WD04]. LIPSS can align and orient the liquid flow, offering the potential application in the microfluidics.

2.4.3 Modification of optical properties

LIPSS can be used as a dye-free coloring on materials allowing changing the color appearance, for instance, A. Y. Vorobyev et al produced a light yellow Al, a bluish Ti using a diffractive effect generated on rippled surfaces [VG07]. The color appearances on metal are dependent on the spatial periods and orientation of nano-ripples, which can be controlled by laser parameters [DSS+10]. Fig. 2.6 shows a remarkable example of colorful picture created by fs-LIPSS on a stainless steel [DSS+10].

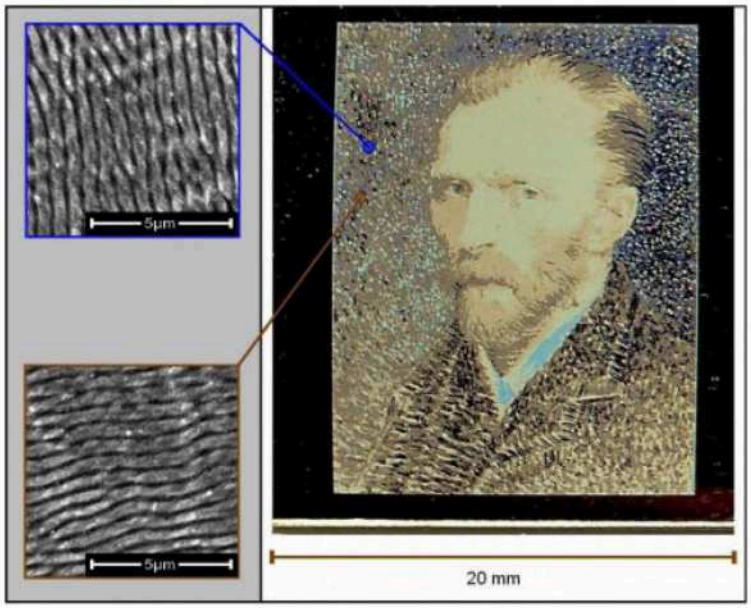

Figure 2.6: Colorful picture comprised of controlled nanostructures by femtosecond laser pulses on 316L stainless steel [DSS+10].

2.4.4 Marking and coding

LIPSS can be applied in marking and coding for authentification and traceability. Color marking is made by the use of ordered nano-ripples with designed orientation and spatial periods on desired regions, which are controlled by laser parameters [DSS+10]. Two-dimensional data codes can be written, consisting in an array of controlled nanostructures by femtosecond laser pulses which are useful for traceability [Lan11]. The process can be rendered parallel by laser beam shaping technologies employing spatial light modulators. An example is the colorful marking and two-dimensional code created on stainless steel by femtosecond laser pulses from French Qiova Company in Fig. 2.7 [Qio16].

Figure 2.7: Marking "Qiova" and two-dimensional codes consisting of controlled nanostructures by femtosecond laser pulses on stainless steel [Qio16]

2.4.5 Light trapping and emitting

Light trapping is useful for photodiodes, sensors and solar harvesting cells. Multiple length scales of surface features reduce the reflections based on three mechanisms dependent on the size of surface features: (a) For feature size much longer than the incident wavelength, light trapping due to multiple reflections from protruding structures enhances coupling into the material, moreover, refraction at oblique angles increases the effective optical path length; (b) For feature size close to incident wavelength, light trapping due to scatter increases the effective optical path length and enhances absorption; (c) For feature size much smaller than incident wavelength, light trapping due to moth-eye effect reduces reflection [SMP10].

LIPSS, similar to a surface grating, induces the dispersion, but LIPSS usually doesn't enhance the absorption significantly due to their shallow height [VG08a]. However, laser-induced arrays of high-aspect-ratio cones or columns features can trap light efficiently [SMA+96]. For example, the micro-structured silicon with micro-cones by femtosecond laser in the atmosphere of SF_6 shows the broadband reduction in reflectivity [SWC+05].

LIPSS can enhance the efficiency in light emitting devices, useful for solid state illumination. Increased emission by LIPSS is due to the surface increase and sharp surface nanostructures reducing the work function of material [BSS+11]. LIPSS can also change the emission spectrum. For example, the efficiency of lamp was increased and the emission spectrum can be controlled by making LIPSS on the tungsten filament in lamp by fs laser [VMG09, Wan09].

2.4.6 Bio-medical application

LIPSS has been widely used in biological and medical applications. For example, LIPSS on biological implants encourages cell growth and improves osseo-integration [KCB+04, CBB+02]. Another example is the black Si with LIPSS created by fs laser, which has the bactericidal function [IHW+13]. For a remarkable example, LIPSS on noble metals can be used as high-efficiency substrates for surface-enhanced Raman spectroscopy (SERS) [MDL+14].

2.5 Challenges and opportunities

LIPSS formation involves a range of complex processes related to optics, photophysics, photochemistry, thermodynamics, hydrodynamics, condensed matter physics, plasma and so on. Only considering optical features, the scenarios of LIPSS formation put forward features of linear and nonlinear optics, such as scattering, interference, excitation of surface plasmon polaritons (SPPs), excitation of plasma, second harmonic generation (SHG) and transient changes of the optical properties in the irradiated materials. For ultrafast laser ablation, it is a challenge to investigate the complex LIPSS formation in fs-ns time domain, in which limited instruments can be applied.

Until now, LIPSS formation mechanisms are not yet fully understood and still under debate. Sipe theory has been widely accepted to explain the LSFL formation based on scattering and interference, but Sipe theory still faces some challenges especially in the limited accuracy. However, potential self-organization model only works in ultra-short pulse, not proper for the laser with long pulse duration related to the weaker laser peak fluence. FDTD-EM approach offers a precise numerical tool to investigate LIPSS formation in the electromagnetic domain, which showed that the propagation of SPPs is not a necessary condition for LSFL formation, and the grating-assisted SP-laser coupling mechanism seems inapplicable because the spatial periods of surface structures are same as the periods of laser-induced energy modulation. In that concern LIPSS formation theories respectively mediated with SPP, SHG and intra-pulse transient optical properties, they still need strong experimental evidences.

LIPSS is a universal phenomenon on almost all the solids induced by the lasers ranging from long pulse to ultra-short pulse. Their appearance on the different materials such as metals, semiconductors and dielectrics, the parts of LIPSS mainly related to LSFL are very similar, which reveals a common LIPSS formation mechanism existing in all solids in the electromagnetic domain. However, now the LIPSS formation theories are different on metals, semiconductors and dielectrics. For example, the interference with SPPs in Sipe theory for metals, the interference with surface-scattered electromagnetic wave in Sipe theory for semiconductors, plasma-mediated formation resulting in regular patterns of self-trapped excitons (STE) and color centers-mediated structural transitions for dielectrics need to converge towards more unified frames. This implies further consideration and we have

identified opportunities to find common LIPSS formation mechanisms on metals, semiconductors and dielectrics in the electromagnetic domain by FDTD-EM approach.

Except LSFL and HSFL, other laser-induced micro/nano-features such as such as bubbles, cones, columns and abnormal ripples as well as macro-structures, and in general surface topographies should be taken into LIPSS formation theory.

In order to explain the complex LIPSS formation in ultrafast laser ablation, more experiments need to be designed and carried out. For example, fs laser-induced transient optical properties can be measured to check the LIPSS formation theory in connection to transient optical properties. In addition, for some complex materials, such as bulk metal glass, there are some distinctive types of LIPSS, which also need more investigations.

2.6 Conclusion

In this chapter, we introduce the general aspects of laser-induced periodic surface structures (LIPSS). Several LIPSS forms and periodicities reported on different solids upon near-infrared fs-laser pulse irradiation were reviewed. However, LIPSS formation mechanisms are not yet fully understood and still under debate until now. Several LIPSS formation theories with merits and limitations are introduced, including Sipe theory, FDTD-EM approach, self-organization model of unstable matter and LIPSS formation respectively mediated with surface plasmon polariton (SPP), second harmonic generation (SHG) as well as with the evolution of optical properties during irradiation. We introduce material transformations under LIPSS, related to the permanent changes of the material in the chemistry, composition, crystal structure and surface morphology. At last, we show the applications of LIPSS in material surface processing, including surface wetting, tribology, modification of optical properties, marking and coding, light trapping and emitting, as well as bio-medical application.

Chapter 3

Dynamics of excited materials: fundamental processes in optical coupling and laser ablation

In this chapter, with a brief introduction of optical properties, we discuss various complex processes in the ultrafast laser-matter interaction. We also review fundamental transient electronic and structural effect that define the coupling of ultrafast laser radiation and material, from band population and Fermi smearing to bond-breaking and structural rearrangements.

At first, this chapter briefly introduces the optical properties of solids. Then the accent is put on the fundamental processes of laser ablation. Next, the transient responses of metals to ultrafast laser are introduced, focusing on the electronic, lattice structure and plasmonic effects. Finally, we introduce the transient responses of semiconductors to ultrafast laser radiation, involving the changes of electronic configuration and lattice structure due to optical excitation.

3.1 Optical properties of solids

At first, the electronic origin of optical properties in solids is briefly introduced. The propagation of an electromagnetic wave in a material is determined by the responses of the material to electric and magnetic fields, which are characterized by the dielectric

constant ε, the magnetic permeability μ and the electric conductivity σ. For the optical part of the electromagnetic spectrum, the magnetic permeability can be taken to be μ=1 [LL84]. As a result, the optical response of a material is solely determined by the frequency ω of the oscillating electric field, and thus dispersion occurs. The frequency-dependent phase velocity v of wave in a material is given by

$$v(\omega) = \frac{c}{\mathrm{Re}\sqrt{\varepsilon(\omega)}} = \frac{c}{n(\omega)} \tag{3-1}$$

where $\varepsilon(\omega)$ is the dielectric function of the material; $n(\omega)$ is the refraction index, governing the linear response of a material to light.

Drude-Lorentz model describes successfully the optical properties of many metals and semiconductors, particularly in the near infrared range, despite the use of only a few parameters. For example, Drude model of Ag and Lorentz model of Te are shown in Fig. 3.1, matching reasonably the measurement results.

Optical properties are related to the electronic structure of materials. In metals, the dominant contribution to the dielectric function arises most commonly from free-carrier interaction. The excited electrons undergo intraband transitions from an occupied to an unoccupied state in the same band around the Fermi level. Considering the response of free electrons (considered as individual, non-correlated particles) to the electromagnetic wave of the oscillating frequency ω, the dielectric constant is given by Drude model:

$$\varepsilon(\omega) = 1 - \left(\frac{Ne^2}{m\varepsilon_0}\right)\frac{1}{\omega^2 + i\gamma\omega} = \varepsilon'(\omega) + i\varepsilon''(\omega) \tag{3-2}$$

Here N is the number of free electrons, e is electron charge, m is electron mass, ω is the light frequency, γ is the collision frequency, ε_0 is the electric permittivity of free space, $\varepsilon'(\omega)$ is the real part of dielectric function and $\varepsilon''(\omega)$ is the imaginary part of dielectric function. The collision frequency γ is the damping factor of electrons, contributing the imaginary part of dielectric function, which determines the absorption. In the framework of Landau's theory, in the low temperature limit $T_e << T_F$ (Fermi temperature), the collision frequency γ is proportional to T_e^2 [FFH+01]. The collision frequency is a sum of contribution of electron-electron interactions (provided that the total momentum changes, e.g. umklapp interactions), electron-phonon/ion and electron-defect contributions.

If $\gamma << \omega$ (for collisionless materials, such as plasma), the imaginary part of dielectric function vanishes and the real part becomes

$$\varepsilon'(\omega) = 1 - \left(\frac{Ne^2}{m\varepsilon_0}\right)\frac{1}{\omega^2} = 1 - \frac{\omega_p^2}{\omega^2} \tag{3-3}$$

Here ω_p is the plasma frequency. In addition, for plasma of free electrons with small nonzero damping, the effect of the collision frequency γ is to reduce the forbidden band of frequencies.

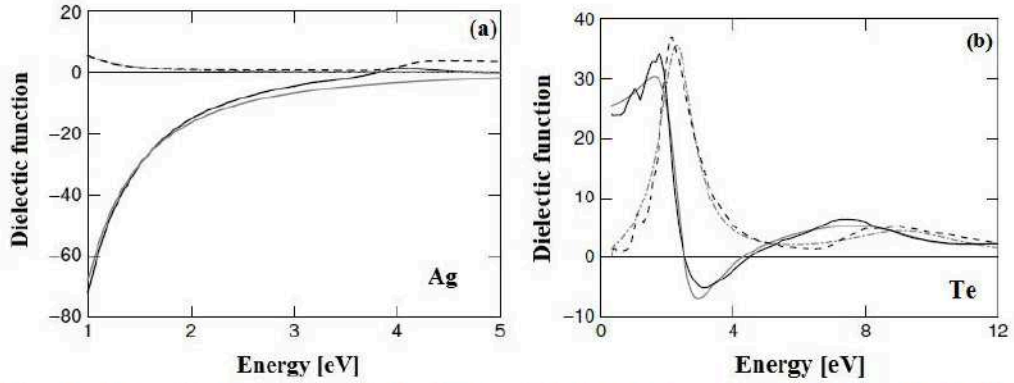

Figure 3.1: (a) Drude model of Ag. (b) Lorentz model of Te. Black lines represent literature values of Re[ε] (solid) and Im[ε] (dashed) [Pal85], while gray lines represent the best-fit values of Re[ε_{model}] (solid) and Im[ε_{model}] (dash-dotted).

Particularly in transition metals, d-orbitals can contribute to the dielectric function via interband transitions. Generally intraband transitions of polyvalent metals are evaluated as Ashcroft-Sturm contributions to the Drude-like dielectric functions [AS71].

In semiconductors, the excited electrons undergo interband transitions between valence band and conduction band. Considering non-excited semiconductors and the response of bound electrons to the electromagnetic wave of the oscillating frequency ω, the dielectric constant can be described using the Drude-Lorentz model:

$$\varepsilon(\omega) = 1 - \left(\frac{Ne^2}{m\varepsilon_0}\right)\frac{1}{\omega^2 + i\gamma\omega} + \frac{Ne^2}{\varepsilon_0 m}\sum_j \frac{f_j}{(\omega_j^2 - \omega^2) - i\gamma_j\omega} \tag{3-4}$$

Here N is the total number of electrons and f_j is the fraction of electrons having a resonant frequency ω_j and damping constant γ_j. The dissipation of electromagnetic energy absorbed by electrons is maximal at resonance, which shows that the peak in the imaginary part of the dielectric constant and the real part through zero are at the resonance frequency (Fig. 3.1(b)).

The real and the imaginary parts of dielectric function are linked by the Kramers – Kronig relations [Jac75].

$$\mathrm{Re}[\varepsilon(\omega)] = 1 + \frac{2}{\pi}P\int_0^\infty dv \frac{v\,\mathrm{Im}[\varepsilon(v)]}{v^2 - \omega^2} \tag{3-5}$$

$$\mathrm{Im}[\varepsilon(\omega)] = \frac{2w}{\pi}P\int_0^\infty dv \frac{1 - \mathrm{Re}[\varepsilon(v)]}{v^2 - \omega^2} \tag{3-6}$$

Here P represents the Cauchy principal value. The real and imaginary parts of dielectric function are not independent, so that the changes in one part cause the variation of the other.

Once the dielectric function of a material is known, all the linear optical properties can be deduced. For example, the reflectivity of a material is related to its dielectric function by the Fresnel formula:

$$R_s = \left| \frac{\cos\theta_i - \sqrt{\varepsilon - \sin^2\theta_i}}{\cos\theta_i + \sqrt{\varepsilon - \sin^2\theta_i}} \right|^2 \tag{3-7}$$

$$R_p = \left| \frac{\varepsilon\cos\theta_i - \sqrt{\varepsilon - \sin^2\theta_i}}{\varepsilon\cos\theta_i + \sqrt{\varepsilon - \sin^2\theta_i}} \right|^2 \tag{3-8}$$

Here R_s, R_p are respectively the reflectivities of s- and p-polarised light at the plane interface between the vaccum and a medium of dieletric constant ε; θ is the incident angle. Fig. 3.2 shows the reflectivities of of single-crystal silicon for s- and p-polarised 800 nm-light. For s-polarisation, the reflectivity monotonically increases with the incident angle. However, for p-polarisation, there is a minimum reflectivity at the Brewster angle of 74.86°. At normal incidence, the reflectivities for s- and p-polarised light are equal.

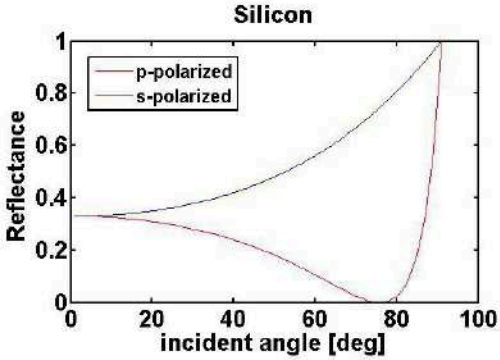

Figure 3.2 Reflectivity of single-crystal silicon for p-polarised (red curve) and s-polarised (blue curve) 800 nm-light as a function of the incident angle.

3.2 Ultra-short pulse laser interaction with solids

The laser–matter interaction has been the object of intense research in the last few decades [BNJ14]. The laser–matter interaction in the ultrashort mode involves several complex processes which put forward specific features related to non-equilibrium and damped heat diffusion.

The first step in the laser–matter interaction is the deposition of a certain amount of laser energy in the material. The spatial and temporal laser energy distribution alongside material response

determines the final modification of the solid surface. The process of energy deposition is initiated by the absorption of photons by the electrons by inverse Bremsstrahlung [SW79]. Consequently, the electrons are excited from their equilibrium states to some excited states and their distribution becomes broader by electron-electron interactions [CMN+96]. Both optical and electronic properties of the excited metals can be described by the free electron gas theory-Drude model in formula (3-2). For many transition metals, except the free electrons, the quasi-bonded electrons in d-band also contribute to the optical properties by the non-Drude interband transitions.

For insulators and semiconductors, after photon excitation, quasi-free electrons are created in the conduction band formed mainly from antibonding states, meanwhile, holes are created in the valence band. A Drude-like contribution appears in the expression of the dielectric function. The generated free-carriers are due to the multi-photon ionization, field ionization, impact ionization and avalanche ionization [Sze81]. The dielectric constant of excited insulators and semiconductors can be described using the Drude-Lorentz model in formula (3-4).

The second step is the excited carrier thermalization. The thermalization occurs via electron-electron collisions, and its characteristic time depends on the energetic characteristics (ranging from few tens of fs at low carrier energies to few fs at higher levels of excitation). This process changes neither the total energy in the carriers nor the carrier density but assists in defining an electronic temperature by redistributing carriers over the band. At the same time the total momentum stays unchanged unless for collisions involving reciprocal lattice vectors (umklapp process), a characteristics that will impact both optical and transport properties. To exemplify in the case of metal, there are three processes of excited carrier thermalizations after ultrafast laser pulse, shown in Fig. 3.3. At first, ballistic electrons are generated upon ultrafast laser irradiation and move into deeper parts of the sample (Fig. 3.3(a)) without suffering many collisional events. After the absorption of ultrafast laser pulse, the thermalization of electrons occurs (Fig. 3.3(b)), leading to the Fermi-Dirac distribution of the electron energy. At last, the electron-lattice system comes into equilibrium state via electron–phonon coupling (Fig. 3.3(c)).

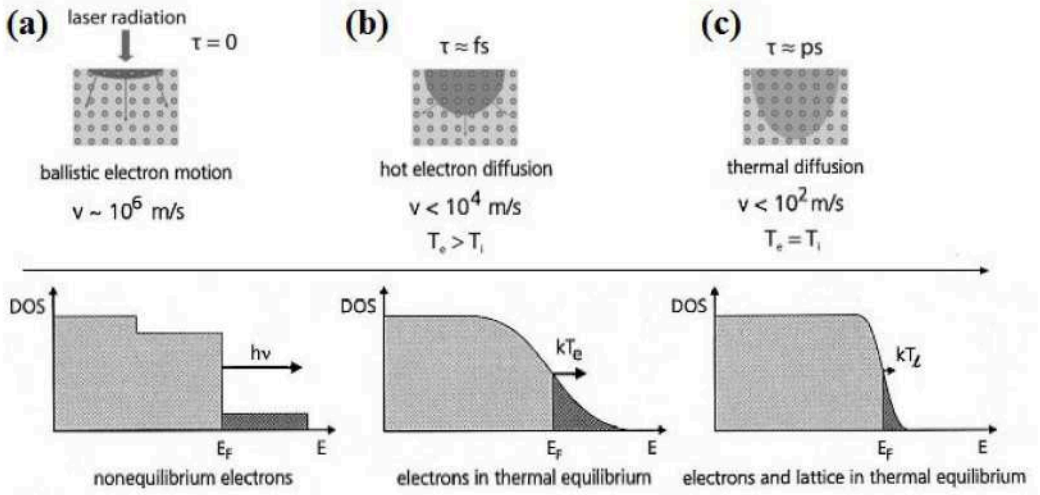

Figure 3.3: Three processes of excited carrier thermalization by ultrafast laser pulse in metals. (a) Photon absorption within the optical penetration depth generates ballistic electrons which move with high velocity into deeper parts of the sample. (b) Diffusive energy transport starts within the electron gas by electron-electron collisions forming the equilibrium electron subsystem with a Fermi distribution at electron temperature Te. (c) The electron-lattice comes into equilibrium state via electron–phonon coupling, energy transport now proceeds by lattice thermal diffusion [HWG+00].

In semiconductors, there are three separate processes in carrier-carrier scattering: electron-electron scattering, hole-hole scattering, and electron-hole scattering [SM02]. All three play a role in carrier thermalization on different time scales. The time scale for electron-electron scattering deceases with increasing conduction electron density and it is less than 20 fs for electron densities greater than 10^{18} cm^{-3} in GaAs [LSF88].

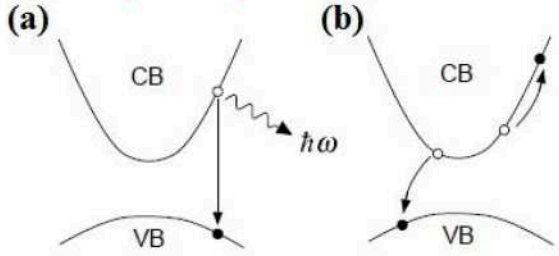

Figure 3.4: Relaxation processes in semiconductors: (a) radiative recombination, (b) Auger recombination [Hua97] .

In various materials the excited carriers relax also in terms of population number. To exemplify in the case of semiconductor, free electrons and holes can recombine in the radiative or non-radiative way, shown in Fig. 3.4.

Electron-phonon non-equilibrium: in ultrashort laser irradiation, the laser pulse duration is shorter than the energy relaxation within the electron-lattice system, resulting in the strong nonequilibrium

system including the electron subsystem and lattice subsystem (Fig. 3.3(b)). To describe the nonequilibrium system, Anisimov *et al* proposed the one-dimensional two-temperature model (TTM) [AKP74]:

$$C_e(T_e)\frac{\partial T_e}{\partial t} = \frac{\partial}{\partial x}\left(K_e \frac{\partial T_e}{\partial x}\right) - G(T_e - T_l) + S(x,t) \tag{3-9}$$

$$C_l(T_l)\frac{\partial T_l}{\partial t} = \frac{\partial}{\partial x}\left(K_i \frac{\partial T_i}{\partial x}\right) + G(T_e - T_l) \tag{3-10}$$

Here T_e and T_i denote the electron and lattice temperatures respectively, C_e and C_i are the electron and lattice heat capacities per unit volume respectively, G is the electron-lattice coupling coefficient, K_e and K_i are the electron and lattice thermal conductivity respectively, $S(x,t)$ is the heat flux. Considering the Gaussian laser pulse and ballistic electron range, the heat flux is described by [HWG+00]

$$S(x,t) = 0.94\frac{1-R-T}{t_p(\delta+\delta_b)} J \cdot \exp\left[-\frac{x}{(\delta+\delta_b)} - 2.77\left(\frac{t}{t_p}\right)^2\right] \frac{1}{\left\{1-\exp\left[-\frac{d}{(\delta+\delta_b)}\right]\right\}} \tag{3-11}$$

Here R and T denote reflectivity and transmissivity respectively, J is the absorbed fraction of the incident intensity, δ is the optical penetration depth, δ_b is the ballistic electron range, d is the film thickness on sample surface and t_p is the laser pulse duration.

The last step is the material removal following the temperature increase at the level of the lattice. Thermal processes occur after the carrier-phonon relaxation and final lattice temperatures can be calculated according to the two-temperature model. The material response in the laser ablation is not only controlled by the physics of coupling the optical energy into the material, but also by the subsequent thermodynamics, following with the generation of a liquid-solid interface and a vapor plume above the surface.

The mechanisms of matter removal via specific thermodynamic trajectories can be visualized by the time evolution of the system in the phase space. Particularly instructive is the visualization in the ρ-T plane [LLM03] as it shows the material evolution via the local density. A schematic overview of the thermodynamic pathways of a hypothetical semiconductor or metal under laser irradiation is depicted in Fig. 3.5 and this is discussed below:

Thermodynamic phases in laser ablation including solid, liquid, gas, warm dense matter (WDM) [Gra14] and plasma. Binodal line is a boundary between the one-phase region (vapor, liquid, supercritical) and the two-phase region (gas-liquid). Spinodal line is

the coexistence of stable and unstable states and the boundary of absolute instability. The common vertex of binodal and spinodal lines is the critical point. The metastable regions (super-cooled gas and superheated liquid (SHL)) are in the regions between the binodal and spinodal lines.

Under fs irradiation, isochoric heating results in a strong compression and pressure increase in the material in the GPa domain. Later the pressure is released via adiabatic mechanical expansion. At high energies, the rapid expansion causes the transition into plasma and gas phases without crossing a liquid boundary, through fragmentation (A-A"-U). In contrast, at the middle energy density domain, closer to the ablation threshold, the excited material enters the metastable regime near the spinodal limit in adiabatic cooling (A-A'-W-Y). Then the metastable material converts into a mixture of liquid and gas via the homogeneous bubble nucleation (Y-Z).

In the case of nonisochoric heating, the excited material cools along the binodal line by thermal diffusion towards the liquid-gas regime (B-B'-W), The ablation by fragmentation only occurs in the regions above the critical point.

In the case of slow heating with a slow expansion along the binodal limit, the material likely reaches the critical point where phase separation occurs. For laser duration τ>100 ns, surface evaporation may also occur.

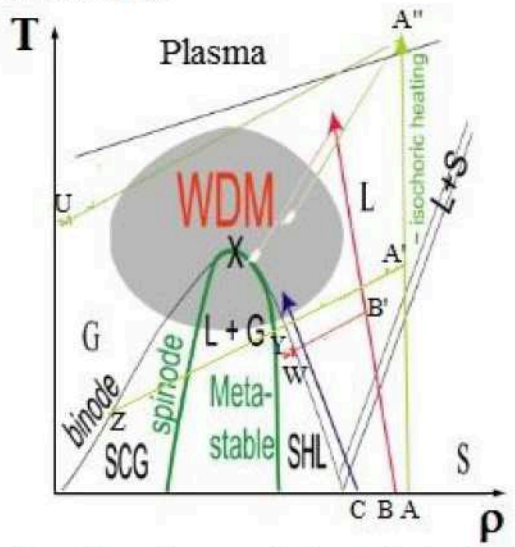

Figure 3.5: Thermodynamic pathways of a hypothetical semiconductor or metal under laser irradiation. Thin black line: binodal; thick green line: spinodal; cross: critical point. L: liquid; G: gas. SCG: supercooled gas. SHL: superheated liquid. [LLM03]

From Fig. 3.5, the ablation mechanisms by ultrafast laser irradiation are summarized as follows: (a) Near-threshold ablation (A-A'-Y-Z) involving the rarefaction wave [SBC+98], bubble and

liquid generation, and shock wave in the time domain from hundreds of ps to tens of ns after excitation [RSL+02]. (b) Fragmentation (A-A"-U) involving the generation of WDM and plasma. (c) Explosive boiling (Y-Z near the critical point) meaning a rapid transition from a superheated liquid to a mixture of vapor and liquid droplets with an explosive development of nucleation centers. (d) Ultrafast melting involving heterogeneous nucleation (at possible defects on material surface at melting point T_m), homogeneous nucleation (at temperatures $T>1.5\times T_m$), as well as non-thermal melting (ionic deformations faster than the picosecond time scale of thermal melting [SBJ+03]). (e) Critical point phase separation (CPPS) [VJL+01] (A-A"-X) involving the spinodal decomposition near the critical point.

In total, the ablation mechanisms mentioned above and their characteristic time scales are summarized in Fig. 3.6.

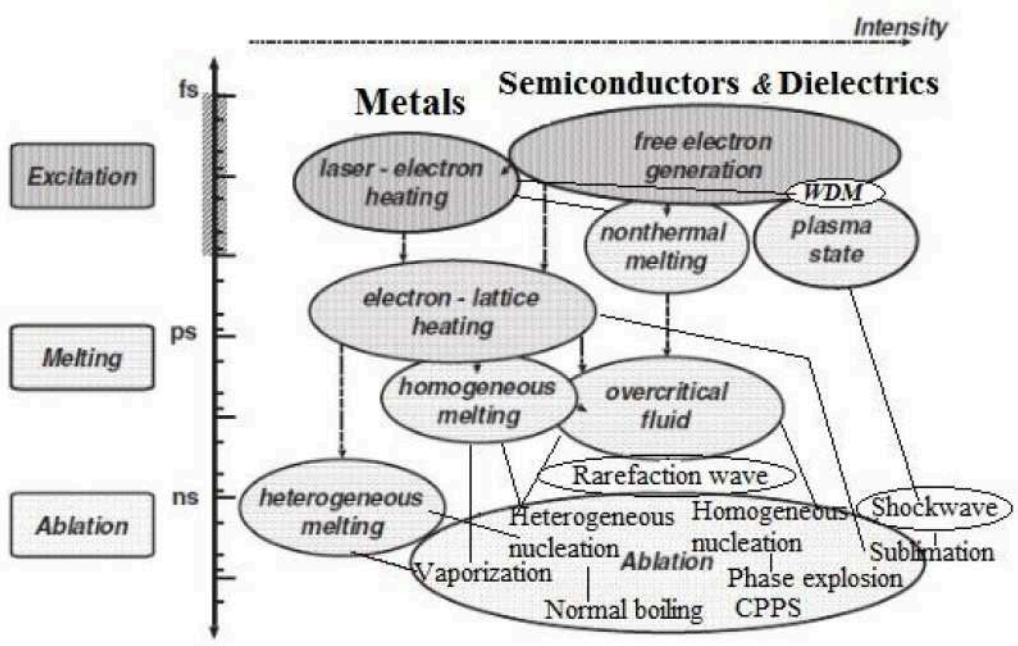

Figure 3.6: Map of excitation/ablation mechanisms and their characteristic time scales (based on [RSL+04]).

After ablation, the re-solidification or condensation of excited material takes place as the temperature of lattice decreases below the melting or boiling points respectively. However, some changes occur in the surface layer. For example, a micro-crater is formed after evaporation and ablation. In addition, material phase may be changed after ablation. Examples involve a range of structural transitions occurring either under pressure drives or by rapid cooling from liquid phases. An illustrative example is the transition from crystalline to amorphous phases in GeSb films [SSB+98] but

graphite to diamond transitions [IKM+15] or crystalline changes in metals [SMG+14] are equally seen.

3.3 Transient responses of metals to ultrafast laser

The dielectric function is an intrinsic material property, related to the electronic configuration and lattice structure. Any variation in the electronic configuration or lattice structure can change the dielectric function. Transient responses of metals to ultrafast laser radiation involve complex processes related to the electronic configuration and lattice structure, such as the photo-excitation of s/p- and d-electrons, electron-electron thermalization, changes of electronic configuration, electron-lattice thermalization, lattice disorder and so on. The complex processes in excited metals are briefly introduced in the three aspects of electronic effects, lattice structure effects and plasmonic effects in the following:

3.3.1 Electronic effects

Irradiating metals by ultrashort laser pulses (in the order of sub-picosecond) can result in a significant rise of the electronic temperature while preserving at the same time a cold ionic lattice. Such extreme nonequilibrium on picosecond time scale impact the excited material properties in terms of optical coupling, transport characteristics and phase transitions. The extreme nonequilibrium state triggers new thermodynamic regimes for highly excited solid materials including the excitation-dependent band structure evolution.

At first, the variation of electronic configuration and transient optical responses to ultrafast laser radiation are introduced by the example of metal gold. Fig. 3.7 shows the schematic of the density of energy states (DOS) of gold [HWG+00]. The free electrons are in the s/p band. The energy difference between Fermi energy E_F and the top of the d band is 2.47 eV (502 nm), called interband transition threshold (ITT). For the excitation photon energy below ITT, only free electrons are excited and the d band is not perturbed. However, for the excitation photon energy above ITT, electrons in the d band are excited and absorb the energy.

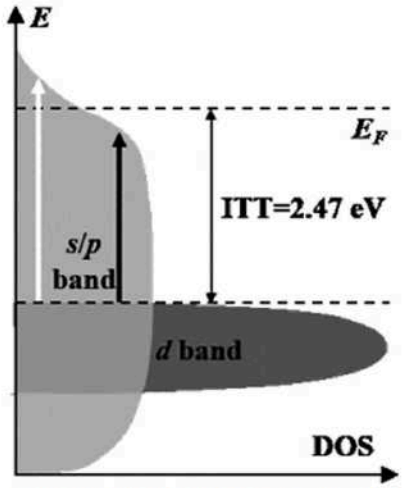

Figure 3.7: Schematic of the DOS of gold [HWG+00].

Under ultrafast laser irradiation, the electronic configuration of gold changes, leading to the transient optical responses. For example, the transient reflectivity of gold excited by 800-nm (1.55 eV) fs pump and with fs probes of varying wavelengths is depicted in Fig. 3.8, showing that the transient optical dynamics are related to the variation of electronic configurations [GX14].

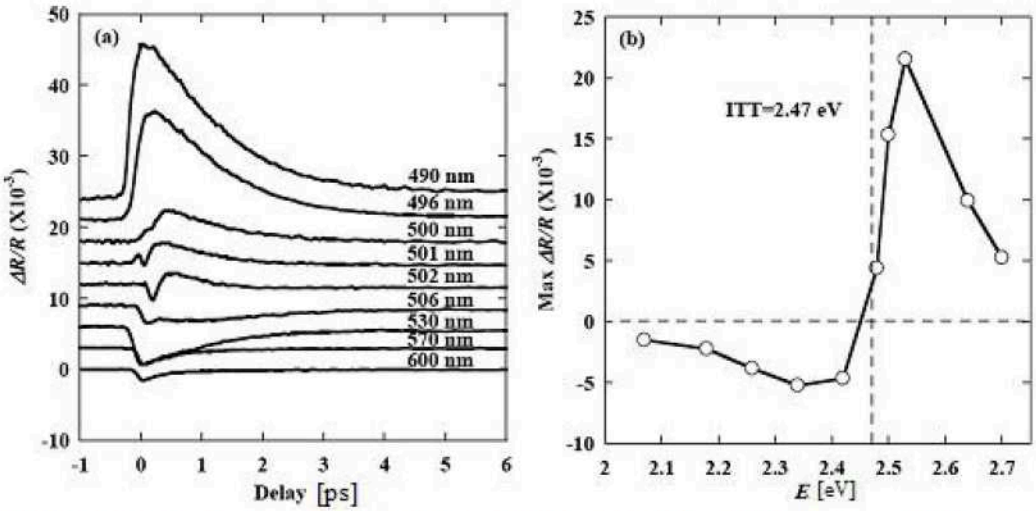

Figure 3.8: (a) Transient reflectivity of gold excited by 800nm pump-photons at 5.28 mJ/cm^2 fluence and probed by varying wavelengths, with curves shifted vertically for clarity. (b) Dependence of the amplitude of the transient reflectivity on the probe photon energy (the vertical dashed line marks the energy for ITT) [GX14].

For 150-fs pump at higher photon energy of 3.1 eV (400 nm) and the fs probe with the associated spectrum varying from 1.50 eV to 2.85 eV, the transient dielectric function of the warm dense gold are shown in Fig. 3.9, showing the dielectric function dynamics of intraband (below 2.37 eV) and interband (above 2.37 eV) components [PCO+09]. Typically, the intraband components of

dielectric function can be fitted well by the Drude model (Fig. 3.9(b)), revealing that the free electrons play the main role in the dynamics of intraband components of dielectric function.

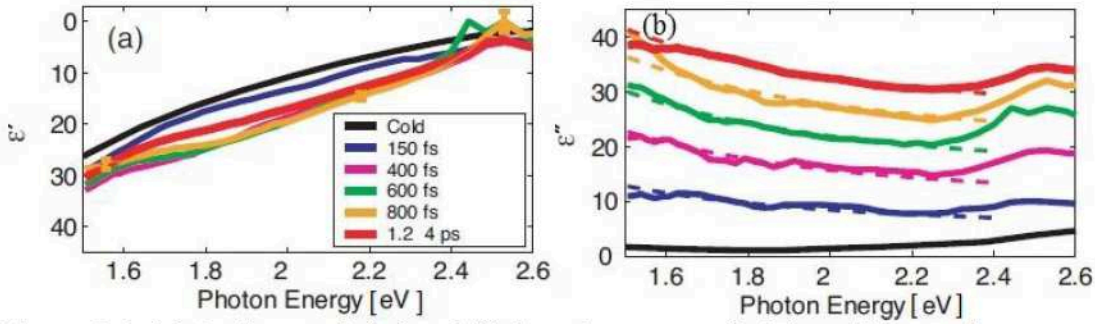

Figure 3.9: (a) Real part of ε(ω) and (b) imaginary part of ε(ω) at different times for an energy density of 2.9×10^6 J/ kg with an off-set of +5 along the vetical axis between time steps. Sample error bars are included in (a). The dashed curves are best-fit Drude functions [PCO+09].

For warm dense gold, because of the increase of the collision frequency due to the excitation of d-band electrons, collision frequency γ in Drude model significantly deviates from the T_e^2 scaling [MR13]. C. Fourment *et al* [FDD+14] used a pump-probe frequency domain interferometry to measure the collision frequency, and found that collision frequency γ increases linearly with T_e, shown in Fig. 3.10. To these, additional effects such as a global variation of the number of free electrons as a function of T_e with associated shift in the density of states can play a role [BCR+14], giving an intricate effect of population and collision effects.

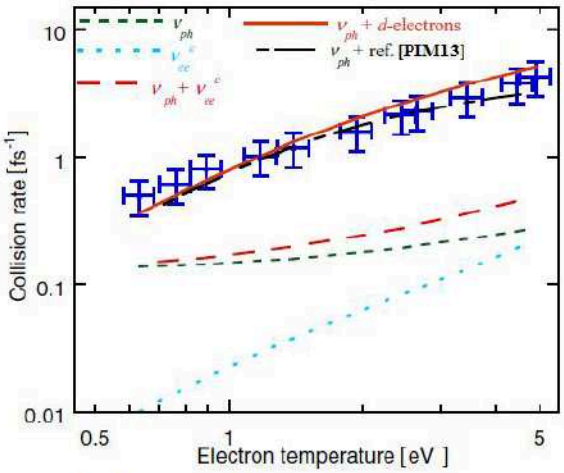

Figure 3.10: Measured electron damping rate as a function of T_e (blue experimental points), and the contributions from collision with phonons (ν_{ph}) and electrons in the conduction band (ν^c_{ee}) [FDD+14]. The sum of both contributions is depicted in the red dashed line. Also plotted are the collision frequencies due to the phonons and d-band electrons according to our simple model (solid line), and due to phonons and electrons according to the Petrov et

al. calculation [PIM13].

Other metals with different electronic configurations may have different transient optical response to ultrafast laser heating. For simple metals (Na, Mg, Al, etc.), s/p-electrons contribute to the optical processes. However, for transition metals, such as Ni, Cu, Au, W, Ti and so on, d-electrons with a higher degree of localization than s/p-electrons can still participate to the optical and at the same structural response, potentially by the electron confinement within more or less diffuse orbitals. In addition, the increase of the electronic temperature strongly changes the shape of the d-band [RCZ+06]. In transition metals, the strong adjustments of the electronic structures are related to the variations of electronic occupation in localized d bands, via change in electronic screening and electron-ion effective potential, leading to the corresponding changes of electronic chemical potentials, free-electron numbers, electronic heat capacities, and electronic pressures. These serve as a base to correctly describe ultrafast structural dynamics, ablation dynamics and phase transitions [BCR+14].

E. Bévillon *et al* [BCR+14] in our group performed a systematic study on the electronic behavior of a free-electron-like metal (Al) and the transition metals (Ni, Cu, Au, W and Ti) by first-principle calculations with the Abinit package based on the density functional theory (DFT), which reveals that density of states (DOS) exhibit different dynamics with the increase of the electronic temperature T_e and the Fermi smearing across the chemical potential: (a) the DOS of Al is almost insensitive to Te; (b) transition metals with d-block fully or almost fully occupied by electrons (Ni, Cu and Au) exhibit a shrinking and a strong shift of the d-block toward lower energies as T_e increases; (c) transition metals with partially filled d-block (Ti and W) display an expansion and a shift toward higher energies of their d-block as T_e increases (minimal for W). In addition, during the ultrafast heating, the effective free electron number per atom N_e can be estimated, shown in Fig. 3.11, revealing the different dynamics of ultrafast laser-induced effective free-like electrons with the increase of T_e.

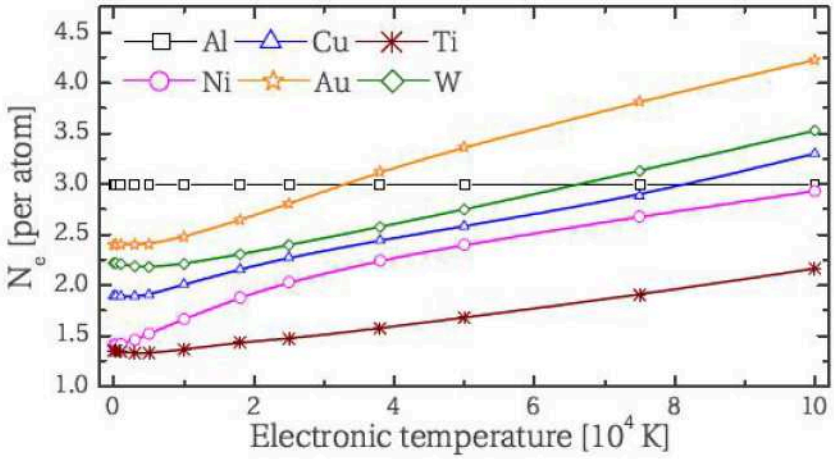

Figure 3.11: Evolution of the number of free electrons per atom (Ne) with the increase of Te for the metals Al, Ni, Cu, Au, W and Ti.

3.3.2 Lattice structure effects

Photo-induced structural dynamics of crystals have been directly studied by femtosecond electron [SDJ+03] and x-ray [LLS+05, CCTR11] diffraction combining atomic scale spatial and femtosecond temporal resolution. Under strong optical excitation, the lattice response is determined by the rate of energy transfer from the excited electrons to the nuclei and the instantaneous effect of change in electron distribution on the interatomic potential energy landscape [EHH+09].

The solids with different bonding characteristics have specific dynamics of the order-to-disorder structural transition. For example, in the canonical free-electron metals like Al, the lattice stability appears to be almost unaffected by optical excitation [RCZ+06]. However, for gold, strong electronic excitation affects the screening of the attractive inter-nuclear potential, resulting in a hardening of the lattice [EHH+09].

3.3.3 Plasmonic effects

When light waves interact with metallic surfaces, the resulting electron density wave that propagates along the surface of the metal, called as a surface plasmon polariton (SPP) [Mai07]. SPPs can be excited by phase-matching techniques.

When ultrashort laser pulses incident on the metal surface disturb the equilibrium in the energy–momentum distribution of electrons, the variation of optical properties can affect SPP propagation along the surface. Thus, via the electronic temperature and electronic redistribution, the process can take a nonlinear aspect.

The nonlinear interaction between a propagating SPP and a fs laser pulse takes place in the femtosecond timescale, which can be used to modulate the propagating SPP [MSS+09]. One example is the plasmonic interferometry on structured surfaces in the presence of light excitation [TNA+09].

3.4 Transient responses of semiconductors to ultrafast laser

Transient responses of semiconductors to ultrafast laser radiation also involve additional complexity related to the electronic configuration and the lattice structure, such as the photo-excitation of electron-hole pairs, carrier thermalization, carrier relaxation, carrier diffusion and so on. Most details of these processes have been introduced in section 3.2. The carrier excitation and relaxation can change the electronic configuration in semiconductors, resulting in the changes of optical properties [Hua97].

Several physical effects in electronic configuration are responsible for the changes of the optical properties of the semiconductor state: band filling, renormalization of the band structure and the free-carrier response [SL00]. Assuming the three effects contribute to the dielectric constant separately, the dielectric function of an optically excited semiconductor is derived [SL00]:

$$\varepsilon^{*} = \varepsilon_{g} + \Delta\varepsilon_{\text{pop}} + \Delta\varepsilon_{\text{bgs}} + \Delta\varepsilon_{fcr} \tag{3-12}$$

where ε_g is the dielectric constant of the unexcited semiconductor, $\Delta\varepsilon_{pop}$ is the changes of dielectric constant due to the state and band filling [BA82], $\Delta\varepsilon_{bgs}$ is the changes of dielectric constant due to the band-structure renormalization, $\Delta\varepsilon_{fcr}$ is the changes of dielectric constant due to free carriers. Band-structure renormalization describes the changes of the single-particle energy in the carriers because of the many-body interactions in the excited plasma, which was treated as a rigid shift of the band structure, leading to the shrinkage of the energy gap. The changes of the optical properties due to the band-structure renormalization were described by the rigid band shift model [RZW+90].

The changes of the optical properties due to the free carriers can be described by the Drude model [SL00]

$$\Delta\varepsilon_{\text{fcr}} = -\frac{N_{e-h}e^{2}}{\varepsilon_{0}m_{opt}^{*}m_{e}\omega^{2}}\frac{1}{1+i\dfrac{1}{\omega\tau_{D}}} = -\left(\frac{\omega_{P}}{\omega}\right)^{2}\frac{1}{1+i\dfrac{1}{\omega\tau_{D}}} \tag{3-13}$$

Here ε_0 is the electric permittivity of free space, e is the electric charge, m_e is electron mass, ω is the oscillating frequency of the

electromagnetic wave, m_{opt} is the optical effective mass of the carriers, τ_D is Drude damping time, and ω_P is the plasma frequency. In the case of silicon, m_{opt}=0.15 for low-density relaxed plasmas, however, m_{opt} is dependent on the density and temperature. $\tau_D \approx 100$ fs for low densities of plasma in silicon, however, $\tau_D \approx 1$ fs for higher densities. [SL00]. The dielectric function on ultrafast scales is determined by the creation and relaxation of the electron-hole plasma.

Excitation by ultrafast laser pulses can induce the changes in the semiconductor lattice by two mechanisms. One mechanism is the thermal melting, with the energy transferring from carriers to lattice. This is typically regulated by electron-phonon coupling up to the achievement of a molten phase via a mix of heterogeneous and homogeneous processes. The other one is the non-thermal melting due to the lattice instability induced by intense optical excitation. As the conduction band has typically an antibonding character, strong excitation and pumping of CB bands weakens the covalent bonding, and softens the lattice, resulting in electronically driven disordering of the lattice [RCZ+06]. Displacive excitation and anharmonicity can lead to the collapse of transverse phonon modes and a depart from crystalline stability. Consequently the semiconductor may lose the lattice structure and undergo a phase transition by the destabilization of the bonds and softening of phonon modes in less than 1 ps, in a trajectory which is not driven by temperature.

In the case of silicon, for fluences near F_{melt}, the solid-liquid phase transition is a slow, thermal process occurring on a 10 – 100 ps time scale. For higher fluences above F_{melt}, melting occurs on a sub-picosecond time scale, and these effects should be accounted for in ablation scenarios.

3.5 Conclusion

In this chapter, we review the optical properties of solids and the transient responses of solids to ultrafast laser radiation, involving the metals and semiconductors. The dielectric function is an intrinsic material property, related to the electronic configuration and lattice structure. Any variation in the electronic configuration or lattice structure can change the dielectric function.

We equally review main processes in ultrafast laser-matter interaction: the deposition of laser energy in the material, the excitation of electrons by absorbing photons, excited carrier thermalization which can be described by two-temperature model

(TTM), excited carrier decay in semiconductors and dielectrics, as well as material removal which can be determined by the time evolution of the material thermodynamic trajectories.

Transient responses of metals to ultrafast laser radiation are briefly introduced with three dominant aspects: (a) electronic effects contribute to the intraband and interband components of dielectric function. Fermi smearing and contribution from low lying orbitals are major components in modifying the dielectric function; (b) lattice structure effects, with the corresponding dynamics of the order-to-disorder structural transition due to intense laser excitation; (c) plasmonic effects, where femtosecond laser pulse can excite and control a propagating SPP.

Transient responses of semiconductors to ultrafast laser radiation involve additional complexity related to the electronic configuration and lattice structure, electronic effects, state and band filling, renormalization of the band structure, as well as the free-carrier response are responsible for the optical response. With respect to structural effects, excitation by ultrafast laser pulses can induce the changes in the semiconductor lattice by thermal heating and the faster non-thermal melting.

These serve as a base to correctly describe ultrafast structural dynamics, ablation dynamics and phase transitions.

Chapter 4

Dynamics of excited materials: Experiments of time-resolved reflectometry and ellipsometry

In this chapter, we developed time-resolved reflectometry and ellipsometry techniques that enable access to the optical indices of excited materials. The dynamic measurements of the transient optical properties of several materials are carried out and discussed respectively, including single-crystal silicon, tungsten, and Zr-based bulk metal glass (Zr-BMG). The objective is the gains of transients in optical coupling potentially intervening in LIPSS formation.

By time-resolved ellipsometry experiments, we aim to gain information about dynamics of excited materials by measuring their transient optical properties. The ultrafast laser-matter interaction is examined by measuring the changes of reflectivity and retrieving thus relative variations of the dielectric function in the vicinity of the ablation threshold. The dielectric function is intrinsically related to the electronic configuration and lattice structure. Our measurements show complex dynamic processes involved in affecting optical properties in metals and semiconductors excited by ultrafast pulses. We then use first principle simulations to reveal how the electronic configuration changes during the excitation, responsible for the measured optical transients. The measured results of excitation effects on the optical properties of single-crystal silicon, tungsten and Zr-based bulk metal glass (Zr-BMG) are introduced and

discussed respectively in the following, emphasizing their potential influence on LIPSS.

4.1 Time-resolved ellipsometry

In order to measure the transient responses of matter to ultrafast laser, a pump-probe method is often used in optical techniques, in which the matter is excited by a strong pump pulse and then the resulting changes are probed by a weak probe pulse in a time-resolved manner. The probe pulse is delayed with respect to the pump pulse by controlling an optical delay path. There are several probing techniques, including the linear (transmission, reflectivity) and nonlinear (SHG, Raman scattering, luminescence). Among these probing techniques, reflectivity measurement is the simplest of the pump-probe techniques. Single angle reflectivity measurement can't obtain both real and imaginary parts of the dielectric function. However, the dielectric function can be determined by measuring reflectivity at two angles, which forms the present concept of reflectrometry/ellipsometry. Time-resolved ellipsometry can provide the information on both carrier and lattice dynamics following the excitation. Thus we use a dual-angle time-resolved ellipsometry technique to measure the transient changes of optical indices in the matter during ultrafast laser ablation.

A regenerative Ti: sapphire oscillator-amplifier system (Concerto Inc) based on the chirped-pulsed amplification technique at a central wavelength of 800 nm with pulse duration of 150 fs and repetition rate of 1 kHz was used to perform the experiments. As a pump, the linearly polarized Gaussian laser was focused at the sample surface with a convex lens of focal length f=500 mm down to a spot of 110 μm. The laser fluence was adjusted using the combination of a waveplate and a polarizer. The number of pulses is controlled by laser shutter. The sample was mounted on a computer-controlled XYZ translation stage. All experiments were performed in an ambient atmosphere.

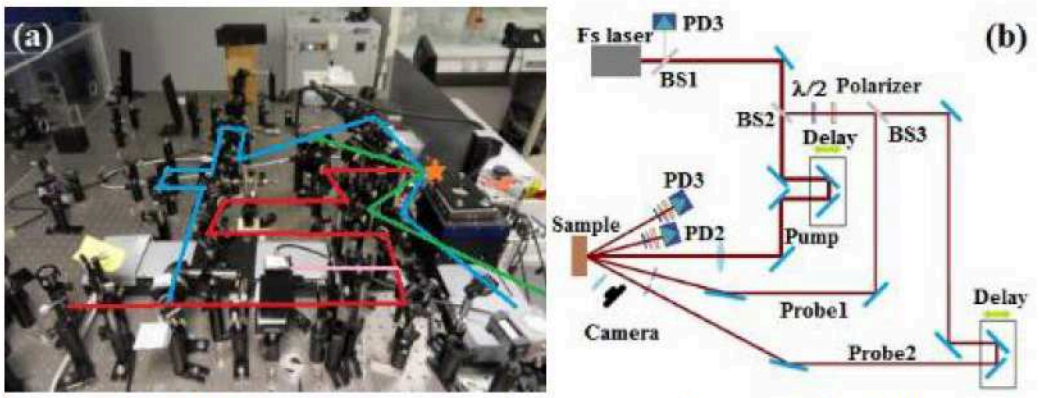

Figure 4.1: (a) Photographic image of experimental time-resolved ellipsometry setup. (b) Schematic of time-resolved ellipsometry arrangement.

Fig. 4.1(a) shows the photographic image of the experimental time-resolved ellipsometry setup, and Fig. 4.1(b) shows the schematic of time-resolved ellipsometry arrangement, which was built according to Ref. [RKC+03]. The s-polarized pump pulse of 150 fs 800 nm arrives at normal incidence on the sample surface and excites the material, determining the changes of transient reflectivity. The 150 fs 800 nm low energy non-perturbing double probes measure reflectivity changes at two different incident angles 28.7° and 65.8° at the same time, which allows for recovery of changes in the refractive index. Two incident angles are chosen according to the reflectivity of unexcited silicon, which has been shown in Fig. 3.2. The single pump pulse arrives at a variable time delay with respect to the double probe pulses. After a beam splitter BS2 and a half-wave plate, probe pulses change into p-polarization before the sample. The superposition of the three laser spots on the sample is monitored by a CCD-camera with a 20×zoom objective. The probed zone is significantly smaller than the spatial extent of the pump excited region and therefore assures that the two smaller probe beams probe a preferably uniformly excited region of the sample. Two photo-diode detectors (PD1, PD2) are used to measure the probe signals. In order to minimize scattered light from s-polarized pump pulse, high-contrast polarizers are used before two photo-diode detectors. To minimize the influence of fluctuations in laser, another photo-diode detector (PD3) is used to measure the fluctuations of the laser fluence. The measured values of the transient reflectivity are recorded and controlled by a LabVIEW program. The corresponding complex refractive index $\tilde{n}=n+k\mathrm{i}$ with different delay times are obtained by inverting Fresnel formulas at the given angles. The accuracy of the measurement is affected by the roughness and local planarity of the sample surface.

Next, we used the time-resolved ellipsometry setup to measure the transient optical properties of several materials. At first, single-crystal silicon was the first object, as many previous experimental results [ACS84, CC88, Hua97, SL00] can be used to check the effectiveness of our experimental setup. Secondly, the non-plasmonic metal tungsten is measured to investigate the effect of d-band electrons. At last, the amorphous alloy Zr-based bulk metal glass (Zr-BMG) is measured to research the ionic structure effect.

4.2 Transient responses of silicon to ultrafast laser

4.2.1 The electronic and optical properties of single crystal silicon

At first, the electronic and optical properties of unexcited silicon are briefly introduced. The band structure of the silicon is shown in Fig. 4.2(a). Si has the nearly parallel dispersion of the lowest conduction and the highest valence bands, where the maximum of the valence band is at the G-point while the minimal of the valence band is near the X-point, leading to the indirect minimum bandgap of 1.12 eV. Consequently, the dielectric function in Fig. 4.2(b) shows a very large imaginary part between 3.2 and 4.3 eV [Hua97].

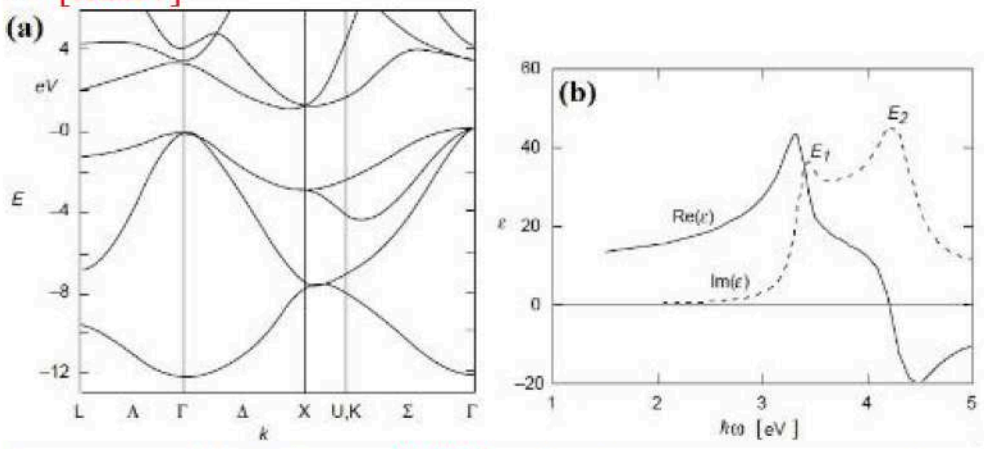

Figure 4.2: (a) Band structure [CC88] and (b) the dielectric function of single-crystal silicon [Pal85].

4.2.2 Measurement of multi-pulse modification thresholds on silicon

The polished (100) surface of n-doped single crystal silicon samples (ITME product) are used in the experiment. The

modification threshold of silicon is dependent on laser wavelength, pulse duration, pulse number and the base temperature of silicon [BBK+02]. For example, the modification threshold on (111) surface of n-doped silicon induced by 800 nm 130 fs laser pulses is 0.26 J/cm^2 [BBK$^+$02]. Before measuring the transient optical indices in excited silicon, we investigate the modification thresholds of silicon samples.

Because of incubation effect, the modification thresholds depend on the number of applied laser pulses. In reference [PER$^+$91], the dependence was found in the form of a power law:

$$F_{\mathrm{mod}}(N) = F_{\mathrm{mod}}(1) \cdot N^{\xi-1} \qquad (4\text{-}1)$$

Here $F_{\mathrm{mod}}(N)$ is the modification threshold fluence for laser pulse number N, ($F_{\mathrm{mod}}(1)$=0.21 J/cm^2 according to experiment data for Si), and ξ is a coefficient, which is dependent in material and reflect a certain fatigue. In Fig. 4.3, the experiment data of modification thresholds depending on the number of pulses are plotted. A least-squares-fit with formula (4-1), yields a coefficient ξ of 0.89, close to the coefficient in reference [BBK$^+$02]. For the finite pulse number N, when the laser fluence is lower than $F_{\mathrm{mod}}(N)$, laser will not modify the silicon surface. So the transient optical indices in excited silicon are measured below the laser fluence of 0.0825 J/cm^2.

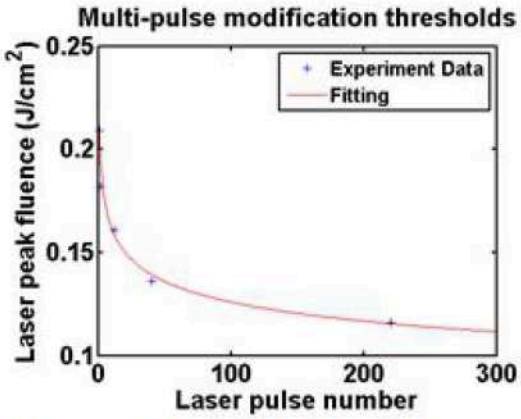

Figure 4.3 Threshold fluence of laser-induced modification of silicon versus the number of incident laser pulses with a duration of τ=150 fs and λ=800 nm in an air environment. The solid line represents a least-squares-fit with formula (4-1), where ξ= 0.89.

4.2.3 Measurement of the transient optical indices of excited silicon in large pump fluence range

For the pump fluence below the modification threshold, the sample is immobile during the measurements and all the pump pulses are shot at one same spot on the sample in order to diminish

the noise from the roughness of silicon sample. However, for the pump fluence close to or above the modification threshold, the silicon sample was raster scanned during the measurements by a two-axis translation stage in order to ensure that each pump pulse strikes a fresh, unexcited area on the silicon surface.

Fig. 4.4 depicts the transient changes of reflectivity at the incident angle of 28.7° and 65.8° following the excitation for different pump fluences and the corresponding time-resolved refractive indices $\tilde{n}=n+k\mathrm{i}$ are retrieved by inverting Fresnel formulas.

As the fluence of the pump pulse is below single-shot modification threshold, both reflectivities at the two angles undergo a fast drop in about 1 ps followed by a slower recovery (Fig. 4.4(a)). Correspondingly, the real part n of refractive index undergoes a fast drop followed by a slower recovery, however, the imaginary part k of refractive index experiences a fast increase followed by a slower recovery.

As the fluence of the pump pulse is varied from 0.256 J/cm^2 up to 0.611 J/cm^2 above single-shot modification threshold, both the reflectivity at the two angles undergoes a fast increase in about 1 ps followed by a quasi-steady-state (QSS) in about 5 ps (Fig. 4.4(b-d)). Correspondingly, the real part n of refractive index undergoes a fast drop followed by a quasi-steady value of about 0.66, however, the imaginary part k of refractive index experiences a fast increase followed by a quasi-steady value of about 1.84. After the pulse duration of 150 fs, the real part n starts to be smaller than the imaginary part k of the refractive index, representing that the QSS is the metal-like state, as evidenced by the negative real part of dielectric function for most typical metals. So the transition from the semiconductor to the metal state from an optical point of view occurs in ultrafast laser ablation at high energy (when typically 10% of the valence band is pumped in the conduction band).

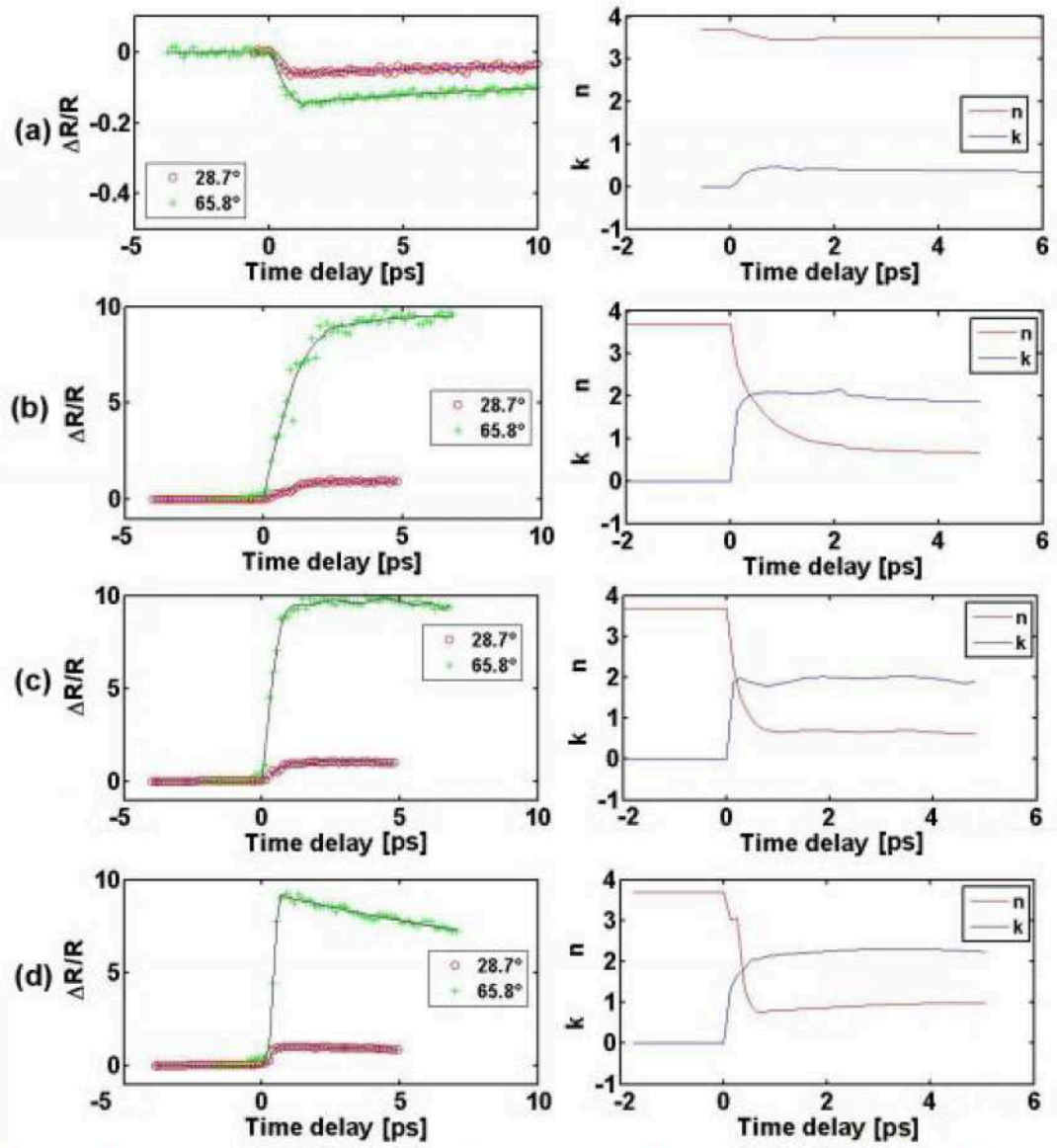

Figure 4.4. Transient changes of reflectivity in silicon at the incident angle of 28.7° and 65.8° following the excitation and the corresponding retrieved time-resolved refractive indices $\tilde{n}=n+ki$ at the pump fluence of (a) F=0.084 J/cm^2; (b) F=0.256 J/cm^2; (c) F=0.318 J/cm^2; (d) F=0.611 J/cm^2.

The experimental transient changes of reflectivity in the laser-excited silicon are analyzed from the perspective of electronic configuration. Because the free carriers dominate the optical response of the excited material in the early stages [SL00], it is appropriate to describe the transient dielectric function of the excited silicon by Drude model. Except other effects, such as state and band filling, band-structure renormalization, the dielectric permittivity is given by the Drude model [SL00]:

$$\varepsilon' = \varepsilon_g + \Delta\varepsilon_{Drude} \qquad (4\text{-}2)$$

$$\Delta\varepsilon_{Drude} = \frac{-e^2 N_e}{\varepsilon_0 m_{opt} m_e \omega^2 (1+\frac{i}{\omega\tau})} \tag{4-3}$$

Here ε' is the dielectric constant of the excited silicon, ε is the dielectric constant of the unexcited silicon, $\varepsilon_g=\tilde{n}^2=(3.6959+0.0047i)^2=13.6597+0.0347i$; Other parameters have been introduced in Chapter 3.4. According to reference [BRK09], $m_{opt}=0.18$ and $\tau=1.1$ fs are chosen for femtosecond-laser-excited silicon. So the free carrier density N_e can be calculated based on the refractive indices in the excited silicon using the formula (4-2) and (4-3).

Before the Drude model is used to analyze our reflectivity, we briefly introduce the absorption of light in solid silicon. In silicon, electron-hole pairs are created by linear and by two-photon absorption (TPA). Neglecting recombination and diffusion during excitation, as well as the changes of the reflectivity R during the pump pulse, the free carrier density in NIR femtosecond-laser-excited silicon can be calculated from the pump fluence F_0 [SL00]:

$$N_{e-h} = F_0 \frac{(1-R)}{\hbar\varpi}\left[\alpha_0 + \beta F_0 \frac{(1-R)}{2\sqrt{2\pi}t_0}\right] \tag{4-4}$$

Here α_0 describe the linear absorption coefficient, $\alpha_0=1.1\times10^3$ cm^{-1} [Pal85]. β is the two-photon absorption coefficient, β=6.8 cm/GW [BRK09]. Reflectivity $R(\theta=0°)=0.33$, according to experiment data, $\hbar\omega$ is the photo energy, $\hbar\omega$=1.55eV (λ=800 nm), t_0 is the pulse duration, t_0=150 fs. According to the pump fluences in the experiments and equation (4-4), the free carrier density is calculated and drawn in Fig. 4.5. Fig. 4.5 shows that the excited free carrier density increase nonlinearly with the increase of laser fluence.

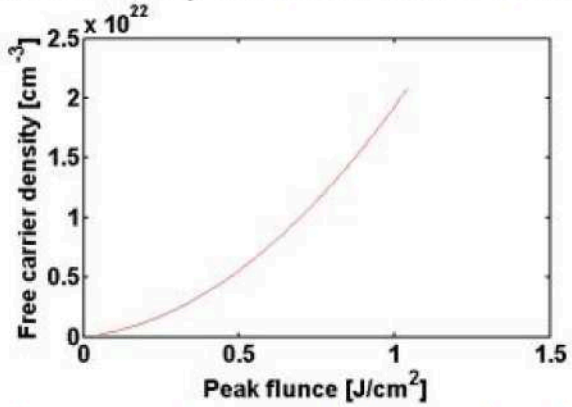

Figure 4.5: Free carrier density as the function of excitation fluence.

Then according to the Drude model (4-2) and Fresnel formula (3-8), the reflectivity at the incident angles of 28.7° and 65.8° are respectively calculated and drawn in Fig. 4.6(a) and (b).

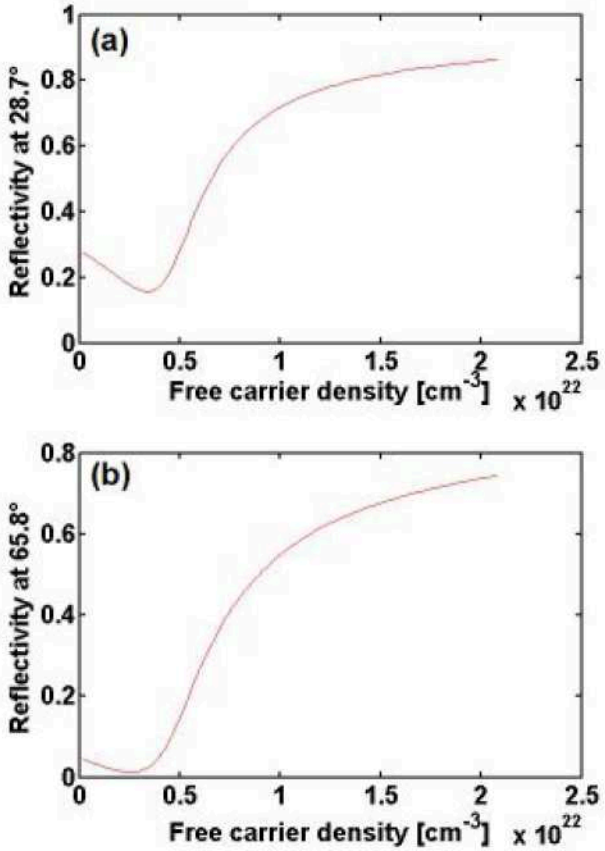

Figure 4.6: Theoretical predictions for the reflectivity of silicon as a function of the excited carrier density at 800-nm wavelength and *p* polarization at the incidence angle of (a) 28.7° and (b) 65.8°.

Fig. 4.6 shows that the main reflectivity features are the decrease at lower densities and a drastic increase at higher densities, in which the reflectivity minimum corresponds to the density where the real part of ε' is equal to 1. The reflectivity start to increase when the carrier density exceeds the critical density N_{cr} corresponding to the real part of ε' is equal to 0 [SL00]. With Drude model and the parameters of m_{opt}=0.18 and τ=1.1 fs, the critical density on the surface is N_{cr}=0.3602×10^{21}cm^{-3} and the critical density in the bulk is N_{cr}=4.92×10^{21} cm^{-3}. Moreover, in Fig. 4.6, the reflectivity starts to increase above the critical density on the surface. However, compared with experiment results, the critical density N_{cr} in the bulk is overestimated. This is because that the calculations only involve Drude model, not including other effects. For example, the state and band filling, as well as band-structure renormalization contribute to the decrease of critical density [SL00]. Moreover, the critical density is affect by the density- and temperature- dependent m_{opt} and τ, as

well as the imprecisions of these parameters at high electronic densities where bands are destabilized.

After the pump pulse, the dynamics of carrier and lattice are followed in the time-resolved reflectivity data in Fig. 4.4. The excited carriers in silicon cause changes in the dielectric function by carrier absorption, the screening of the ionic potential and many-body effects. At early times (t<1ps), the changes of dielectric function are mainly from electronic configuration in nature, for example, band structure change and free carrier absorption. We will discuss particular cases below:

In the case of the low pump fluence below the modification threshold, the fast drop in the reflectivity in Fig. 4.4(a) can be explained by the free carrier response at low density below critical density. The initial decrease of reflectivity at two incident angles can be estimated by Drude model, which shows the free carrier density of 3.42×10^{20} cm^{-3} at the end of the pulse duration in Fig. 4.4(a), revealing that the excited free carriers in sub-critical density contribute to the initial decease of the reflectivity.

As the pump fluence increases above the modification threshold, the drastic increase in the reflectivity occurs in Fig. 4.4(b-d), which can be explained by the free carrier response at high density above critical density. The drastic increase in the reflectivity can be also theoretically predicted by Drude model, which shows that the free carrier densities of 1.88×10^{21} cm^{-3} in Fig. 4.4(b), 2.62×10^{21} cm^{-3} in Fig. 4.4(c) and 7.89×10^{21} cm^{-3} in Fig. 4.4(d) are higher than the surface critical density. So the excited free carriers of over-critical density play a main role in the drastic increase of the reflectivity. In addition, for the highest fluence, the hydrodynamic expansion leads to the reflectivity decay.

Except the main role of free carrier response, many-body effects and the screening of the ionic potential more or less affect the reflectivity data in Fig. 4.4, which are difficult to be distinguished in our reflectivity data. Many-body effects lead to the bandgap renormalization, which decreases the bandgap, for example, the shrinkage of the bandgap is about 400 meV over the entire band at the carrier density of $10^{21}cm^{-3}$ [ACS84]. The screening of the ionic potential may cause a large change of the band structure, such as the change at L and X-valley in Fig. 4.2(a).

In addition, in high pump fluencies, destabilizing the band structure has severe structural effects. Transverse modes are softened and the matrix loses stability [GDJ04, LLS+05]. Band and structural collapse occur towards a state with liquid-like order and metallic optical properties. The semiconductor-to-metal transition may occur

in sub-picosecond timescale after the excitation, which can be directly measured by femtosecond electron [SDJ+03] and x-ray [LLS+05, CCTR11] diffraction.

4.3 Transient responses of tungsten to ultrafast laser

Tungsten is a hard brittle steel-grey metal, which has a stable crystalline form of a body-centered cubic structure. Tungsten has the highest melting point (3422 °C), lowest vapor pressure and the highest tensile strength in all pure metals. Tungsten also has the high density of 19.25 g·cm^{-3}. Typically, tungsten does not support surface plasmon polaritons (SPP) in the wavelength range of 240–920 nm. Tungsten has numerous applications in incandescent light bulb filaments, X-ray tubes, superalloys, radiation shielding, etc. [Ham04]

The frequency-dependent refractive index of tungsten is shown in Fig. 4.7. The interband transition threshold of tungsten in the ambient conditions is 0.3 eV [NKN71], which is lower than the pump photon energy of 1.55 eV in the experiment.

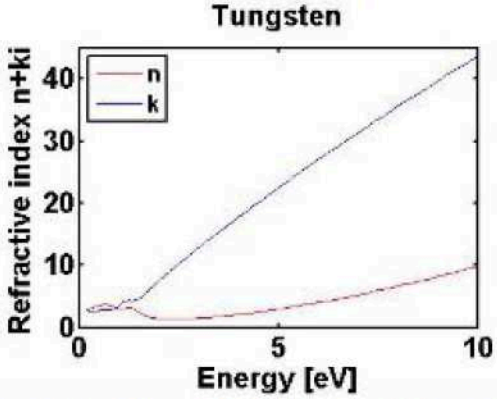

Figure 4.7: The frequency-dependent refractive index of tungsten [Ham04].

The single-side polished tungsten samples (Goodfellow Inc.) with dimensions of 25mm×25 mm ×1mm are used in the experiment. The polishing was done with either diamond paste and alumina powder with grit size down to 0.1 μm. The refractive index of the single-side polished tungsten sample is N=3.5+3.15i at 800-nm wavelength, measured by spectroscopic phase modulated ellipsometer (Uvisel, Horba Jobin Yvon). Before and after laser fabrication, the samples were cleaned ultrasonically in ethanol for 5 min.

In our experiment, the single-shot ablation threshold of tungsten sample is about 0.6 J/cm^2 (peak fluence) [BSC+10]. For the pump

fluence below the ablation threshold, the sample is immobile during the measurements and all the pump pulses are shot on a same spot on the sample in order to diminish the noise level from the surface roughness of sample. However, for the pump fluence close to or above the modification threshold, the tungsten sample is raster scanned during the measurements by a two-axis translation stage in order to ensure that each pump pulse strikes a fresh, unexcited area on the W surface.

Fig. 4.8 depicts the transient changes of reflectivity in tungsten at the incident angle of 28.7° and 65.8° following the excitation of different pump fluencies. Depending on fluence, two characteristic regions are observed. A swift reflectivity increase can be noted for low fluences up to just above the modification threshold. Just after the maximum, the reflectivity is then followed by ps scale recovery (Fig. 4.8(a, b)). This optical behavior is usually associated with variation of collisional frequencies, electronic number, or occupation degree of free-like electronic states. We will see below that the characteristic electronic bands of W with partially filled structured d blocks plays a specific role in the optical dynamics, and as well in a structural response to excitation.

After a transitional domain where the reflectivity increase seems balanced by an opposite effect, the high fluence regime (Fig. 4.8(c-f)) shows a different behavior. In this case, a sub-ps (below 0.5 ps) reflectivity decrease is followed by a stationary low-reflectivity phase of several ps. The rapid decay of reflectivity is potentially linked to a lower density state and thus to ablation, as typical ablative behaviors are associated with thermal and hydrodynamic changes on several ps timescale.

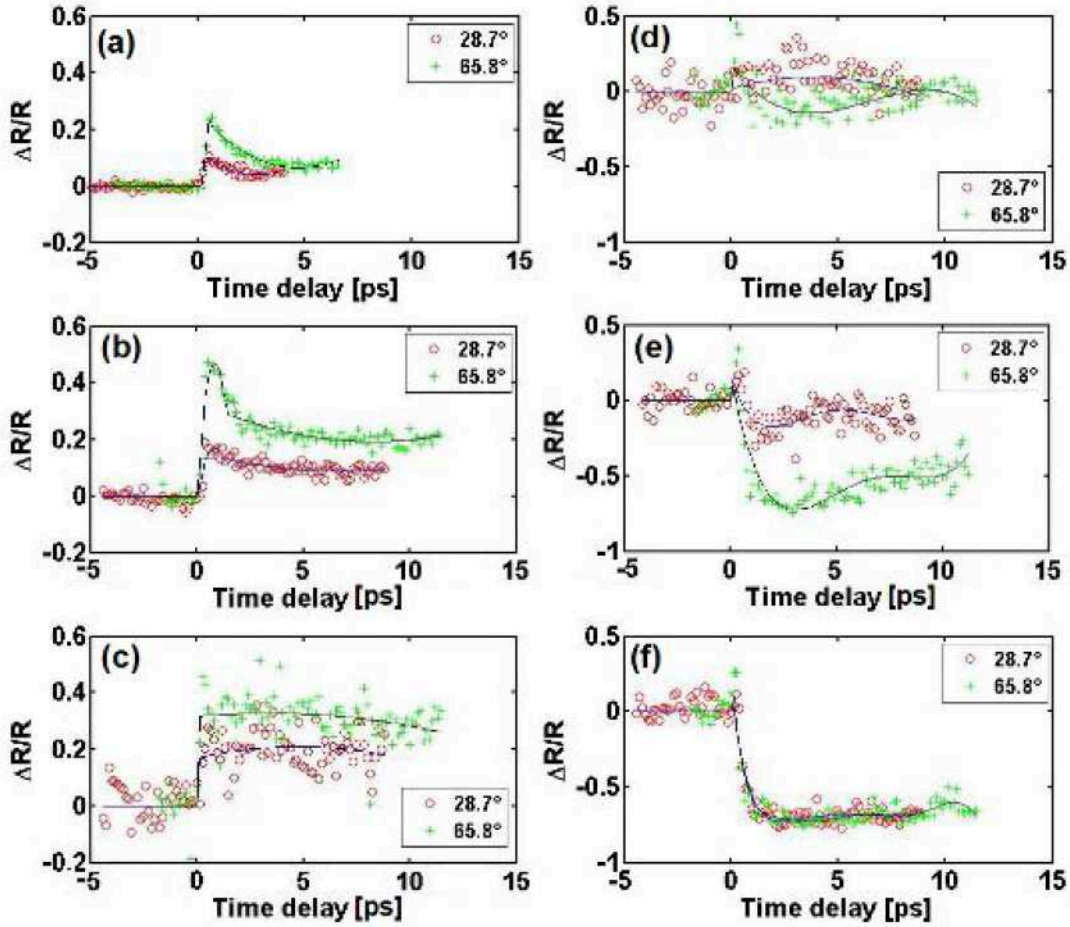

Figure 4.8: Transient changes of reflectivity in tungsten at the incident angle of 28.7° and 65.8° following the excitation at the pump fluence of (a) F=0.047 J/cm^2; (b) F=0.622 J/cm^2; (c) F=1.456 J/cm^2; (d) F=2.450 J/cm^2; (e) F=4.634 J/cm^2; (f) F=5.338 J/cm^2.

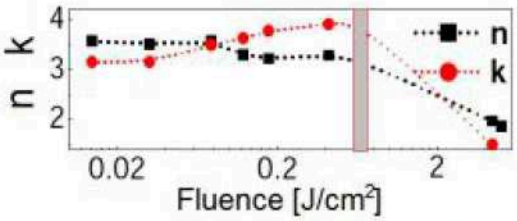

Figure 4.9: Refractive indices (n, k) as a function of pump fluence. Note that accurate values can be determined for the below and in the vicinity of ablation threshold (Gray color bar), the other values being indicative [ZLB+16].

In our research work [ZLB+16], according to parts of our experiment results, the refractive indices (n, k) retrieved from the extremum of the reflectivities at two incident angles after excitation are drawn in Fig. 4.9. Fig. 4.9 shows that the excited tungsten in low fluence below 0.1 J/cm^2 could not support the SPP propagating because of $n > k$. However, in the higher fluence in the vicinity of ablation threshold, excited tungsten satisfies the condition of n^2-k^2<-1 [VG08b], which supports SPP propagation, meaning that

the excited tungsten during the excitation follows a transition from the non-plasmon state to the plasmon state. We will see in the next chapter the potential implication in LIPSS.

To investigate the nonplasmonic-to-plasmonic transition in excited tungsten, E. Bévillon *et al.* in our research group [BCR+16] propose a possible explanation by first-principles molecular dynamics. The first-principle simulations are carried out by Abinit code [GAA+09]. A 54 atoms supercell of body centered cubic (bcc) W is built as the model with $5s^2 5p^6 5d^4 6s^2$ valence electronic configuration. At first the simulations are performed at room temperature ($T_i = T_e$ = 300 K, T_i : ion temperature, T_e: electron temperature) during 2 ps, providing an average thermodynamic equilibrium to extract the ionic configurations. Then electronic structures are computed at T_e of 300, 10^4 and 2.5×10^4 K, in order to evaluate optical properties in solid phase at these levels of electronic excitation. The simulation results are shown in Fig. 4.10 and 4.11

Fig. 4.10 shows the DOS of W model computed at T_i=300, 10^4 and 2.5×10^4 K. Dark colored areas at different T_e in DOS correspond to $[-h\nu-32kT_e, h\nu+32kT_e]$ responsible for photon-induced transitions [HDS+08], showing occupied electronic states mainly impacted by 800 nm photons. Tungsten with partially filled d-block displays an expansion and a shift toward higher energies of their d-block when T_e is increased. The changes of plasmon properties are due to Fermi broadening within a structured d-block, extending the optical intra-band transition space for visible frequencies. In other words, the presence of a d-band pseudogap reduces the optically "metallic" character of W, an effect which becomes less influential with the development of available electronic states within the d-block due to electron heating and Fermi smearing.

Fig. 4.11 shows the real part n and imaginary part k of the optical indices for the electronic temperatures of 300 K, 10^4 K and 2.5×10^4 K, showing that the n decreases and k increases with the increase of T_e, which is consistent with the experimental detection of optical indices in Fig. 4.8.

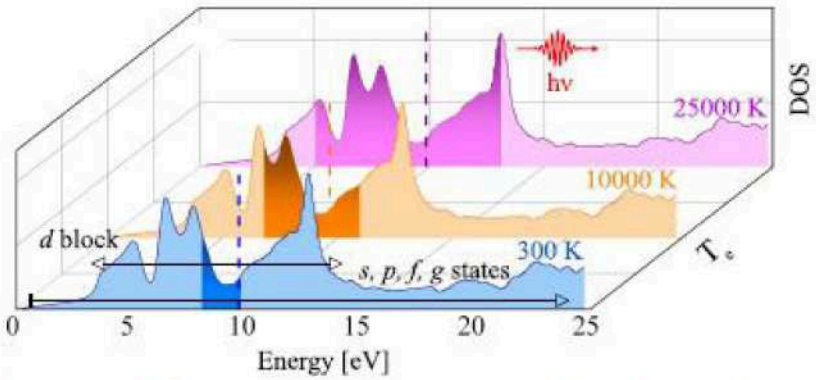

Figure 4.10: DOS of bcc W computed at Ti = 300 K and its evolution with Te. Dashed lines indicate the Fermi levels and dark colored areas show occupied electronic states mainly impacted by 800 nm photons [BCR+16].

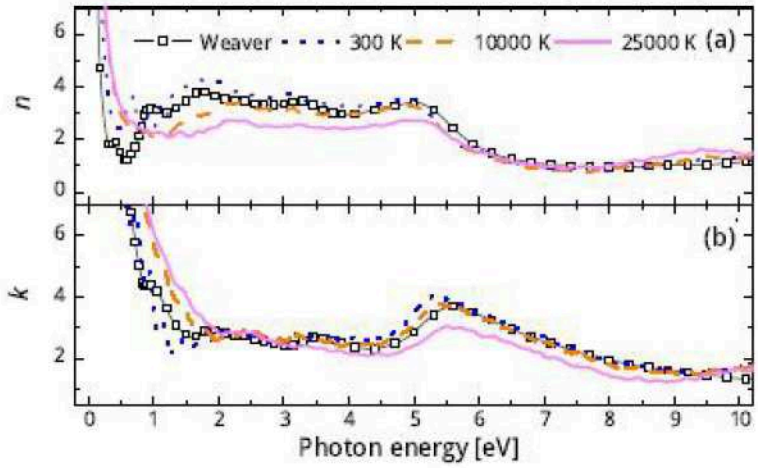

Figure 4.11: (a) Real and (b) imaginary part of the optical indices for the electronic temperatures of 300 K, 10^4 K and 2.5×10^4 K. The squares represent the experimental data for non-excited W [WOL75]. [BCR+16]

Low excitation levels determines electronic transfer around a chemical potential located within a partially filled d-band, leading to an increase of imaginary and a decrease of real indices towards a nonplasmonic-to-plasmonic state transition.

With gradual influence on molecular binding, higher input fluences determine ultrafast transitions to ionized low density phases where charge-induced, mechanical pressure-induced and thermal, heat-induced drives concur to destabilize the solid matrix on sub ps scales typically associated with non-thermal transitions.

4.4 Transient responses of BMG to ultrafast laser

Bulk metallic glasses (BMG) are solid non-crystalline metallic alloys with disordered atomic-scale structure. They are ideal material supports for micro geometries due to lack of crystallites, grain

boundaries and dislocations in material structure [WDS04]. BMG can be produced by the rapid cooling. Zr-based superalloy is a kind of bulk metallic glasses, which has been widely investigated [SNK+07]. Therefore a Zr-BMG: $Zr_{41.2}Ti_{13.8}Cu_{12.5}Ni_{10}Be_{25.5}$ (at%) alloy is used as the research object.

Because BMG has the disordered atomic-scale structures, the theory accompanying periodicity in the crystalline solid is not helpful for the analysis of BMG, However a chemical-bonding viewpoint is used instead. In order to investigate the electronic structure of disordered systems, N. F. Mott and P. W. Anderson proposed new theory of localization theory and percolation, for which they were awarded the Nobel Prize in Physics in 1977 [MJ58, And78]. However, most research works focus on the ground state of BMG, not the excited state. So the excited state of BMG is investigated by our single-pump double-probes experimental system.

The single-side polished Zr-BMG samples with the diameter of 8 mm and thickness of 3 mm are used in the experiment. $Zr_{41.2}Ti_{13.8}Cu_{12.5}Ni_{10}Be_{25.5}$ (at%) is produced by arc melting under a purified Ar atmosphere and dropping into a copper mold. After cutting, polishing was done by diamond paste and alumina powder with grit size down to 0.1 um. Zr-BMG samples before experiments were identified by electron back-scatter diffraction (EBSD). The optical indices of Zr-BMG samples are evaluated ex-situ by using a commercial ellipsometer (Uvisel, Horiba Jobin Yvon). Under 800 nm-wavelength irradiation, the refractive index of Zr-BMG is $\tilde{n}$= 3.114+3.679i.

In the experiment, the single-shot ablation threshold of Zr-BMG sample is about 0.3 J/cm^2 (peak fluence). Fig. 4.12 depicts the transient changes of reflectivity at the incident angle of 28.7° and 65.8° following the excitation of different pump fluences and the corresponding time-resolved dielectric function are retrieved by inverting Fresnel formulas. Fig. 4.12(a, b) shows the changes of reflectivity at two incident angles under pump fluence of 0.0378 J/cm^2 in the vicinity of multi-pulse pulse ablation threshold (approximately 0.04 J/cm^2), the reflectivity is remarkably stable upon excitation, so the refractive index (n, k) is considered to be constant at this pump energy. This can be seen as a consequence of the multi-metal composition which should lead to a multitude of electronic states and a quasi-continuum density of states (DOS), where the effect of laser-induced electronic population/depopulation seems minimal. A similar behavior can be noticed for fluences below the single shot ablation threshold. In between these values, multi-shot sequences affect the optical properties via the

accumulation of damage-induced topological features. Before onsetting obvious transient refractive index changes, BMG surface could be damaged by multi-pulses and nanoscale surface structures appear.

Fig. 4.12(c, d) shows the changes of reflectivity under pump fluence of 1.22 J/cm^2. Both reflectivities at two angles decreased significantly. The transient refractive index (n, k) and dielectric index extracted from these behaviors are shown in Fig. 4.12(e) and 4.12(f) respectively. Despite the fact that the inversion assumes a sharp interface, a condition that may not be fulfilled for high fluences, we note the qualitative decrease of n and k, indicating the fast appearance of a plasma phase.

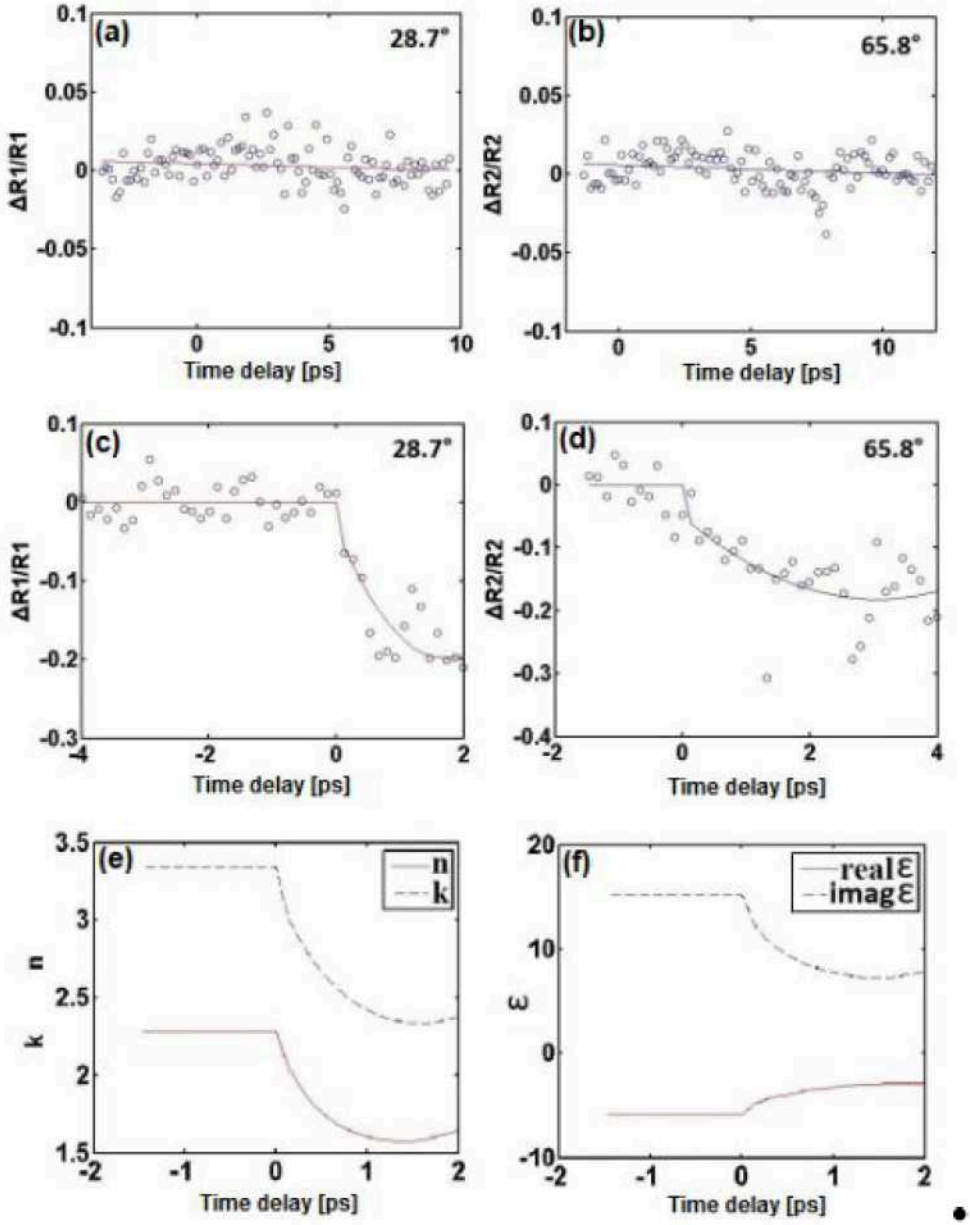

Figure 4.12: Transient changes of reflectivity in Zr-BMG at the incident angle of 28.7° and 65.8° following the excitation and the corresponding retrieved time-resolved refractive indices $\tilde{n}=n+ki$ at the pump fluence of (a, b) F= 0.038 J /cm^2; (c, d) F= 1.22J/cm^2; (e, f) Retrieved n, k behavior in the high fluence domain from (c, d). Note that the decrease signalizes a fast onset of a low density plasma phase.

In order to investigate the effect of ultrafast laser heating on the optical properties, first-principle simulations are carried out by CASTEP program [CSP+05]. Considering the limit of the computing power with CASTEP, a 50-atoms cell ($Zr_{20}Be_{12}Ti_7Cu_6Ni_5$) is used as the Zr-BMG model, shown in Fig. 4.13(a). The amorphous cell is built in a Monte Carlo fashion, by minimizing close contacts between atoms, whilst ensuring a realistic distribution of torsion angles for any given force field for any component at the solid density of 6.125g/cm^2 at the temperature of 300 K.

At first the first principle simulation is performed at room temperature (T_i = T_e = 300 K), providing the DOS and optical properties of Zr-BMG in ground state. Then Zr-BMG model is computed at the temperatures (T_i = 300 K, T_e = 10000 K), in order to evaluate the DOS and optical properties in the excited state. The simulation results are shown in Fig. 4.13(b, c).

Fig. 4.13(b) is the DOS of Zr-BMG model computed at T_i=300 K and T_e= 300 K, 10^4 K, which shows that Zr-BMG exhibits a small shift of the d-block toward lower energies (visible at the energy range of (-5~1) eV) when T_e increases, leading to the small decrease of reflectivity in excited state.

Fig. 4.13(c) shows the real part n and imaginary part k of the refractive indices computed at T_i = 300 K and T_e= 300 K, 10^4 K. At the 1.55-eV probe energy, with the increase of T_e from 300 K to 10^4 K, n increases and k decreases slightly. The minor changes of optical indices also reflect the stable reflectivity upon weak excitation in Fig. 4.12(a, b).

With the increase of pump energy, the reflectivity decreases (Fig. 4.12(c d)). These can be explained by the onset of low density plasma absorbing the probe pulses.

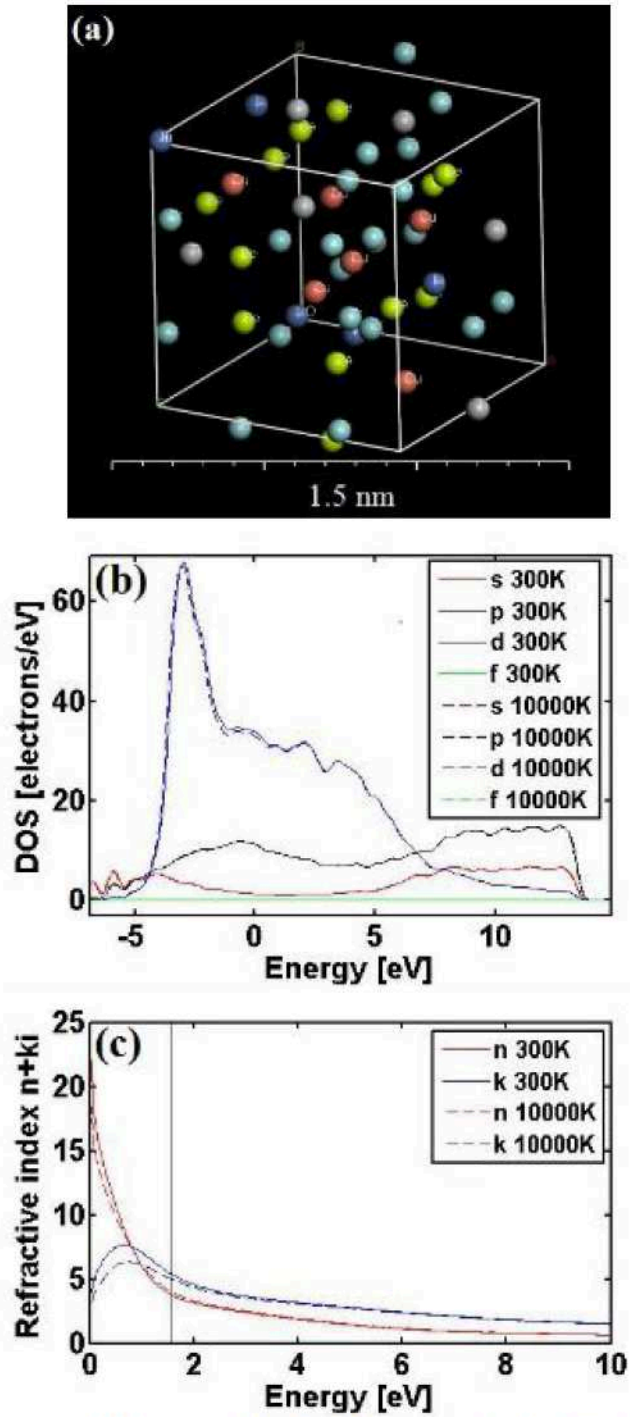

Figure 4.13: (a) Zr-BMG model of 50 atoms; (b) DOS of Zr-BMG model computed at T_i = 300 K and T_e= 300 K, 10^4 K. The electronic chemical potential (Fermi level) is at 0 eV. (c) Real and imaginary part of the refractive indices computed at T_i = 300 K and T_e= 300 K, 10^4 K.

4.5 Conclusion

In this chapter, we have observed the transient optical properties of silicon, tungsten and Zr-BMG excited by ultrafast laser

pulses. A single-color two-angle time-resolved ellipsometry method was presented.

For semiconductor silicon, in the case of the low pump fluence below the modification threshold, the fast drop of the reflectivity can be explained by the free carrier response at low density below critical density. As the pump fluence increases above the modification threshold, the drastic increase of the reflectivity occurs, due to the free carrier response at high density above critical density, many-body effects, as well as the screening of the ionic potential. The transition from the semiconductor to the metal-like liquid phase occurs in ultrafast laser ablation at high energy.

For metal tungsten, at low pump fluence, the initial fast increase of the reflectivity in about 0.5 ps can be explained by a redistribution of electron population around the chemical potential within a d-block pseudogap. With the increase of pump fluence, the reflectivity shows a sudden decrease signaling a fast achievement of the plasma state. Particularly, the excitation achieved the transition from the non-plasmon state to the plasmon state, a feature that will be verified in LIPSS calculations. Experimental plasmon transition is investigated by first-principle molecular dynamics based on Abinit code. The plasmon transition is due to Fermi broadening within a structured d-block, extending the optical intra-band transition space for visible frequencies.

For amorphous alloy Zr-BMG, at low pump fluence the reflectivity is remarkably stable upon excitation. As the fluence of the pump pulse increases above the threshold the reflectivity at the two angles decreases. In order to investigate the effect of ultrafast laser heating on the optical properties, first-principle simulations are carried out by CASTEP program. The calculated DOS and optical properties of Zr-BMG in both ground state and excited state show that Zr-BMG exhibits a small shift of the d-block toward lower energies at the energies of in the (-5~1) eV range when T_e increases, leading to the small decrease of reflectivity in excited state. The minor changes of optical indices also reflect the stable reflectivity upon weak excitation.

These experimental results offer the information for the next investigation of ultrafast laser ablation and fs-LIPSS formation.

Chapter 5

LIPSS experiments on selected materials

We review here a range of ripple-like structures obtained on materials ranging from amorphous to crystalline materials with various bandgaps. We have specifically chosen tungsten, a metallic material with non-plasmonic characteristics in the NIR-VIS range, multi-component metallic alloys with different degrees of surface finish, as well as semiconductor and dielectric materials (silicon, fused silica) where collective carrier response is induced by electronic excitation. We will focus therefore on the influence of material, surface and excitation effects in defining LIPSS.

We have seen that laser-induced periodic surface structure (LIPSS) is a universal phenomenon occurring on almost all solids. The typical femtosecond (fs) laser-induced ripples have typically a smaller spatial period than laser wavelength and various orientations. We have equally indicated the potential application in micro/nano-machining. In this chapter, we focus on several typical materials to investigate the general mechanism of fs-LIPSS formation. At first, the effects of the materials with different electronic energy band structures are investigated, involving W (metal), Si (semiconductor) and SiO_2 (dielectric). Secondly, we focus on the LIPSS formation on W in view of its pristine non-plasmonic condition. Finally, the effect of ionic multi-element structures is discussed in the single-crystal superalloy CMSX-4, amorphous alloy Zr-BMG and its corresponding crystal alloy Zr-CA. The range of experiments presented here underline that the feedback process between incident laser and surface nanostructures plays an important role in the ripple formation. Therefore surface roughness and defects will affect the LIPSS orientation and arrangement

quality and we have designed experiments to outline topography and electronic effects, namely the surface roughness, the dynamics of the dielectric function, the material composition and its structural state. We give examples of LIPSS formation on metals, semiconductors and dielectrics, underlining factors that can assist the formulation of general scenarios for LIPSS formation. We couple morphology observations (electron microscopy (SEM), atomic force microscopy (AFM)), chemical and structural analysis (in specific cases the chemical compositional changes of LIPSS are measured by energy dispersive X-ray spectrometry (EDX) and the structural state via electron back-scatter diffraction (EBSD).) together with controlled state transformation of the materials (crystalline versus amorphous). Finally, LIPSS characteristics of six materials dependent on different pulses and laser fluencies are respectively analyzed and summarized, providing the experimental results for the investigation of the LIPSS formation mechanism from an electromagnetic viewpoint.

5.1 LIPSS experimental setup

All LIPSS experiments are performed by using as radiation source a regenerative Ti:sapphire oscillator-amplifier system (Legend Coherent Inc) based on the chirped-pulsed amplification technique at a central wavelength of 800 nm with pulse duration of 50 fs and repetition rate of 1 kHz. The linearly polarized Gaussian laser beam is focused with a convex lens of 100-mm focal length down to a spot of radius=13 μm at $1/e^2$ intensity. The laser fluence is adjusted by using the combination of a waveplate and a polarizer. The number of pulses is controlled by laser shutter. Increasing laser pulse numbers are used to investigate the initial LIPSS formation. The sample is mounted on a computer-controlled XYZ translation stage with a spatial resolution of 125 nm and the irradiated zone is observed in real time by a magnifying imaging system and projected on a CCD monitor. All the experiments are performed in ambient atmosphere with the sample surface perpendicular to laser beam. The experimental details and results of LIPSS on tungsten, silicon, fused silica, CMSX-4, Zr-BMG and Zr-CA are respectively introduced in the following.

5.1.1 LIPSS experiments on tungsten

The single-side polished tungsten sample (Goodfellow Inc) with the size of 25 mm×25 mm×1 mm is used in the experiment.

The polishing was done with diamond paste and alumina powder with grit size down to 0.1 μm. Before and after laser fabrication, the samples are cleaned ultrasonically in ethanol for 5 min.

In order to investigate LIPSS formation, increasing numbers laser pulses are shot at the laser fluence of F=0.38 J·cm^{-2} (in the vicinity of the single-shot ablation threshold of F=0.4 J·cm^{-2}) at different spots on the tungsten sample. The morphology of LIPSS was observed by SEM and the periodicity of ripples is analyzed by two-dimensional Fast Fourier Transform (2D-FFT).

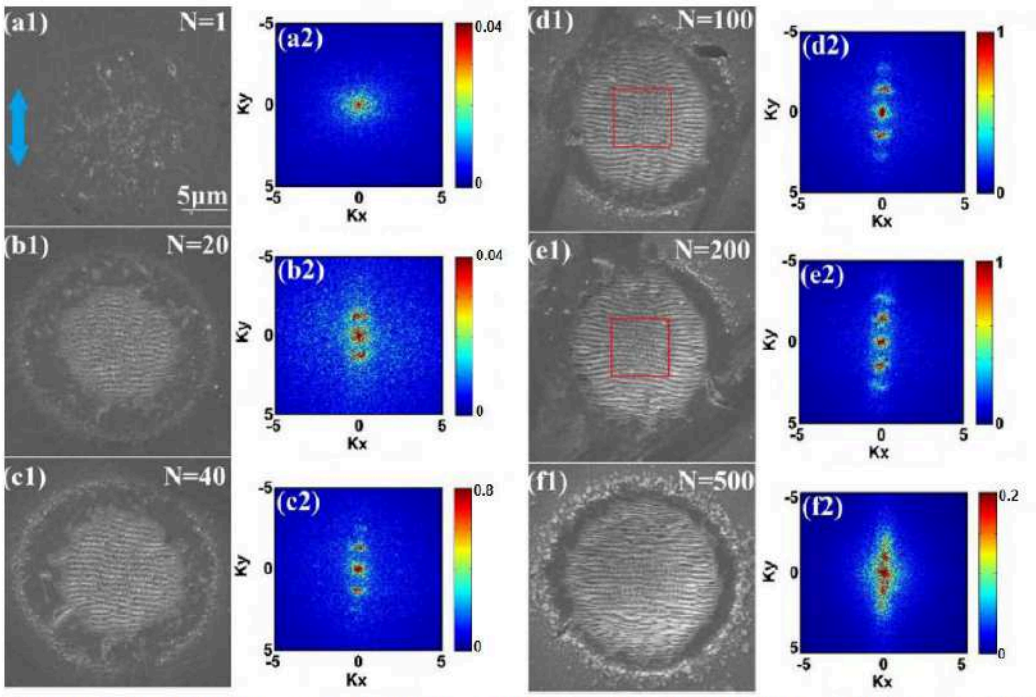

Figure 5.1: SEM images of tungsten surfaces after irradiation at fluence F=0.38 Jcm^{-2} by fs laser pulses: (a1) N=1; (b1) N=20; (c1) N=40; (d1) N=100; (e1) N=200; (f1) N=500; (a2-f2) shows the 2D-FFT of (a1-f1) images respectively, representing the periodicity in the spatial frequency space. The laser polarization direction indicated with a double-head arrow and scale are shown in (a).

Fig. 5.1 shows the SEM images of LIPSS formed on tungsten surface with increasing pulse number (N) of linearly polarized laser radiation at a fixed fluence F=0.38 Jcm^{-2}. Fig. 5.1(a1) represents the morphology of the irradiated tungsten surface after 1 pulse, showing that isolated nanostructures are formed in a disordered distribution, leading to the enhancement of surface roughness. These were previously discussed and localized nucleation centers of phase transitions [ARL^{+}15]. Fig. 5.1(a2) is the 2D-FFT of Fig. 5.1(a1), representing the periodicity in the frequency space, which shows that the surface nanostructures have the Gaussian distribution of spatial frequency, without an obvious periodicity. Note that the amplitude of color bar represents the intensity of distributed spatial frequency

in Fig. 5.1(b1); In Fig. 5.1(b1), after 20 pulses, LSFL ripples with direction perpendicular to laser polarization are observed within the irradiated spot. Fig. 5.1(b2) is the 2D-FFT of Fig. 5.1(b1), showing that LSFL ripples have the spatial periodicity of 625±16nm; In Fig. 5.1(c1), after 40 pulses, LSFL ripples become much clearer, while faint HSFL ripples appear with the direction perpendicular to laser polarization. Fig. 5.1(c2) is the 2D-FFT of Fig. 5.1(c1), showing that LSFL ripples have the spatial periodicity of 597±15 nm and HSFL ripples have the spatial periodicity of 320±5 nm; Fig. 5.1(d1, d2) show that after 100 pulses, LSFL ripples in the full spot have the spatial periodicity of 581±15 nm. Typically, in the red rectangle region in Fig. 5.1(d1), LSFL ripples have the spatial periodicity of 568±15 nm and HSFL ripples have the spatial periodicity of 303±10nm. However, in the region outside the red rectangle in Fig. 5.1(d1), LSFL ripples have the spatial periodicity of 625±15 nm; Fig. 5.1(e1, e2) show that after 200 pulses, LSFL ripples in the full spot have the spatial periodicity of 568±15 nm. Typically, in the red rectangle region in Fig. 5.1(e1), LSFL ripples have the spatial periodicity of 520±15 nm and HSFL ripples have the spatial periodicity of 285±10 nm. However, in the region outside the red rectangle in Fig. 5.1(e1), LSFL ripples have the spatial periodicity of 568±15 nm; Fig. 5.1(f1, f2) show that after 500 pulses, the spatial periodicity of LIPSS becomes unclear and the amplitude of color bar in Fig. 5.1(f2) decreases, revealing that the formed LIPSS have been damaged by subsequent pulses. This behavior is not actually new but it will be useful for the follow-up discussion.

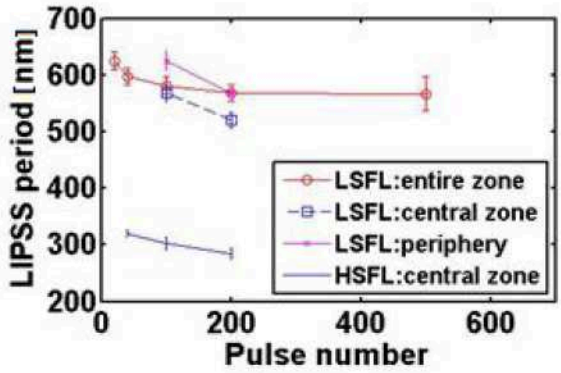

Figure 5.2: The relationship between LIPSS spatial periods and pulse number.

The relationship between LIPSS spatial periodicity from Fig. 5.1 and pulse number is summarized and drawn in Fig. 5.2. Fig. 5.2 shows that the LSFL periodicity decreases with the increase of laser pulses, which is consistent with the reference [VG08b] and the similar phenomenon in other materials [HZC+09]. In addition, at 100-200 pulses, the LSFL periodicity in the center region is bigger

than the peripheral region of the irradiated spot. On the other hand, HSFL periodicity decreases a little with the increase of laser pulses, which is nearly the half of LSFL periodicity formed at the same pulses.

In Sipe theory, LIPSS are commonly attributed to the interference between the incident laser light and the excited surface electromagnetic wave. Particularly, LIPSS on metals are believed to be generated by the interference between the incident light and excited surface plasmons (SPP) (provided that the latter can be indeed excited in synchronism–momentum-conservation-conditions). For a smooth planar dielectric/metal interface, SPP wave vector parallel to the interface K_{SPP} is given by [Rae88]:

$$K_{SPP} = K\sqrt{\frac{\varepsilon_m \varepsilon_d}{\varepsilon_m + \varepsilon_d}} \qquad (5\text{-}1)$$

Here K is the light wave vector in vacuum, $\varepsilon_m=\varepsilon'_m+i\varepsilon''_m$ is the dielectric constant of the metal, and $\varepsilon_d=\varepsilon'_d+i\varepsilon''_d$ is the dielectric constant of the dielectric medium, $\varepsilon_d=1$ when the medium is vacuum or air. The conditions for SPP propagating on the metal planar surface in air is $Re(\varepsilon'_m)<-1$ [Rae88]. Then due to SPP, the spatial periodicity Λ of LSFL ripples formed on metal surface in the air by a linearly polarized laser light is given [VG08b]:

$$\Lambda = \lambda \times \mathrm{Re}\left(\sqrt{\frac{\varepsilon_m + 1}{\varepsilon_m}}\right) \qquad (5\text{-}2)$$

Here λ is the incident laser wavelength, λ=800 nm in the experiments.

In the experiment, the dielectric constant of unexcited tungsten is ε_m=2.33+22.05i at 800-nm wavelength. This optical state could not support SPP propagating on the planar surface because of the positive real part of dielectric constant.

Considering the experiments of transient optical indices in the excited W in Chapter 4.3, the ultrafast laser excitation can bring the real part of dielectric constant below -1, which satisfies for a short moment the condition for SPP (we recall that this is achieved at peak electronic temperatures, almost during the pulse duration). For example, according to the experiment data in Chapter 4.3, the dielectric constant of excited W can be -4.18+15.75i at the end of the laser pulse duration at the energy close to the ablation threshold. According to the equation (5-2), the calculated spatial period on the excited W is Λ=794 nm, which is much bigger than the experimental LSFL periodicity of 625 - 568 nm. So the SPP seems to contribute a little for LSFL formation on the planar W.

In general, the periodicity of LSFL ripples decreases as the number of laser pulses increases [HZC+09, BMS05, HCT+07]. The initial SPP-laser interference and the subsequent grating-assisted SPP-laser coupling were used to explain the periodicity-decreasing phenomenon [HZC+09]. These indicate the smaller periodicity in the periphery area than the center area of the irradiated spot [HZC+09], which is not consistent with our experiment results of the smaller periodicity in the center region (Fig. 5.2). In addition, J. Z. P. Skolski *et al*'s investigation by FDTD simulations showed that the propagation of SPPs is not a necessary condition for LSFL formation [SRO+14]. So it is a question if the SPP contribute to the LSFL formation on tungsten.

At this point we postulate that, except the transient optical indices during the excitation, the nanostructures on W surface also play a role in the LIPSS formation, which will be discussed in the next Chapter.

5.1.2 LIPSS experiments on the semiconductor (Si)

The polished (100) surface of n-doped single crystal silicon samples (ITME product) are used in experiment. In order to investigate LIPSS formation on silicon, increasing numbers of laser pulses are shot at the laser fluence of F=0.30 J·cm^{-2} (slightly above the modification threshold) at different spots on the silicon sample. The morphology of LIPSS was observed by SEM and the periodicity of ripples is analyzed by two-dimensional Fast Fourier Transform (2D-FFT).

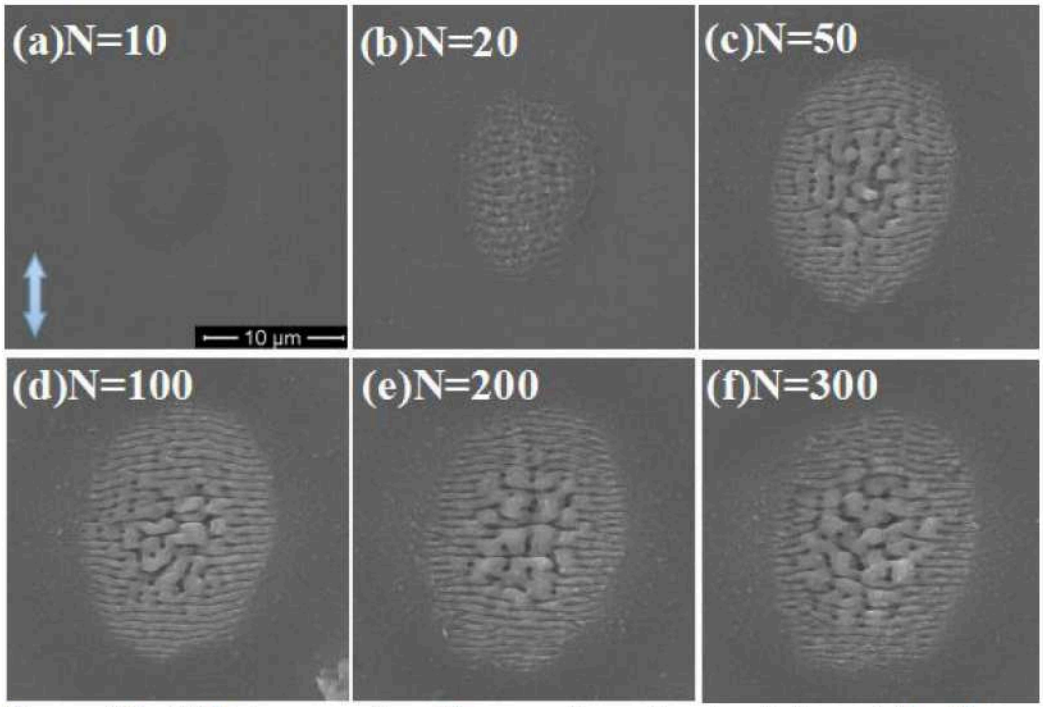

Figure 5.3: SEM images of a silicon surface after irradiation at the fluence F=0.30 Jcm^{-2} by different numbers of fs laser pulses: (a) N=10; (b) N=20; (c) N=50; (d) N=100; (e) N=200; (f) N=500. The laser polarization direction indicated with a double-head arrow and scale are shown in (a).

Fig. 5.3 shows the SEM images of LIPSS formed on silicon surface with increasing pulse number (N) of linearly polarized laser radiation at a fixed fluence F=0.30 Jcm^{-2}. Fig. 5.3(a) represents the morphology of the irradiated silicon surface after 1 pulse, showing a dark coloration spot in the center without LIPSS. In Fig. 5.3(b), after 20 pulses, LSFL ripples with direction perpendicular to laser polarization are observed within the irradiated spot, which have the quasi-constant spatial periodicity centered at 744 nm by 2D-FFT; In Fig. 5.3(c), after 50 pulses, LSFL ripples become much clearer, while faint macro-ripples appear in the center of irradiated spot with the direction parallel to laser polarization, showing that LSFL ripples have the quasi-constant spatial periodicity centered at 646 nm and macro-ripples have the quasi-constant spatial periodicity centered at 1534 nm; Fig. 5.3(d) shows that after 100 pulses, LSFL ripples in the full spot have the quasi-constant spatial periodicity centered at 663 nm. However, macro-ripples are not seen clearly; Fig. 5.3(e) shows that after 200 pulses, instead of macro-ripples, micro-scale pillars appear in the center of the irradiated spot, LSFL ripples in the peripheral have the quasi-constant spatial periodicity centered at 663 nm; Fig. 5.3(f) show that after 300 pulses, micro-scale pillars also appear in the center of the irradiated spot, LSFL ripples in the

peripheral have the quasi-constant spatial periodicity centered at 614 nm.

Next, we analyze these experimental results from a perspective given by Sipe theory and Drude model. According to the formula (4-4) of laser-induced free carrier density, the calculated free carrier density is N_e=2.362×10^{21} cm^{-3} from F=0.30 J/cm^2 in the experiment. Then the dielectric constant of excited silicon at this density can be derived as ε^*= 7.10+2.57i ($\tilde{n}$= 2.71+0.47i), from the Drude model in formula (4-2) and (4-3).

Then Sipe model is used to predict the LIPSS formation on silicon. In Sipe model, the maximum values in the efficacy factor η map correspond to the LIPSS with the orientation and periods. The Sipe model underlines the effect of rough surface, and the shape factor s and filling factor F are set to be (F, s) = (0.1, 0.4) for the rough surface [SYP$^+$83, BRK09]. Fig. 5.4 are the two-dimensional η maps for normal incident radiation (θ=0°) at λ=800 nm for unexcited silicon (ñ=3.6959+0.0047i) and excited silicon (ñ=2.4751+0.0013i). The laser polarization is parallel to the Y axis. In Fig. 5.4, the feature indicated by a single-headed arrow can be associated with LSFLs being predominantly perpendicular to the polarization and having periods close to the laser wavelength. On the unexcited silicon, the LSFLs have the spatial period of Λ=800/1.04=769.2 nm. Considering the transient optical indices due to laser-induced free carriers in the experiment (Fig. 5.3), the LSFLs on the excited silicon are predicted to have the spatial period of Λ=800/1.08=740.7 nm, which is consistent with the experiment results in Fig. 5.3. So both the effects of rough surface (surface nanostructures) and the intra-pulse transient optical indices can contribute to the LSFL formation.

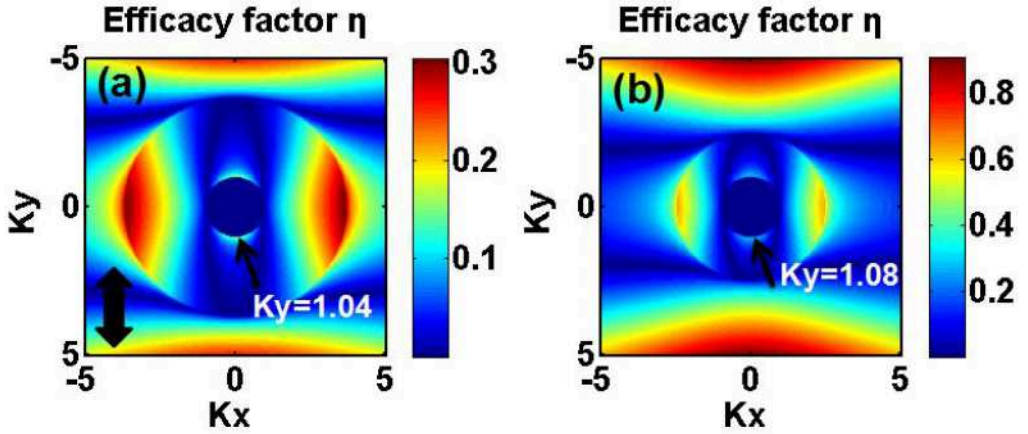

Figure 5.4: 2D maps of the efficacy factor η for single-crystalline silicon as a function of the normalized LIPSS wave vector Kx, Ky, for normal incident radiation (θ=0°) at λ=800 nm for: (a) unexcited silicon (ñ=3.6959+0.0047i); (b)

excited silicon (ñ=2.4751+0.0013i). The polarization E is indicated in a double-heated arrow in (a).

5.1.3 LIPSS experiments on the dielectric fused silica

Amorphous fused silica (a-SiO_2) is the pure form of the silica glass; when molten silicon dioxide is rapidly cooled, it solidifies as a glass. Pure fused silica has the glass transition temperature of 1202 ◦C and the softening temperature of 1585 ◦C [Ojo04]. Dielectric fused silica is a largely used optical material due to its good transmission in a wide spectral range (from 180 nm in the ultraviolet region to 2.5 μm in the infrared region), and low coefficient of thermal expansion. Fused silica has high stability to thermal shock over large temperature excursions and high laser damage threshold. Besides its optical properties, fused silica is also a key material in microelectronics and chromatography due to its mechanical resistance, high dielectric strength, wide temperature operating range and selectivity for chemical modification [Mis12].

In order to investigate LIPSS formation on fused silica, increasing numbers of laser pulses are shot at the laser fluences of F=3.23-3.8 $J{\cdot}cm^{-2}$ at different spots on the fused silica sample. The morphology of LIPSS is observed by SEM and the periodicity of ripples is analyzed by 2D-FFT.

Fig. 5.5 shows the SEM images of LIPSS formed on fused silica with increasing pulse number (N) of linearly polarized laser radiation at a fixed fluence F=3.23 Jcm^{-2}. In Fig. 5.5(a), after 8 pulses, HSFL ripples with direction perpendicular to laser polarization are observed within the irradiated spot, which have the quasi-constant spatial periodicity centered at 239 nm with large range by 2D-FFT; In Fig. 5.5(b), after 10 pulses, HSFL ripples have the quasi-constant spatial periodicity centered at 274 nm with large range by 2D-FFT; In Fig. 5.5(c), after 20 pulses, remarkably, new surface structures appear in the center of irradiated spot. However, HSFL only exist in the periphery of the spot; Fig. 5.5(d) shows that after 50 pulses, LSFL ripples in the full spot have the quasi-constant spatial periodicity centered at 575 nm with the direction parallel to laser polarization.

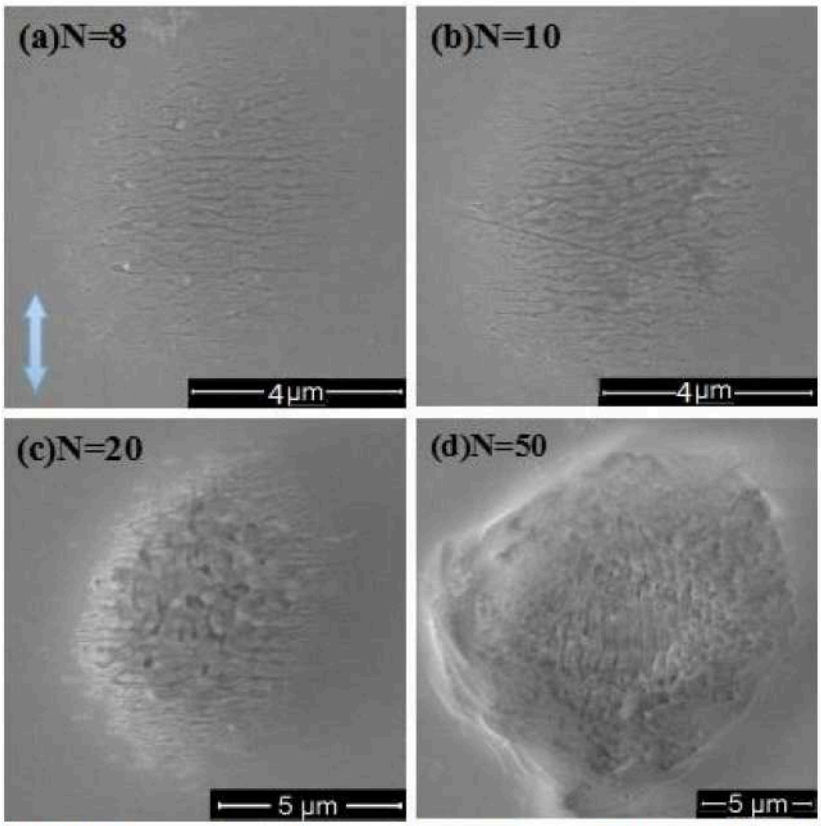

Figure 5.5: SEM images of silicon surface after irradiation at fluence F=3.23 J•cm^{-2} by fs laser pulses: (a) N=8; (b) N=10; (c) N=20; (d) N=50. The laser polarization direction is indicated in (a) with a double-head arrow. Note that different scales in each image.

Fig. 5.6 shows the SEM images of LIPSS formed on fused silica with increasing pulse number (N) of linearly polarized laser radiation at a fixed fluence F=3.80 J·cm^{-2}. In Fig. 5.6(a), after 4 pulses, LSFL ripples with direction parallel to laser polarization are observed within the irradiated spot. LSFL ripples have the quasi-constant spatial periodicity centered at 681 nm by 2D-FFT; In Fig. 5.6(b), after 6 pulses, LSFL ripples with direction parallel to laser polarization are observed within the irradiated spot, having the quasi-constant spatial periodicity centered at 614 nm (given by 2D-FFT); In Fig. 5.6(c), after 10 pulses, LSFL ripples with direction parallel to laser polarization are observed within the irradiated spot, with the quasi-constant spatial periodicity centered at 646 nm by 2D-FFT; Fig. 5.6(d) shows that after 20 pulses, LSFL ripples in the full spot have the quasi-constant spatial periodicity centered at 557 nm with the direction parallel to laser polarization.

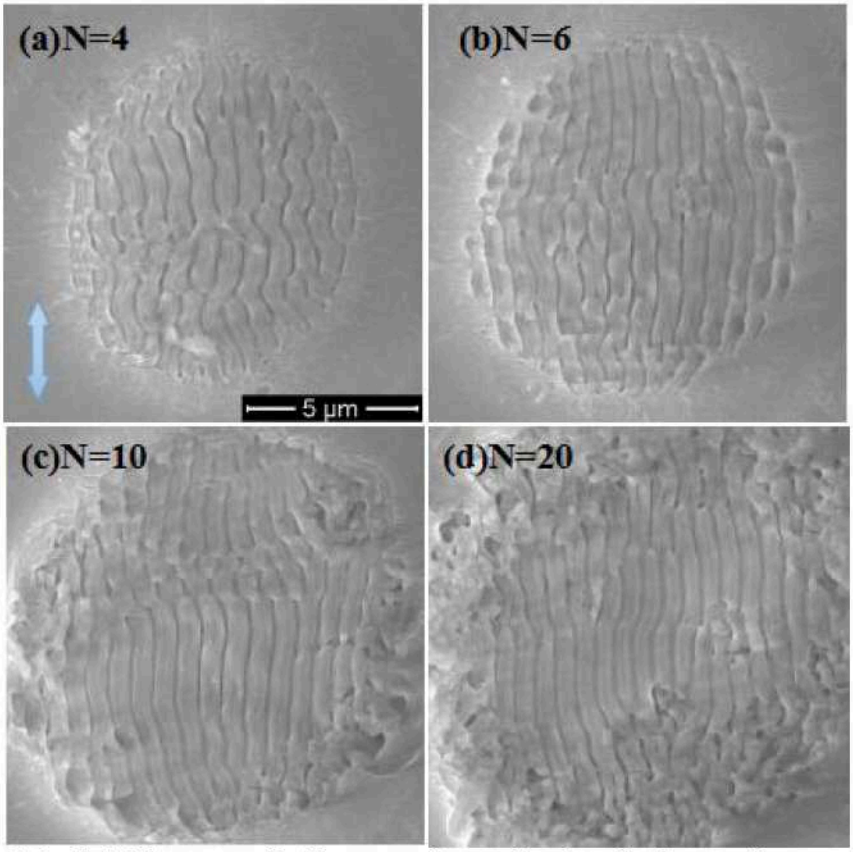

Figure 5.6: SEM images of silicon surface after irradiation at fluence F=3.80 J·cm^{-2} by fs laser pulses: (a) N=4; (b) N=6; (c) N=10; (d) N=20. The laser polarization direction indicated with a double-head arrow and scale are shown in (a).

In summary, there are two types of LIPSS on fused silica, involving HSFL ripples perpendicular to laser polarization (direction is marked as $\perp$E), LSFL ripples parallel to laser polarization (direction is marked as $\parallel$E). With the increase of laser pulses, the LSFL periodicity gradually decreases, going in the range of 681 - 558 nm, similar to the case of LSFL on tungsten and silicon. Remarkably, at the fluence of F=3.23 Jcm^{-2}, with the increase in the number of laser pulses, the transition from HSFL ripples ($\perp$E) to LSFL ($\parallel$E) is observed. However, at higher fluence of F=3.80 J•cm^{-2}, only LSFL ($\parallel$E) ripples are observed.

Compared with semiconductors, the dielectric materials have larger bandgap. For fused silica, the bandgap is equal to E_g=9 eV [Mis12]. Since the photon energy (1.55 eV) in the experiments is much smaller than the band gap, no linear absorption takes place, leading to transparency for the 800-nm light at low intensities. In Sipe model, LIPSS formations on metals and semiconductors are commonly attributed to the interference between the incident laser light and the excited surface electromagnetic wave. Compared with a situation where reflection dominates (most light photons are

reflected on metal and semiconductor surfaces), a large part of the incoming light can refract into the bulk dielectric materials and bulk and surface effect will mix. So the interference between refracted light in the vicinity of the surface layer and excited surface electromagnetic wave plays an important role in LIPSS formations on dielectric materials. The complexity can go beyond the Sipe theory and lead to different LIPSS characteristics. For example, LSFL ($\parallel$E) on fused silica are different from the LSFL ($\perp$E) on tungsten and silicon in our experiments. The scattering characteristics and the effects of dielectric function in fused silica on LSFL formation will be investigated in next Chapter by FDTD simulations.

In addition, focused femtosecond pulses allow laser intensities to be sufficiently high for triggering processes of nonlinear optical absorption (photo-ionization), leading to the generation of free electrons in the conduction band. Various nonlinear effects resulting from the strong laser fields in the dielectric material and the additional free electrons appearing in the focal region affect the energy deposition on surface. For example, we observed the transition from HSFL($\perp$E) in low fluence to LSFL ($\parallel$E) in high fluence on the fused silica, related to the effect of free carrier density.

Finally, the LIPSS on dielectric materials are so different from the LIPSS on metals and semiconductors, because of the transparent properties due to the dielectric functions. These will be discussed in the next chapter.

5.1.4 LIPSS experiments on the single-crystal superalloy CMSX-4

CMSX-4 is an ultra-high strength, single crystal nickel-base alloy with a composition given as 62.17 Ni, 12.58 Al, 9.86 Co, 7.45 Cr, 2.17 Ta, 2.11 W, 1.29 Ti, 0.94 Re, 0.38 Mo and 1.05 other elements in atomic percent. CMSX-4 has the melting point of 1455°C, and boiling point of 2730°C. CMSX-4 has the solid density of 8.90 g/cm^3. The alloy can be operated at high peak temperature of at least 1163°C. Nickel-based superalloys are widely used for turbine blades in aircraft engine and power generation systems [RGN07]. Therefore CMSX-4 can serve as good model metallic systems for ablation mechanism studies in particular thermodynamic conditions of high melting point. In addition, they are two-phase materials containing no high-angle boundaries.

Fig. 5.7 is the SEM images of the typical two-phase (γ (Ni) and γ'(Ni_3Al)) microstructure of the CMSX-4 after solution and aging treatment, showing that cubic ordered γ'(Ni_3Al) precipitates with an edge length of 0.6 μm are embedded in the γ (Ni) matrix with a channel width of approximately 90 nm [MMT+07]. After fs laser ablation, such two-phase matrix structures could induce surface nanostructures, enhancing the nanoscaled surface roughness and promoting the LIPSS formation.

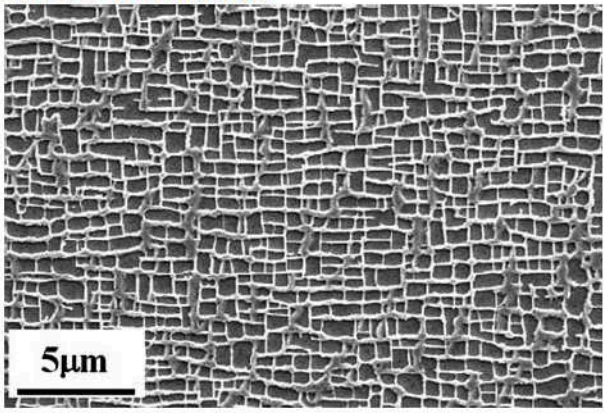

Figure 5.7: SEM images of the two-phase microstructure of the single-crystal superalloy CMSX-4 [MMT+07].

Ultrashort pulsed laser ablation in nickel-base superalloy CMSX-4 has been investigated so far in different aspects. These are targeting processing thresholds (single-shot ablation thresholds in CMSX-4 as 0.3±0.03 J/cm^2 [MMT+07]) including the conditions for generating liquid layers, or ablating processes including the developments of shock wave. Zhang *et al.*'s investigations [ZCF+11, ZCF+12] showed that, similar to a range of metallic systems, fs laser ablation produces low-spatial-frequency LIPSS (LSFL), high spatial-frequency LIPSS (HSFL) and spikes on CMSX-4. Spatial periodicities are reported as 730-760 nm for LSFL, 360 nm for HSFL with both directions perpendicular to laser polarization. We will follow below the role of local surface topography in forming LIPSS.

The surface of the Ni-based superalloy CMSX-4 sample was polished by conventional metallographic procedures with a final polish of 0.05 μm Al_2O_3 suspensions. The sample was subsequently cleaned in an ultrasonic ethanol bath for 5~10 min prior to the femtosecond laser ablation. The refractive index of CMSX-4 was measured by a spectroscopic phase modulated ellipsometer (Uvisel, Horiba Jobin Yvon) as ñ=2.05+4.24i at 800 nm wavelength.

We first determine the influence of the dose accumulation in a cumulative regime and we observe the topology evolution. In order to investigate LIPSS formation, an increasing number of laser pulses

are shot at different spots on the CMSX-4 sample. The morphology of the laser-induced periodic microstructure was examined aposteriori by SEM and the periodicity of ripples is analyzed by two-dimensional Fast Fourier Transform (2D-FFT).

Fig. 5.8 shows the SEM images of LIPSS formed on CMSX-4 surface with increasing pulse number (N) of linearly polarized laser radiation at a fixed fluence F=0.507 J•cm^{-2}. For N=1, we observe several nano-protuberances and nanoholes on surface in the center of the irradiated spot [Fig. 5.8(a)]. For N=4, well-marked HSFL ripples with direction parallel to laser polarization are generated and, at the same time, faint LSFL ripples with direction perpendicular to laser polarization are observed within the irradiated spot. Above N=10, well defined LSFL ripples are observed (Fig. 5.8(c, d, e)). This evolution is confirmed by a 2D-FFT analysis of the patterns (Fig. 5.8 (f-j)), equivalent to a description in the space frequency domain. If Fig. 5.8(f) does not allow to define a periodic pattern for N=1 but merely a randomly rough topology, HSFL are imprinted for a low number of pulses (Fig. 5.8(g)). Fig. 5.8(g), the 2D-FFT profile of Fig. 5.8(b) at N=4 confirms HSFL ripples with a quasiconstant periodicity centered at 337 nm and LSFL ripples with a quasiconstant periodicity centered at 725 nm. For N=10, HSFL ripples and clear LSFL ripples are observed. Remarkably, because of a defect line marked in red line in Fig. 5.8(c), the direction of a few LSFL ripples near the defect is changed [Fig. 5.8(c)]. Fig. 5.8(h) is 2D-FFT of Fig. 5.8(c) that shows HSFL ripples with a quasiconstant periodicity centered at 349 nm and LSFL ripples with a periodicity value centered at 665 nm. For N=20, HSFL ripples with direction parallel to laser polarization disappear [Fig. 5.8(d)]. Fig. 5.8(i), the 2D-FFT of Fig. 5.8(d), shows LSFL ripples with a quasiconstant periodicity centered at 672 nm. A new kind of HSFL ripples with direction perpendicular to laser polarization starts to appear having a quasiconstant periodicity centered at 343 nm, which has been reported in references [ZCF$^+$11, ZCF$^+$12]. For N=50, both LSFL and HSFL ripples with direction perpendicular to laser polarization are observed [Fig. 5.8(e)]. Fig. 5.8(j) is 2D-FFT of Fig. 5.8(e) that shows LSFL ripples with a quasiconstant periodicity centered at 656 nm and HSFL ripples with the periodicity centered at 328 nm. It is noted that the periodicity of LSFL ripples decreases with increasing number of laser pulses.

In summary, the morphology of LIPSS on CMSX-4 shows three kinds of LIPSS: LSFL perpendicular to laser polarization, HSFL parallel to laser polarization and HSFL perpendicular to laser polarization. LSFL perpendicular to laser polarization has the

periodicity of 725-629 nm and the periodicity decreases gradually with an increasing number of laser pulses. HSFL parallel to laser polarization exists in the initial LIPSS formation stage, having the periodicity of about 340-350 nm. As laser pulse number increases, HSFL parallel to laser polarization disappear and HSFL ripples perpendicular to laser polarization appear with the periodicity of about 340 nm, nearly half the periodicity of LSFL.

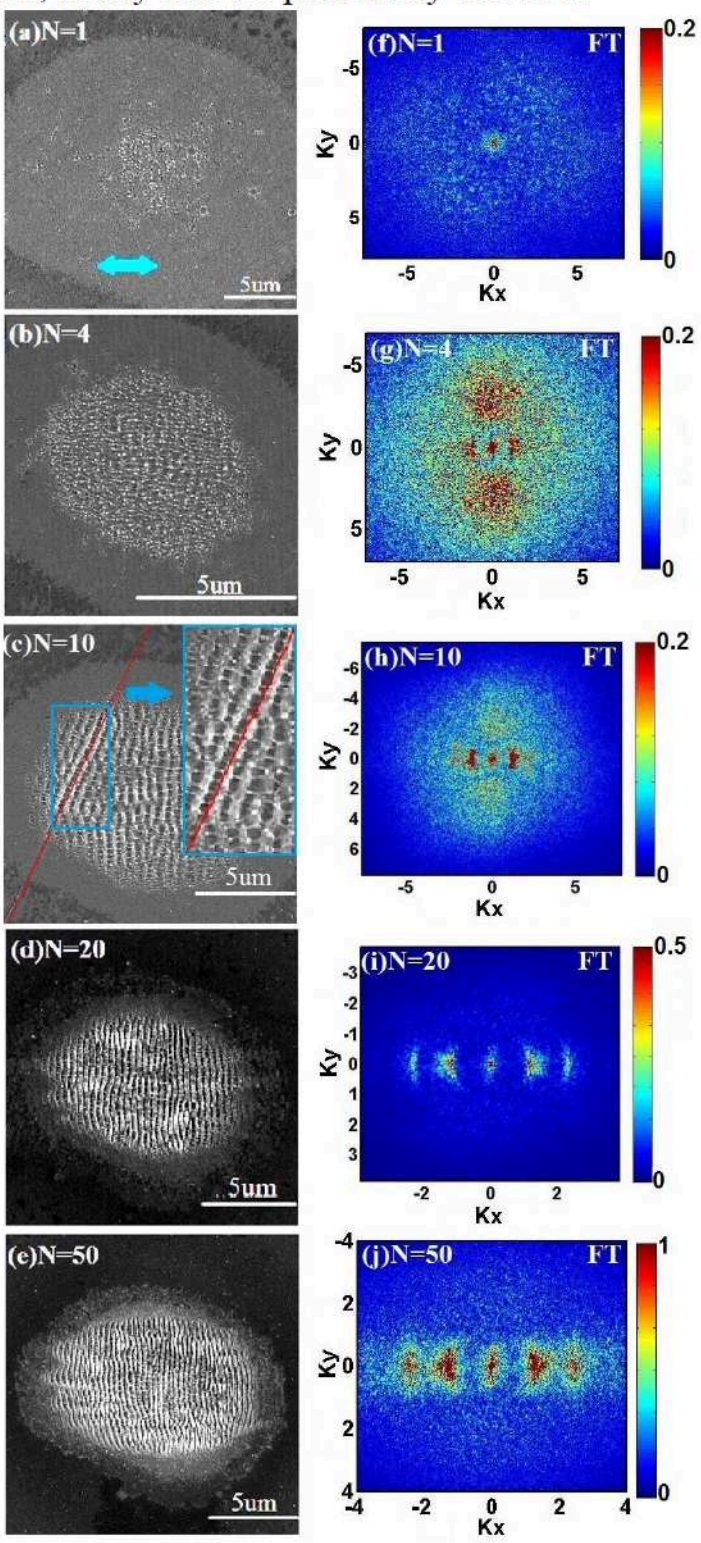

Figure 5.8: SEM images of the CMSX-4surface after irradiation with an increasing number of linearly polarized laser pulses at the fluence of F = 0.507 J·cm^{-2}. The respective pulse numbers are as follows: (a) N=1; (b) N=4; (c) N=10; (d) N=20; (e) N=50; (f) 2D-FFT of the image (a), representing the periodicity in the k-space; (g) 2D-FFT of the image (b); (h) 2D-FFT of the image (c); (i) 2D-FFT of the image (d); (j) 2D-FFT of the image (e). The laser polarization is indicated with a double-headed arrow in (a).

5.1.5 LIPSS experiments on the amorphous alloy Zr-BMG and its corresponding crystal alloy Zr-CA

Zr-based Bulk metallic glasses (Zr-BMG) are solid non-crystalline metallic alloys with disordered atomic-scale structure and ideal material supports for micro geometries due to lack of crystallites, grain boundaries and dislocations in material structure. Zr-BMG $Zr_{41.2}Ti_{13.8}Cu_{12.5}Ni_{10}Be_{25.5}$ (at%) is studied in our work.

The lattice structure of Zr-BMG can be controlled by annealing at special temperature above crystallization temperature, applied pressure and annealing time. Reference [Wan02] shows that the lattice structure of Zr-BMG transforms to stable crystalline phases: a significant amount of Zr_2Cu phase (tetragonal, a=0.32 nm, c=1.14 nm), an $MgZn_2$ type of Laves phase ZrTiNi (hex, a=0.52 nm, c=0.85 nm), and a small amount of Zr_2Ni phase after annealing at and above 773K for 5 hours. In our work, Zr-based crystalline alloy (Zr-CA) was obtained by annealing Zr-BMG at 800K for 50 hours. After crystallization of Zr-BMG, lattice structures and properties change.

Single-side polished Zr-BMG and Zr-CA samples are used in the experiment. Polishing was done by diamond paste and alumina powder with grit size down to 0.1 µm. Zr-BMG and CA samples before experiments are identified by electron back-scatter diffraction (EBSD) and confirmed as amorphous or crystalline. The optical indices of Zr-BMG and Zr-CA samples were evaluated ex-situ by using a commercial ellipsometer (Uvisel, Horiba Jobin Yvon). Under 800 nm-wavelength irradiation, the refractive index of Zr-BMG is ñ= 3.114+3.679i and the refractive index of Zr-CA is ñ =2.591+3.301i. Before and after the fs laser ablation, the samples are cleaned in an ultrasonic ethanol bath for 5~10 min.

The first striking element comes from the inspection of the surface topography for the two materials. The surface topologies of the Zr-BMG and Zr-CA samples were analyzed using SEM. Fig. 5.9 presents SEM images of pristine Zr-BMG and Zr-CA surfaces with the following characteristics. Zr-BMG surface has a flat aspect with low roughness (a defect hole is shown in Fig. 5.9(a) as a reference). The annealing treatment had nonetheless as strong influence on the

CA, as we observe a range of high-density randomly-distributed nano-particles with the size smaller than 200 nm on Zr-CA surface (Fig. 5.9(b)). These are intrinsically related to the process of re-crystallization, generating thus a surface with nano-protuberances in the 100-200 nm range and 200-300 nm spacing.

Energy dispersive X-ray spectrometry (EDX) analysis of the chemical composition (inset in Fig. 5.9(b)) indicates that the main elements composing the nanoparticles are Zr and Cu demonstrating potential nano-particles of Zr_2Cu crystalline phase in the Zr-CA. The two different topographies will have a strong influence on the formation of LIPSS.

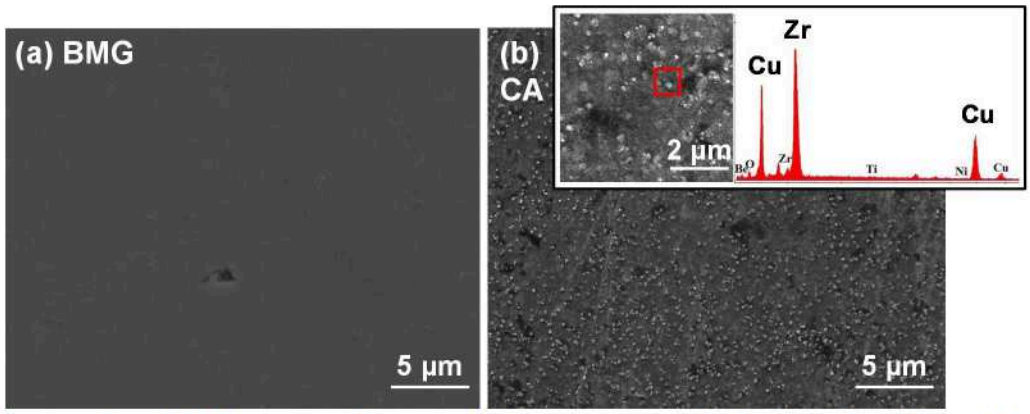

Figure 5.9: SEM images of (a) Zr-BMG surface and (b) Zr-CA surface. The presence of nano-particulates and protuberances is visible for the crystalline alloy surface and is a product of the annealing procedure. Inset: EDX analysis of nano-crystallites.

In order to investigate lattice structure effects on LIPSS formation, comparison experiments about LIPSS formation on Zr-BMG and Zr-CA are carried out. The morphology of the laser-induced periodic microstructure is examined aposteriori by SEM and the periodicity of ripples is analyzed by two-dimensional Fast Fourier Transform (2D-FFT). The difference of surface topology is analyzed and discussed in the following.

At laser fluence of 0.38 $J \cdot cm^{-2}$, LIPSS on Zr-BMG with increasing pulse number from 1 to 50 are shown in Fig. 5.10(a1-f1). In contrast, LIPSS on Zr-CA are shown in Fig. 5.10(a2-f2). Except LSFL ripples perpendicular to laser polarization on both Zr-BMG and Zr-CA after 1 pulse, HSFL ripples parallel to laser polarization appear only on Zr-CA within 10 pulses. The periodicity of LIPSS is analyzed by two dimensional Fast-Fourier-transform (2D-FFT). Fig. 5.11(a) is the 2D-FFT of Fig. 5.10(c1), representing the spatial periodicity in the k-space, which shows LSFL ripples perpendicular to laser polarization with a quasiconstant periodicity centered at 742

nm on Zr-BMG. In contrast, Fig. 5.11(b) is the 2D-FFT of Fig. 5.10(c2), which shows LSFL ripples perpendicular to laser polarization with a quasiconstant periodicity centered at 708 nm and HSFL ripples parallel to laser polarization with a quasiconstant periodicity centered at 384 nm.

At laser fluence of 0.15 J·cm^{-2}, LIPSS on Zr-BMG with 20, 50, 100 pulses are shown in Fig. 5.10(g1-i1). In contrast, LIPSS on Zr-CA are shown in Fig. 5.10(g2-i2). The difference is that LIPSS on Zr-BMG shows more regular than LIPSS on Zr-CA. This is because that Zr-BMG lacks crystallites, grain boundaries and dislocations in material, and is easier to form regular ripples due to the plasticity.

At laser fluence of 0.60 J·cm^{-2}, LIPSS on Zr-BMG with 1, 2, 4 pulses are shown in Fig. 5.10(j1-l1). In contrast, LIPSS on Zr-CA are shown in Fig. 5.10(j2-l2). Obviously, after 4 laser pulses, Zr-CA has LIPSS in the center. However, the spot center is a flat surface without LIPSS on Zr-BMG. This can be put in connection with the achievement a certain thickness of a heated, low viscosity "liquid" layer that will attenuate and damp spatial light modulation or capillary waves.

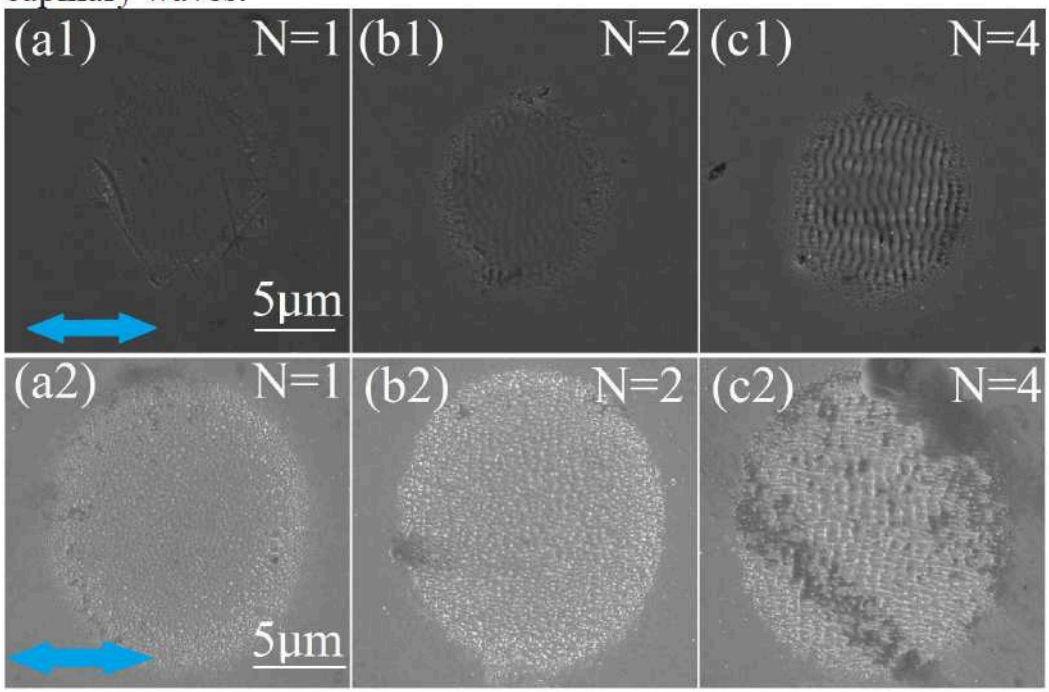

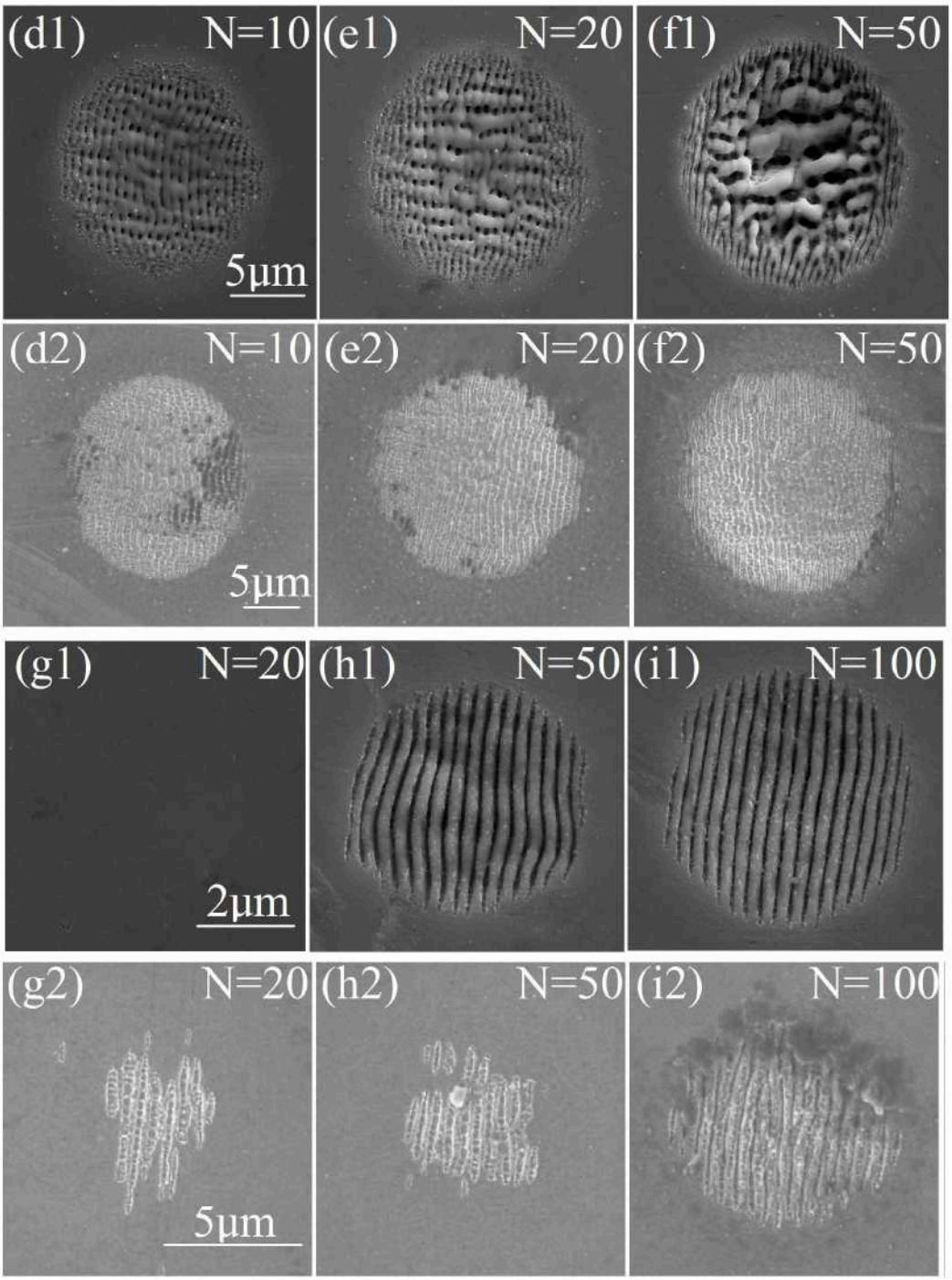
(d1) N=10
5μm
(e1) N=20
(f1) N=50
(d2) N=10
5μm
(e2) N=20
(f2) N=50
(g1) N=20
2μm
(h1) N=50
(i1) N=100
(g2) N=20
5μm
(h2) N=50
(i2) N=100

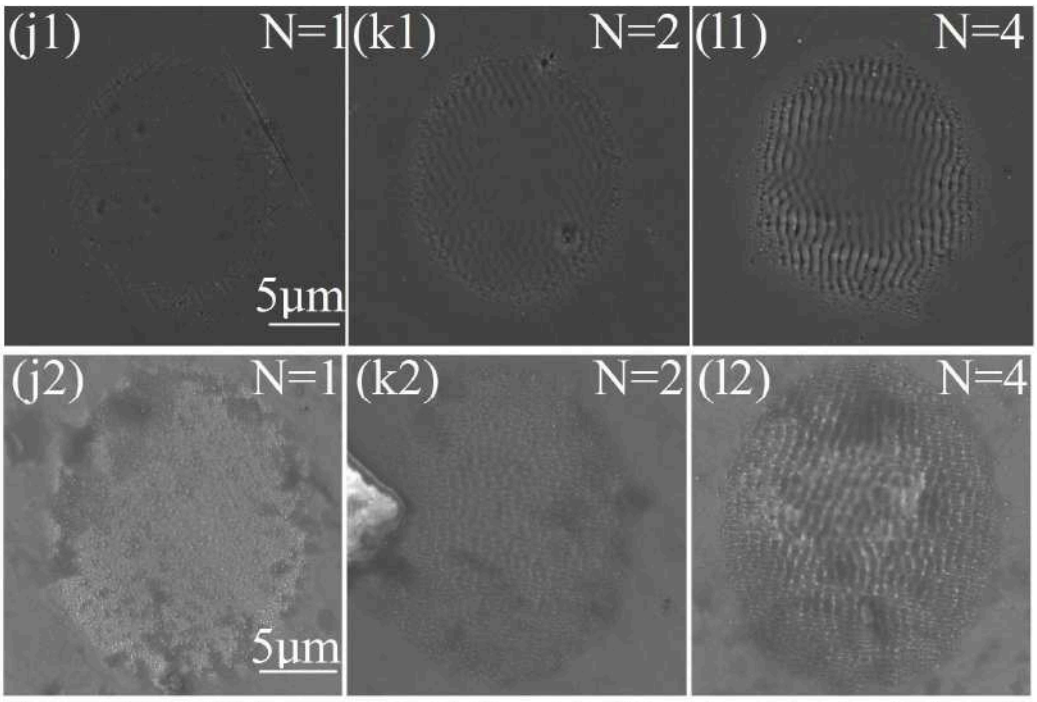

Figure 5.10: SEM images of Zr-BMG and Zr-CA surface after irradiation with linearly polarized laser pulses at different fluences: (a1-f1) Zr-BMG, (a2-f2) Zr-CA at ϕ=0.38 J·cm^{-2}; (g1-i1) Zr-BMG, (g2-i2) Zr-CA at ϕ=0.15 J·cm^{-2}; (j1-l1) Zr-BMG, (j2-l2) Zr-CA at ϕ=0.60 J·cm^{-2}.The pulse number is shown in every image. The electric polarization direction of the laser beam is indicated with a double-headed arrow in (a1, a2).

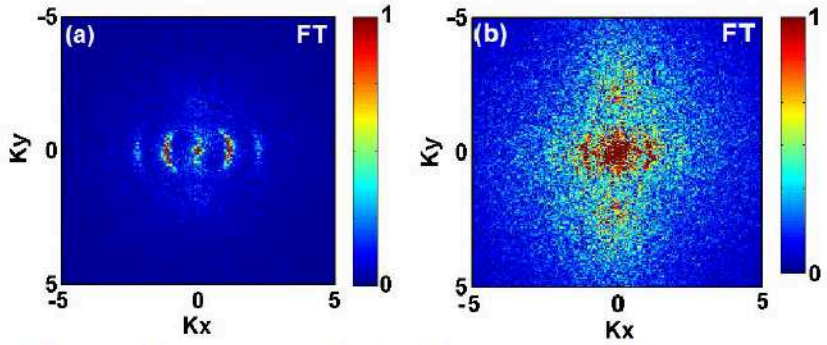

Figure 5.11: (a) 2D-FFT of Fig. 5.10(c1), representing the spatial periodicity in the k-space on Zr-BMG; (b) 2D-FFT of Fig. 5.10(c2), representing the spatial periodicity in the k-space on Zr-CA.

In summary, the differences of surface topologies in amorphous and crystalline Zr-based superalloys affect LIPSS formation. Three differences of LIPSS upon the accumulation of laser pulses at various fluences are observed: (1) At low laser fluence, LIPSS on Zr-BMG shows more regular aspect than LIPSS on Zr-CA. (2) At moderate fluence, except LSFL ripples perpendicular to laser polarization on both Zr-BMG and Zr-CA, HSFL ripples parallel to laser polarization appear only on Zr-CA within 10 pulses. (3) At

high laser fluence, Zr-CA has LIPSS in the center. However, the spot center is a flat surface without LIPSS on Zr-BMG.

Comparing the results we may deduce that the formation of HSFL ripples on Zr-CA is strongly related to the specific nano-structured surface of Zr-CA with a high density of nanoparticles, while LSFL generation can be related to an initial roughness as well as to a laser-induced evolving topology on both surfaces in terms of laser-induced additional roughness and corrugation. We will discuss the consequences of the high density nano-roughness on electromagnetic energy distribution in the vicinity of the surface in next Chapter.

However, beside the nanoscale roughness, Zr-BMG and Zr-CA present opposite thermodynamic features notably a thermoplastic character for Zr-BMG and a more brittle character with sharp thermodynamic transition points for Zr-CA. The thermoplastic moldable character of Zr-BMG is presumably responsible for the quality arrangement and morphology of LSFL. The HSFL morphology on Zr-CA depends on the input energy and ranges from droplet-like forms to inner-structure texturing, suggesting equally a dewetting mechanism. This shows a strong inter-relation between field and thermodynamic issues in building a comprehensive scenario for ripple formation. We will see below subtle changes in structure and composition of the Zr-BMG.

5.2 Crystallization effects during fs ablation of Zr-BMG

Besides structure changes, the question is if the structure was equally altered, and we will observe structural changes in Zr-BMG. Femtosecond laser can induce crystallization in some amorphous materials [ZLZ+15, LHW+15, EKK+14]. In our case the analysis of surface crystallization in the laser impact area is performed using a scanning electron microscope (SEM, Zeiss Supra55 FEG-SEM), equipped with an HKL-Oxford Instruments EBSD system composed of a Nordlys II camera and Channel 5 software suit. EBSD acquisitions were performed with the accelerating voltage varying from 7 to 20 keV, with a working distance of 15 mm and sample tilt of 70◦ with respect to horizontal. The spatial resolution of the EBSD is typically about 20nm×60nm×10nm (horizontal axis×tilted axis×depth) [SMF+14]. Direct interrogation of EBSD pattern (EBSP) is used to analyze the lattice structure by EBSD data analysis after LIPSS formation.

Fig. 5.12(a) shows the SEM image of the LIPSS on Zr-BMG surface, which is made by 50 pulses at laser fluence of 0.67 J·cm^{-2}. Fig. 5.12(b) is the EBSD diffraction pattern, measured from the small region marked in a red cross in Fig. 5.12(a). EBSD diffraction pattern shows the existence of crystalline phase in nano-size region on LIPSS, which is mostly the tetragonal phase, potentially Zr_2Cu. It is to be emphasized though that these structures appear only at a relatively high number of pulses and are not typically found in the rippled area.

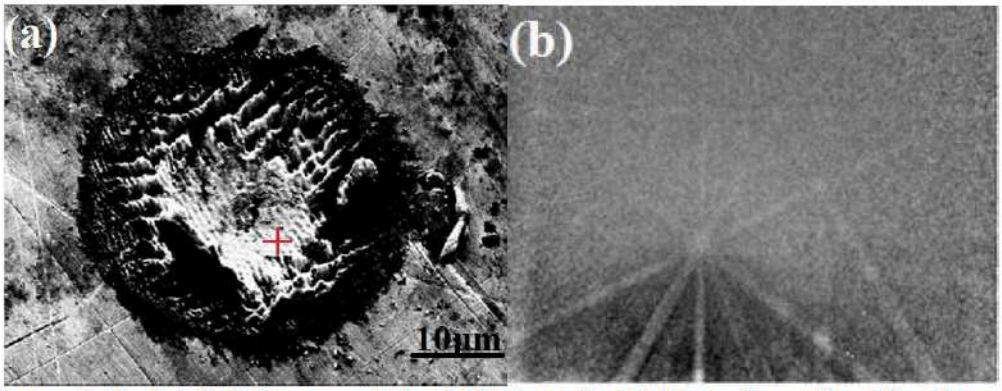

Figure 5.12: (a) SEM image of the LIPSS on Zr-BMG surface after 50 pulses at laser fluence of 0.67 J·cm^{-2}. (b) EBSD diffraction patterns measured from the small region marked in a red cross in (a).

5.3 Conclusion

In this chapter, the experiments of fs-LIPSS on six different materials are carried out, involving metal tungsten, semiconductor silicon, dielectric fused silica, single-crystal superalloy CMSX-4, amorphous alloy Zr-BMG and its corresponding crystal alloy Zr-CA. The experimental results of LIPSS are respectively summarized below.

On tungsten, there are two types of LIPSS: LSFL and HSFL ripples perpendicular to laser polarization. For LSFL on W, the SPP seems to contribute only to a minor extent for LSFL formation on the planar W. The initial SPP-laser interference and the subsequent grating-assisted SPP-laser coupling indicate the smaller periodicity in the periphery area than the center area of the irradiated spot, which is not consistent with our experiment results of the smaller periodicity in the center area. In result, it is a question if the SPP contribute to the LSFL formation on tungsten.

For silicon, there are only LSFL ripples perpendicular to laser polarization. With the increase of laser pulse numbers, the LSFL periodicity gradually decreases, which is in the range of 744 - 614

nm. LSFL formation on silicon can be explained by Sipe theory and Drude model, revealing the main effects of rough surface (surface nanostructures) and the intra-pulse transient optical indices.

For fused silica, there are two types of LIPSS: HSFL ripples perpendicular to laser polarization ($\perp$E), LSFL ripples parallel to laser polarization ($\parallel$E). In case of dielectrics, refractive light components play a larger role and a stronger flexibility as a function of the local fluence can be foreseen.

For CMSX-4, three are three kinds of LIPSS: LSFL ($\perp$E), HSFL ($\parallel$E) and HSFL ($\perp$E). LSFL ($\perp$E) has the periodicity of 725-629 nm and the periodicity decreases gradually with an increasing number of laser pulses. HSFL ($\parallel$E) exists in the initial LIPSS formation, having the periodicity of about 340-350 nm. As laser pulses increase, after HSFL ($\parallel$E) disappears and HSFL ripples ($\perp$E) appear with the periodicity of about 340 nm, nearly half the periodicity of LSFL.

In the comparison of LIPSS on Zr-BMG on Zr-CA, we may deduce that the formation of HSFL ripples on Zr-CA is strongly related to the specific nano-structured surface of Zr-CA with a high density of nanoparticles, while LSFL generation can be related to an initial roughness as well as to a laser-induced evolving topology on both surfaces in terms of laser-induced additional roughness and corrugation. However, beside the nanoscale roughness, Zr-BMG and Zr-CA present opposite thermodynamic features notably a thermoplastic character for Zr-BMG and a more brittle character with sharp thermodynamic transition points for Zr-CA. The thermoplastic moldable character of Zr-BMG is presumably responsible for the quality arrangement and morphology of LSFL.

From the view of lattice structure, the laser-induced crystallization on amorphous alloy Zr-BMG is evidenced by electron back-scatter diffraction (EBSD). Although LIPPS pattern are mainly amorphous, at large doses EBSD diffraction pattern shows the existence of crystalline phase in nanoscale region on LIPSS, which is maybe the tetragonal phase Zr_2Cu.

LIPSS experimental results in this chapter will provide the experimental data for investigating the LIPSS formation mechanism in next chapter.

Chapter 6

LIPSS formation mechanisms and the role of micro/nano-structures

Here we approach using numerical solving of Maxwell equations the topic of light interaction with rough surfaces, emphasizing the role of nanostructures in determining periodic scattered field patterns. We will thus offer an electromagnetic perspective on the apparition of spatially modulated light fields.

LIPSS formation involves a complex chain of physical processes, which have been introduced in Chapter 2. LIPSS formation is affected by irradiation and material conditions. Particularly, ultrafast laser can induce the transient changes of optical properties in matter, which has been investigated and discussed in Chapter 4. In Chapter 5, fs-LIPSS experiments on tungsten, silicon, and metallic superalloys in three structural configurations (CMSX-4, Zr-BMG and Zr-CA) show different LIPSS characteristics, however, LIPSS formed on the these materials have a common point: LSFL structures form perpendicular to the laser polarization, revealing a common formation mechanism of regular LIPSS on metal, semiconductor and alloys.

Because of the complexity of LIPSS formation, the growth mechanisms of some LIPSS features are not yet fully understood. Several mechanisms of LIPSS formation have been introduced with their merits and drawbacks in Chapter 2. Among them, Sipe theory is widely accepted to describe the LIPSS formation, based on the interference between the incident laser and surface-scattered electromagnetic wave [SYP+83, YPD+83]. Sipe theory is a useful and valuable approach, which relies on diffraction to explain periodic optical coupling features and predicts major LIPSS

characteristics in a simpler, intuitive form. However, Sipe theory is an approximate solution of the scattered field induced by a simple rough surface model [SYP+83]. Finite-difference time-domain (FDTD) approach is a precise numerical method that can simulate the interference and scattering of the electromagnetic waves on rough surfaces [SRO+12]. Therefore in order to overcome approximations in Sipe theory, FDTD simulations are used to investigate qualitatively the LIPSS formation on rough surfaces and the role of micro/nano-structures in LIPSS formation.

In this chapter, at first, FDTD method is briefly introduced and then it is used to simulate the case of Sipe theory on a comparative basis. Secondly, localized surface plasmon in nanostructures, its effect on scattering electromagnetic wave, as well as the roles of micro/ nano- structures in LIPSS formation are introduced and analyzed by FDTD simulations. Finally, the formation mechanisms of LSFL and HSFL on several superalloys are respectively analyzed and discussed.

6.1 FDTD method

Maxwell's equations are fundamental to any description of light-matter interactions. Differential Maxwell's equations are given below, including Ampere's law, Faraday's law, Gauss's law for electric field, and Gauss's law for magnetic field respectively.

$$\varepsilon \frac{\partial E}{\partial t} + \sigma E = \nabla \times H \tag{6-1}$$

$$\mu \frac{\partial H}{\partial t} = -\nabla \times E \tag{6-2}$$

$$\nabla \cdot \mu H = 0 \tag{6-3}$$

$$\nabla \cdot \varepsilon E = 0 \tag{6-4}$$

Here t is the time, μ is permeability, ε is permittivity, σ is the conductivity, E is the electric field and H is the magnetic field.

Finite-difference time-domain (FDTD) method can solve Maxwell's equations numerically. The method was introduced by Yee in 1966 [Yee66]. In Yee's algorithm, Maxwell's curl equations (6-1) and (6-2) are expressed in a Cartesian frame. To numerically evaluate the equations, central differences are used for the finite-difference expressions of the space and time derivatives. For example, applying the central differences to all derivatives equation (6-1) along the X axis and denoting the temporal grid by a superscript n, one arrives at the following finite-difference update equations [TH05]:

$$E_{\mathrm{x}}\Big|_{i,j,k}^{n+1} = E_{\mathrm{x1}}\Big|_{i,j,k} E_{\mathrm{x}}\Big|_{i,j,k}^{n}$$
$$+E_{\mathrm{x2}}\Big|_{i,j,k}\left(H_{\mathrm{z}}\Big|_{i,j+1/2,k}^{n+1/2} - H_{\mathrm{z}}\Big|_{i,j-1/2,k}^{n+1/2} + H_{\mathrm{y}}\Big|_{i,j,k-1/2}^{n+1/2} - H_{\mathrm{y}}\Big|_{i,j,k+1/2}^{n+1/2}\right) \quad (6\text{-}5)$$

$$E_{\mathrm{x1}}\Big|_{i,j,k} = \frac{1-\sigma_{i,j,k}\Delta t/(2\varepsilon_{i,j,k})}{1+\sigma_{i,j,k}\Delta t/(2\varepsilon_{i,j,k})} \quad (6\text{-}6)$$

$$E_{\mathrm{x2}}\Big|_{i,j,k} = \frac{\Delta t/(\varepsilon_{i,j,k}\Delta)}{1+\sigma_{i,j,k}\Delta t/(2\varepsilon_{i,j,k})} \quad (6\text{-}7)$$

Here superscript n indicates the time steps, Δt is the time increment, Δ is the space increment, and i, j and k are the discretized space coordinates.

Fig. 6.1 shows a Yee unit cell. In Yee cell, electric and magnetic field vector components are distributed. Each component of E and H is respectively surrounded by four circulating components of H and E. A three-dimensional space lattice consists of a multiplicity of such Yee cells. The so-called leapfrog arrangement of Yee cell is used for the time derivatives, meaning that each component of H is computed and stored using a previous E, then all the E components are updated from H and the cycle starts again. An electromagnetic wave interaction structure is mapped into the space lattice by assigning appropriate values of permittivity to each electric field component, and permeability to each magnetic field component [Yee66].

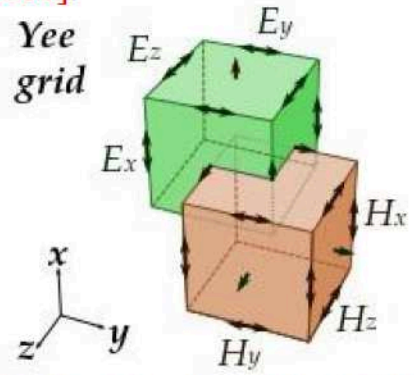

Figure 6.1: Yee unit cell used for FDTD [Yee66].

In order to ensure the simulation accuracy, the dimensions of Yee cell (Δx, Δy, Δz) are chosen by

$$(\Delta x, \Delta y, \Delta z) \leq \lambda/(10n) \quad (6\text{-}8)$$

where λ is the laser wavelength; n is the refractive index of the medium. When the dimensions of Yee cell are determined, in order to ensure the algorithm's numerical stability, the increment Δt follows the condition [TH05]:

$$\Delta t_{\max} = c^{-1}\left(\frac{1}{\Delta x^2}+\frac{1}{\Delta y^2}+\frac{1}{\Delta z^2}\right)^{-\frac{1}{2}} \tag{6-9}$$

Here, c is the light speed; (Δx, Δy, Δz) are the dimensions of the space grid. Uniaxial Perfectly matched layer (UPML) method was used as absorbing boundary condition, to avoid nonphysical reflections. FDTD method has been a powerful engineering tool for integrated and diffractive optics device simulations [TH05].

In this chapter, FDTD method is used to compute the inhomogeneous energy distribution of electromagnetic field on the surface.

6.2 FDTD simulations on Sipe theory

Sipe theory has been largely applied to describe the LIPSS formation, based on the interference between the incident laser and surface-scattered electromagnetic wave [YPD+83, SYP+83]. The Sipe theory can predict major features of periodic field patterns and optical coupling, however the approximate description of roughness and interaction can be improved using FDTD.

In this section, at first, a Sipe model about LIPSS formed on Ge and Al is calculated. Next, compared with Sipe theory, 3D-FDTD simulations are used to estimate modulated fields and thus anticipate the LIPSS positions on Ge and Al. Finally， FDTD simulations on energy distribution induced by nanoscale hemispheres on surface are performed to investigate the origin of LIPSS formed on rough surface.

6.2.1 Sipe theory about LIPSS formed on Ge and Al

J. E. Sipe et al developed the theory of LIPSS formation by associating the Fourier component of LIPSS with the corresponding Fourier component of inhomogeneous energy deposition beneath the surface [SYP+83]. Sipe theory describes the electric field intensity distribution created by a plane wave incident on a thin, rough surface selvedge region, whose height is much less than wavelength. In Sipe theory, the surface roughness is built according to the shape factor s and filling factor F. Sipe theory provides an expression for the inhomogeneous energy deposition on the surface, which is proportional to $\eta(K, K_i)\times|b(K)|$, where the efficacy factor $\eta(K, K_i)$ describes the efficacy with which the roughness leads to an inhomogeneous energy absorption at K; $|b(K)|$ represents a measure

of amplitude of the surface roughness at K. It is assumed that ripples grow where the absorbed energy is the largest. $|b(K)|$ varies slowly for a surface with homogeneously distributed roughness, and the efficacy factor $\eta(K, K_i)$ exhibits sharp peaks at certain K values, so the efficacy factor $\eta(K, K_i)$ determines the spatial ripple periodicity [SYP+83].

The efficacy factor $\eta(K, K_i)$ is calculated according to the formulas of Sipe theory in the reference [SYP+83]. The shape factor s and filling factor F are set to be (F, s) = (0.1, 0.4) for the rough surface [SYP+83]. Fig. 6.2(a) gives the two-dimensional η map for 1060-nm p-polarized laser radiation incident on Ge at the incident angle 60°. The laser polarization is parallel to the X axis. The refractive index of Ge is $\tilde{n}$=4+0.1i at 1060-nm wavelength. In Fig. 6.2(a), there are clearly observable intersecting circular patterns that correspond to quasi periodic field energy patterns in the real space. In the wave-vector space (η map), the double rings center at $\pm(2\pi/\lambda)\times\sin(60°)$ with the radius of $(2\pi/\lambda)$, derived from the synchronism condition involving momentum conservation between the surface scattered wave vector and the non-normally incident beam [SYP+83]. Inhomogeneous energy focuses on the lateral side-part of the intersecting circular patterns, which relates to the period and direction of ripples, where energy deposition peaks. Fig. 6.2(b) is the two-dimensional η map for 1060-nm s-polarized laser radiation incident on Ge at the incident angle 60°. The laser polarization is parallel to Y axis. In Fig. 6.2(b), we can observe intersecting circular patterns and two fan-shaped structures outside the crossed circles in K_x axis. Inhomogeneous energy deposition occurs preferentially in patterns corresponding to two fan-shaped structures.

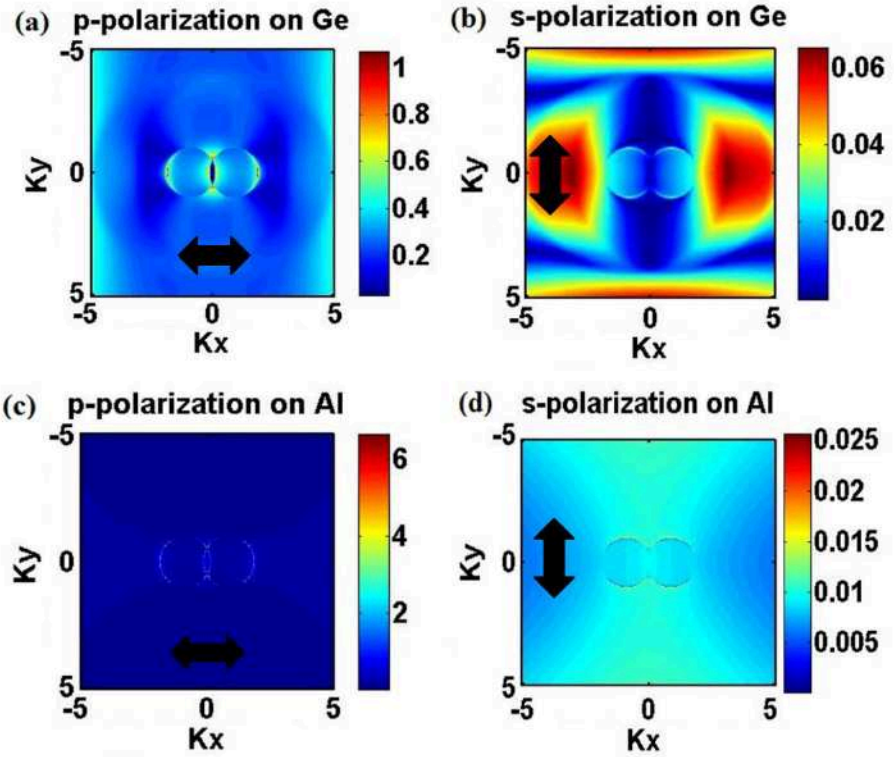

Figure 6.2: 2D-η maps for 1060-nm p-polarized laser at the incident angle 60° and (F,s) = (0.1,0.4). (a) 2D-η map for p-polarized laser on Ge (ñ=4+0.1i); (b) 2D-η map for s-polarized laser on Ge; (c) 2D-η map for p-polarized laser on Al (ñ=1.8+9.3i). (d) 2D-η map for s-polarized laser on Al. The polarization direction is indicated by black arrow.

Fig. 6.2(c) represents the two-dimensional η map for 1060-nm p-polarized laser incident on Al at the incident angle 60°. The laser polarization is parallel to X axis. The refractive index of Al is $\tilde{n}$=1.8+9.3i at 1060 nm wavelength. Here we can observe only intersecting circular patterns. Inhomogeneous energy focuses on part of intersecting circular patterns corresponding to the external lateral lobes. Fig. 6.2(d) is two-dimensional η map for 1060-nm s-polarized laser incident on Al at the incident angle 60°. The laser polarization is parallel to Y axis. In Fig. 6.2(d), inhomogeneous energy focuses on part of double crossed circles corresponding to the vertical lobes.

In their experiment, J. E. Sipe, J. F. Young *et al.* reported LIPSS on Ge, Si, Al and brass by linearly polarized 1060-nm nanosecond laser pulses. Incident angle and beam polarization are changed in the experiment. They analyzed the information from the Fourier transform of LIPSS via an experimental Fraunhofer diffraction pattern produced by exposing the LIPSS-patterned surface to a cw laser beam. For example, Fig. 6.3 shows the photograph of the diffraction pattern reflected on Ge surfaces with LIPSS generated by p-polarized 1060-nm radiation incident at the angle of 60°. There are 3 types of ripples: type s^+, type s^-, type c and

exceptionally bright dots seen in Fig. 6.3. Type s^+ and type s^- represent the ripples perpendicular to the laser polarization, and type s^+ has smaller periods, while type s^- has larger periods than laser wavelength. The difference in wavelength derives directly from the synchronism condition involving momentum conservation between the ripples wavevector and the non-normally incident beam [SF86]. Type c represents the ripples parallel to the laser polarization. We draw attention to the visible dots in Fig. 6.3 which may correspond to the ripples with period close to laser wavelength parallel to the polarization. The exceptionally bright dots are only seen on Ge, however, not seen on Al at any incident angle. This feature does not explicitly appear from a Sipe theory analysis and therefore this was thought be linked to the role of feedback and details of the actual damage approach [YPD+83].

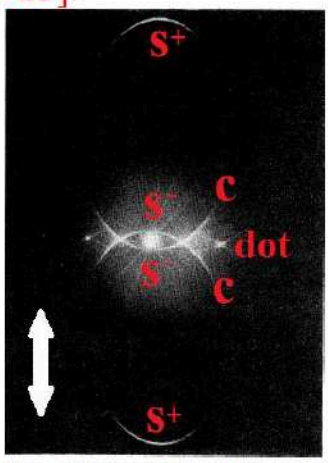

Figure 6.3: Photograph of the diffraction pattern reflected on Ge with LIPSS fabricated by p-polarized 1060-nm radiation incident at the angle of 60°. The polarization direction is indicated by the white arrow [YPD+83].

In Sipe theory, the electromagnetic field is decomposed into longitudinal and transverse components. The longitudinal component is short ranged and responsible for the local field collections, which is treated by a variation principle and finding an approximate solution for polarization in the selvedge. The transverse component describes multiple scattering, which is treated by a perturbation series [SYP+83]. From here a certain loss of accuracy may be corrected using numerical approaches.

6.2.2 3D-FDTD simulations about LIPSS on Ge and Al

Sipe theory only solved the inhomogeneous energy deposition beneath the rough surface. In order to study the energy transfer from the electromagnetic field above the surface to the material beneath the rough surface, both the energy distribution above and beneath the

rough surface of Ge and Al are calculated by 3D-FDTD method. The rough surface is irradiated at the incident angle of 60° in air with p-or s-polarized laser pulses of 20-ns duration at 1060-nm wavelength in the simulation model. The refractive indices are chosen to be the same as in Fig. 6.2. The surface roughness is built according to the shape factor s and filling factor F. The nanoparticles with the same size of 25 nm × 25 nm × 40 nm are used according to the shape factor *s* of 0.4, which is related to the spherical particle appropriately. There is 10% of all the surface area filled up with these nanoparticles in a random manner, according to filling factor *F* of 0.1. The range of rough surface selvedge region is 0-40 nm in Z axis. The bulk material is below the surface and air is above the surface. The incident plane is in XOZ plane. The p-polarization is along X axis and s-polarization is along Y axis. The electric field amplitude of the plane wave is set to 1 V/m. Total-field scattered-field (TFSF) method and perfect match layer (PML) boundary are used in the simulation. Because the simulation time of 20 nanoseconds needs lots of memory in computer, only 100 femtoseconds in the middle of one pulse are chosen as the simulation time. The simulation results show that 100 femtoseconds are enough for the calculation accuracy.

At first, the exposed semiconductor Ge is simulated and the results are shown in Fig. 6.4. Fig. 6.4(a) shows thus the time-averaged E^2 for the simulation time for Ge at the plane of Z=0.15 μm above the surface in the case of p-polarized plane wave incident at the angle 60°. Fig. 6.4(b) is 2D Fourier transform of Fig. 6.4(a), which is similar to the efficacy factor η map in Fig. 6.2(a). The type s^+ in the intersecting circular patterns and the exceptionally bright dots are seen in Fig. 6.4(b). So the exceptionally bright dots can be seen in one pulse, not linked to the role of inter-pulse feedback between laser pulses and evolving surface proposed in Ref. [YPD+83].

Fig. 6.4(c) shows the time-averaged E^2 for the simulation time for Ge at the plane of Z=-0.03 μm plane below the surface by p-polarized plane wave incident at the angle 60°. Fig. 6.4(d) is 2D Fourier transform of Fig. 6.4(c). The intersecting circular patterns which show diffuse localization (without specifically defined wavevectors) and two fan-shaped structures outside the crossing circles along Kx axis are seen in Fig. 6.4(d). Comparing Fig. 6.4(b) with Fig. 6.4(d), the double crossed circles exist above the surface, but they are not clearly defined below the surface. Double crossed circles are induced by the interference between the scattered light and incident laser [YPD+83]. Below the surface, the effect of

interference between the scattered light and incident laser becomes weak in view of the losses. Two fan-shaped structures are only seen below the surface, so two fan-shaped structures along the laser polarization are related to the interference between scattered light and refracted light in Ge.

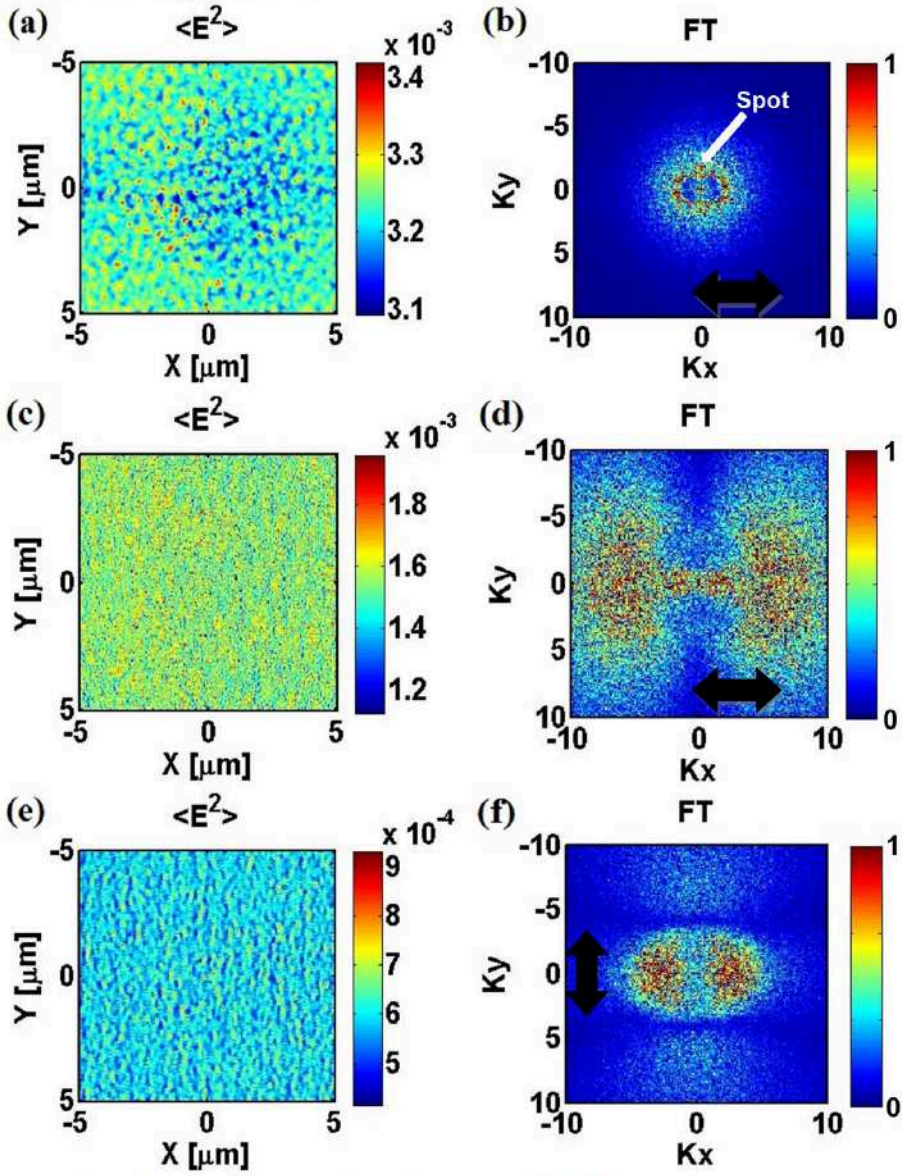

Figure 6.4: (a) Time-averaged E^2 for Ge at Z=0.15 μm above the surface for a p-polarized plane wave incident at 60°; (b) 2D- FT of (a); (c) Time-averaged E^2 for Ge at Z=-0.03 μm below the surface for a p-polarized plane wave incident at 60°; (d) 2D-FT of (c); (e) Time-averaged E^2 for Ge at Z=-0.03 μm below the surface for s-polarized plane wave incident at 60°; (f) 2D-FT of (e).

For the case of s-polarization, Fig. 6.4(e) shows the time-averaged E^2 (for the simulation time) for Ge at the plane of Z=0.15 μm above the surface for a plane wave incident at the angle 60°. Fig. 6.4(f) is 2D Fourier transform of Fig. 6.4(e), which is similar to the efficacy factor η map in Fig. 6.2(b). In Fig. 6.4(f), the

double crossed circles are not clear, two fan-shaped structures along K_x axis and two fan-shaped structures along K_y axis appear, which are also seen in Fig. 6.2(b). Two fan-shaped structures along the laser polarization are related to the interference between scattered light and refractive light in Ge as it will be discussed latter in the text.

Next, the metal Al is simulated and the results are shown in Fig. 6.5. Fig. 6.5(a) shows the time-averaged E^2 for the simulation time for Al at the plane of Z=0.15 μm above the surface in the case of a p-polarized plane wave incident at the angle 60°. Fig. 6.5(b) is 2D Fourier transform of Fig. 6.5(a), which is similar to the efficacy factor η map in Fig. 6.2(c). The type s^+ and type s^- ripples in the intersecting circular patterns and the exceptionally bright dots are seen in Fig. 6.5(b), in which bears similarities with Fig. 6.2(c), except the exceptionally bright dots.

Fig. 6.5(c) shows the time-averaged E^2 for the simulation time for Al at the plane of Z=-0.03 μm plane below the surface for a p-polarized plane wave incident at the angle 60°. Fig. 6.5(d) is 2D Fourier transform of Fig. 6.5(c). The double crossed circles and exceptionally bright dots are not seen in Fig. 6.5(d). This is because that metal Al has larger extinction coefficient than semiconductor Ge and less light could go through the surface region. In view of the losses the effect of interference between the scattered light and incident laser disappears gradually below the surface and the energy distribution transforms into the Gaussian shape of the k-vectors space.

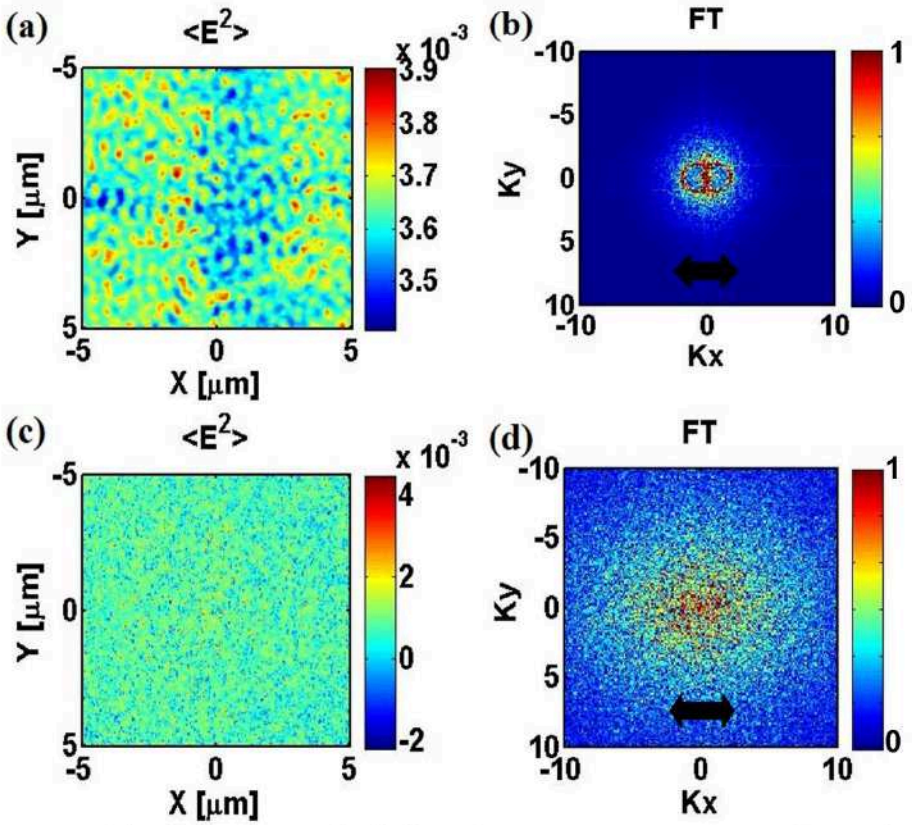

Figure 6.5: (a) Time-averaged E^2 for Al at Z=0.15 μm above the surface for p-polarized plane wave incident at the angle 60°; (b) 2D- FT of (a); (c) Time-averaged E^2 for Ge at Z=-0.03 μm below the surface for p-polarized plane wave incident at 60°; (d) 2D-FT of (c).

After the simulations of the energy distributions above and beneath the rough surface of Ge and Al, we found that 3D-FDTD method can simulate the case of Sipe theory successfully and offer more information about the energy transferring. So we will use the FDTD method to investigate the LIPSS formation.

6.2.3 FDTD simulations on energy distribution induced by nanoscale hemispheres on surface

In order to investigate the exceptionally bright dots in Fig. 6.4(b), 3D-FDTD simulations for a Ge hemisphere on Ge surface are analyzed. In the simulation model, a hemisphere is located in the coordinate origin and its radius is 0.1 μm. The incident plane wave has an incident angle of 60° in XOZ plane and it has the wavelength of 1060 nm. The p polarization is along X axis. The electric field amplitude of the plane wave is set to 1 V/m. Perfect match layer (PML) boundary is used in the simulation. Simulation results are shown in Fig. 6.6.

Fig. 6.6(a) shows time-averaged E^2 distribution on Ge flat surface with a Ge hemisphere of radius R=0.1 μm induced by the plane wave of 1060-nm wavelength at the incident angle of 60°. The electromagnetic energy distribution has a comet-like shape along X axis and it shows energy modulation around the hemisphere. Fig. 6.6(b) is the binary image of Fig. 6.6(a), which shows the periodic modulation clearly. Fig. 6.6(c) is 2D- FT of Fig. 6.4(b), which shows the two crossed circles in the center and part of bigger circles corresponding to diffraction. The exceptionally bright dots are junctions of bigger circles. So the exceptionally bright dots in Fig. 6.4(b) are due to the energy modulation induced by single nanoparticle on surface at large incident angle, which is an individual effect, just involving the interference between incident wave and scattered wave.

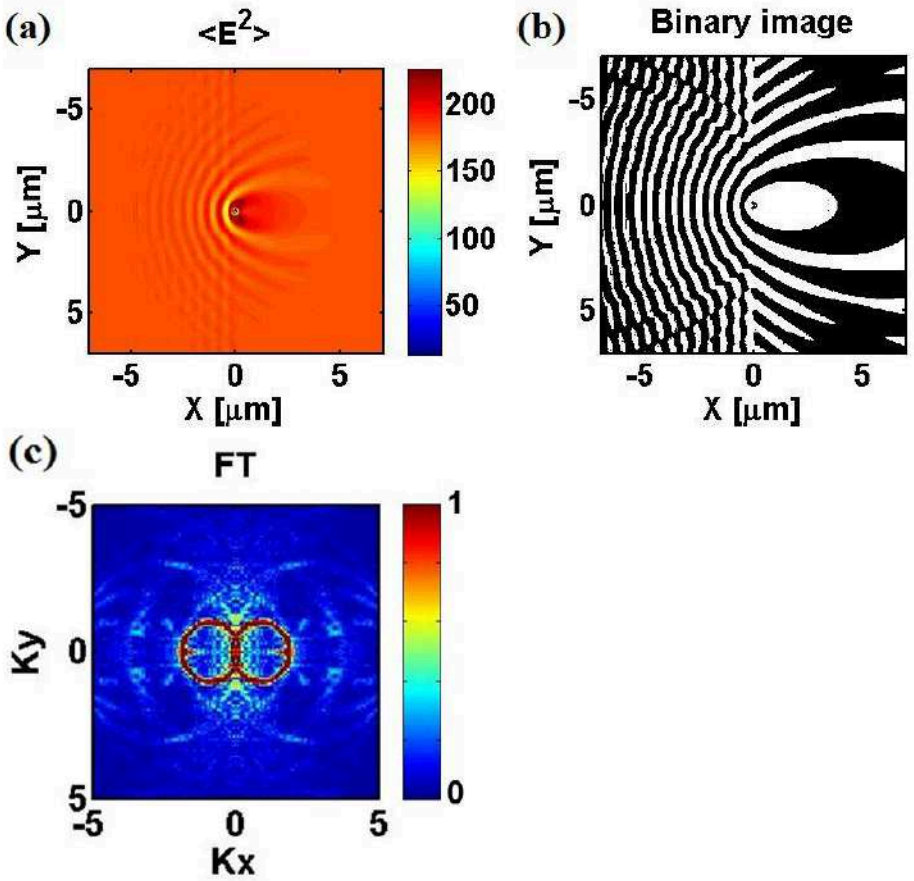

Figure 6.6 (a) Time-averaged E^2 distribution on Ge flat surface with a Ge hemisphere of radius R=0.1 μm induced by the plane wave of 1060-nm wavelength at the incident angle of 60°; (b) Binary image of (a); (c) 2D-FT of (b).

In order to study the energy deposition induced by an ensemble of hemispheres, 8 hemispheres are built in the same model. Simulation results are shown in Fig. 6.7. Fig. 6.7(a) shows

time-averaged E^2 distribution induced by the plane wave of 1060-nm wavelength on Ge flat surface with eight Ge hemispheres of radius R=0.1 μm positioned on the top of it. In Fig. 6.7(a), electromagnetic energy distribution is the sum of energy modulation induced by each hemisphere. Fig. 6.7(b) is the binary image of Fig. 6.7(a), which shows the periodic modulation clearly. Fig. 6.7(c) is 2D-FT of Fig. 6.7(b), which shows the two crossed circles in the center and part of bigger circles, similarly to energy deposition induced by 1 hemisphere.

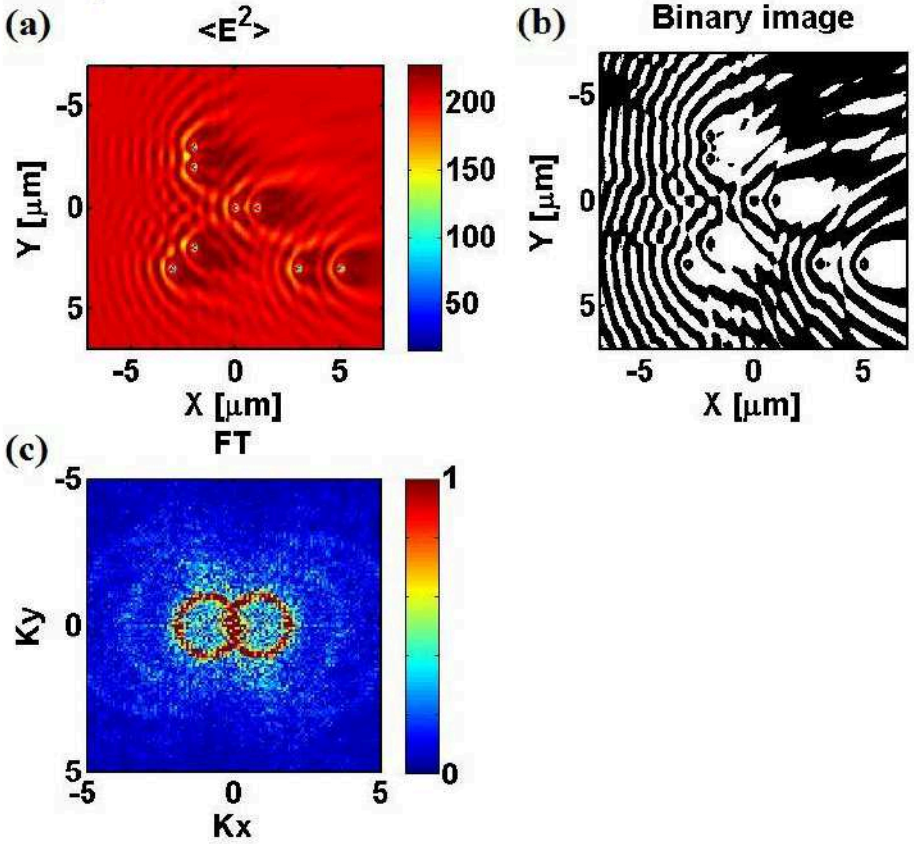

Figure 6.7: (a) Time-averaged E^2 distribution on Ge flat surface with eight Ge hemispheres of radius R=0.1 μm induced by plane wave of 1060-nm wavelength at the incident angle of 60°; (b) Binary image of (a); (c) 2D-FT of (b).

As the number of hemispheres on surface increases, surface roughness gets bigger. The energy deposition induced by rough surface is the sum of energy deposition induced by every nanoparticle on surface in Fig. 6.4(a), and the coherent interference between nanoparticles. As Fig. 6.4(b) shows, the energy deposition by rough surface is as same as in Fig. 6.6(c) and 6.7(c) in the onset of central double crossed circles.

In summary, the exceptionally bright dots in Fig. 6.4(b) are due to the energy modulation induced by single nanoparticle on surface at an incident angle, which is an individual effect, involving the interference between incident wave and scattered wave. The

exceptionally bright dots represent the ripples parallel to the laser polarization with the periods close to the laser wavelength. The energy deposition induced by rough surface is mainly the sum of the individual effect of nanoparticles on surface. In addition, the coherent interference between nanoparticles may also play a role in energy modulation, which will be discussed in section 6.6.

6.3 Localized surface plasmons (LSP) and scattering electromagnetic wave (SEW)

In Sipe theory, radiation remnants are the electromagnetic field structures in the rough surface layer on semiconductor, which behave as a dipole sheet and take the place of the "surface-scattered wave" concept in phenomenological theories of ripple formation particularly for semiconductors. Radiation remnants have transverse and longitudinal polarization, so they are not classical radiation fields. However, radiation remnants satisfy the dispersion relations in air and underlying medium, so they are similar to radiation fields. However, the physical nature of radiation remnants was not clearly specified [SYP+83].

For metal, instead of radiation remnants as defined for semiconductor, the excitation of surface plasmon on rough surface plays an important role in the LIPSS formation in Sipe theory [SYP+83]. There are two types of surface plasmon, called as surface plasmon polariton and localized surface plasmon. Surface plasmon polaritons (SPP) are propagating, dispersive electromagnetic waves coupled to the electron plasma of a conductor at a dielectric interface. SPPs can be excited by phase-matching techniques. When light waves interact with metallic surfaces, the resulting electron density wave may propagate along the surface of the metal, defining a surface plasmon polariton. Owing to the strong frequency dependence of the metal complex permittivity, plasmons exhibit strong frequency dependence leading to surface plasmon resonances [Mai07].

On the other hand, localized surface plasmons (LSP) are non-propagating excitations of the conduction electrons of metallic nanostructures coupled to the electromagnetic field. LSP can be excited by direct light illumination [Mai07].

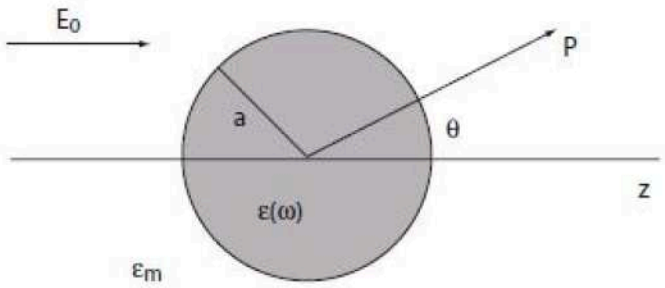

Figure 6.8: Drawing of a sphere placed in an electromagnetic field [Mai07].

When the laser irradiates a particle with sub-wavelength size in air or on the surface, scattering electromagnetic wave (SEW) is induced. SEW can be modeled by a dipole source model. LSP is coupled to the scattering electromagnetic wave. For example, Fig. 6.8 shows the case of a homogeneous, isotropic sphere of radius a with dielectric constant ε in the surrounding isotropic, non-absorbing medium with the medium dielectric constant ε_m (for medium air, ε_m=1). Radius a is in the range of sub-wavelength values. When the sphere is irradiated by the electric field E_0, the induced electric field E outside the sphere is represented by a dipole source located at the sphere center. The dipole moment p is represented by the formula:

$$p = 4\pi\varepsilon_0\varepsilon_m a^3 \frac{\varepsilon - \varepsilon_m}{\varepsilon + 2\varepsilon_m} E_0 \tag{6-10}$$

This formula shows that the dipole source experiences a resonant enhancement under the condition that $|\varepsilon+2\varepsilon_m|$ is a minimum. This resonance is called the localized surface plasmon (LSP) [Mai07]. In physics, the applied electromagnetic field induces an effective restoring force on the driven electrons on the surface, so that a resonance can arise, leading to field amplification both inside and in the near-field zone outside the metal sphere.

From another viewpoint of optics, the resonantly enhanced dipole source leads to the enhancement in the efficiency with which a metal nanoparticle scatters and absorbs light in the air, measured by extinction cross section C_{ext}, including scattering cross section C_{sca} and absorption cross section C_{abs}. The corresponding cross sections for scattering and absorption C_{sca} and C_{abs} can be calculated via the formulas [Mai07]:

$$C_{sca} = \frac{8\pi}{3} k^4 a^6 \left| \frac{\varepsilon - \varepsilon_m}{\varepsilon + 2\varepsilon_m} \right|^2 \tag{6-11}$$

$$C_{abs} = 4\pi k a^3 \, \mathrm{Im}\left[\frac{\varepsilon - \varepsilon_m}{\varepsilon + 2\varepsilon_m} \right] \tag{6-12}$$

$$C_{ext} = C_{sca} + C_{abs} \tag{6-13}$$

where $k=2\pi/\lambda$. From formula (6-13), the resonant wavelength of a silver sphere in the air is λ_{max}=400nm.

The resonant enhancement of polarization in LSP is dependent on the incident laser wavelength. The resonantly enhanced polarization in LSP can be measured by scattering cross sections in far field. In order to investigate the effect of LSP, 3D-FDTD simulations on the scattering cross sections of single Ag sphere in the air or an Ag hemisphere on the flat Ag surface are carried out. In the simulation model, both the sphere and hemisphere have the same radius of 50 nm. The incident plane wave propagates along Z axis and has the wavelength range of 300 nm-1200 nm. The wave polarization is in the X axis. The sphere center is at coordinate origin. The amplitude of electric field in the plane wave is set to 1V/m. Simulation time is set to be enough for the wave propagation in all the simulation space. Total-field scattered-field (TFSF) method is used to analyze the scattered field. Ag Drude model is built based on the tabulated data from Palik [Pal85]. The simulation results are shown in Fig. 6.9.

Fig. 6.9 shows that a single Ag sphere in air has the maximum scattering cross sections at 400 nm wavelength, while an Ag hemisphere on flat Ag surface has the maximum scattering cross sections at 363 nm wavelength, revealing that metal nanoparticles on the surface have similar LSP, in which the resonant frequency is close to the one of metal particles in air. Note that the resonant wavelength is related to nanoparticle size and shape [Mai07].

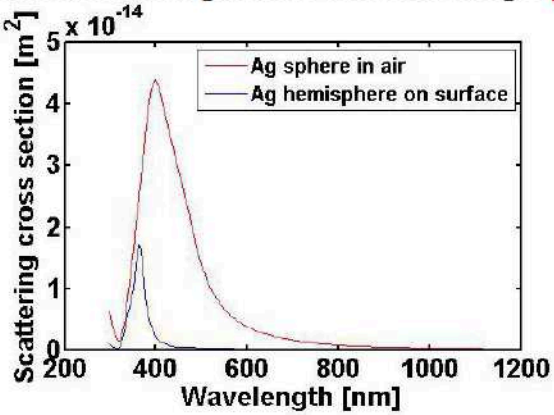

Figure 6.9: Extinction cross sections of single Ag hemisphere in air or on the flat Ag surface in the wavelength range of 300 nm-1200 nm.

In order to investigate the scattering characteristics of nanoparticles of different materials, 3D-FDTD simulations on the scattering cross sections of single hemisphere on the flat surface for three types of materials Ag, Ge and silica are carried out. In the

simulation model, all the hemispheres have the same radius of 50 nm. The dielectric functions of Ag, Ge and silica in unexcited state are built based on the tabulated data from Palik [Pal85]. Other simulation conditions are same as in Fig. 6.9. The simulation results are shown in Fig. 6.10.

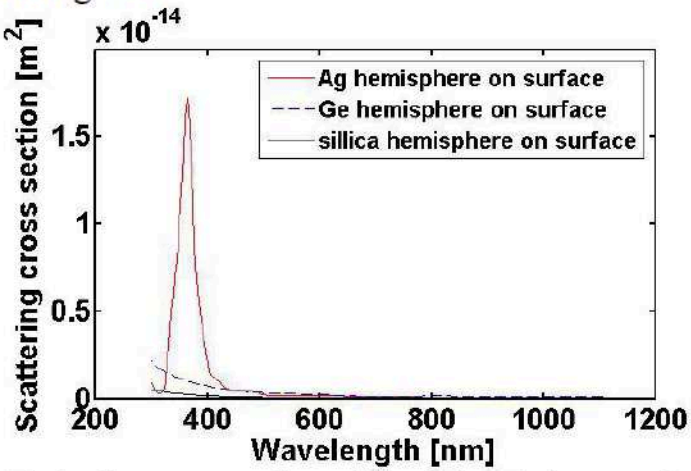

Figure 6.10: Extinction cross sections of single hemisphere on the flat surface in the wavelength range of 300nm-1200nm, for three types of materials: Ag, Ge and silica.

Fig. 6.10 shows that an Ag hemisphere on flat Ag surface has the resonant enhancement in scattering at the 363 nm wavelength, however, both the Ge and silica hemispheres have an increasing scattering cross sections with the decreasing wavelength, without the resonant enhancement at the given frequency range. Fig. 6.10 reveals that metal nanoparticles on the surface have much stronger scattering enhancement than both semiconductor and dielectric nanoparticles, because of LSP on metal.

In summary, metal nanoparticles on the surface have strong scattering enhancement originating from LSP, in which the resonant frequency is close to the one of metal particles in air.

For LIPSS formation, Sipe model indicates the necessary involvement of a surface wave. The nature of this wave can imply several options, such as diffracted waves with evanescent components [GA06] or surface plasmon polaritons (SPP). It will be argued in the following that, if the SPP wave has a role, it is not a necessary and sufficient condition to the development of LIPSS. We will point out to the surface topography and the presence of nanoparticles(nanoprotuberances) or nanoholes. We will focus first on a single nanoparticle effect and we will show that in the scattering characteristics, the role of LSP is inherently present.

6.4 The roles of micro/ nano- structures in LIPSS formation

Motivated by the features of lack crystallites, grain boundaries and dislocations, we focused on Zr-BMG $Zr_{44}Ti_{11}Cu_{10}Ni_{10}Be_{25}$ (at%) as the investigated material in the initial LIPSS formation steps from a topological and compositional viewpoint.

6.4.1 Micro/ nano- structures during LIPSS formation on Zr-BMG

The experiments of LIPSS formation on Zr-BMG have been introduced in Section 5.1.5. We follow first the topology changes upon the accumulation of first incident pulses in Fig. 5.10, which shows LSFL with the periodicity of 730±40 nm formed by four consecutive linearly polarized laser pulses.

When the laser pulse energy is at the level of single-pulse ablation threshold, the first laser pulse can damage the surface in a localized inhomogeneous manner at the sites of intrinsic surface defects or induce local nucleation of phase transformations [IZA15]. Therefore nanostructures on the surface appear in a dominantly random manner, as seen in Fig. 5.10(a1). The ablative features follow generally the main characteristic of an ultrafast ablation process with rapid, quasi-isochoric heating, build-up of temperature and pressure gradients and thermo-mechanical relaxation with thermodynamic evolutions below or beyond the critical point [CCA+12]. The main consequence is the onset of nanoscale surface structures.

We follow below potential sources and geometries of field interference at the surface.

6.4.2 Energy modulation induced by single surface nanostructure

In order to investigate the effect of surface nanostructures in LIPSS formation scenarios, we first analyze the energy modulation induced by single surface nanostructure using FDTD simulations. Then, the space period and patterns of energy modulation are evaluated, equally considering the interaction with the incident field. To assess conductor and isolator roles and emphasize their specific scattering features, simulations were carried on Zr-based BMG and

dielectric material silica glass models. Finally, near-field enhancement of localized surface plasmon is discussed.

The FDTD method is used to compute the inhomogeneous electric field distribution on the surface in the presence of a single scatterer. Effects of single hemisphere form placed on planar surface of BMG are analyzed. The surface is irradiated at normal incidence in air with linearly polarized laser pulses of 50 fs duration FWHM at 800 nm central wavelength. In the model geometry in Fig. 6.11(a), a hemisphere with the radius of 0.1 μm is located in the coordinate origin. BMG planar surface is at Z=0. The incident plane wave propagates in Z axis from the source plane. The laser polarization is along X axis. The amplitude of laser pulse is set to 1 V/m. Because dielectric constants of Zr-based BMG change little during the laser pulse duration of 50 fs at low laser fluence and the linear response is investigated, the refractive index of $Zr_{44}Ti_{11}Cu_{10}Ni_{10}Be_{25}$ is kept constant at the level of $\tilde{n}$=2.27+3.34i in FDTD simulation. Total-field scattered-field method is used to analyze the scattered field [AT02]. We recall that the polarization vector of the plane wave polarization is defined along E_x, and thus the electric field E_x quasi-represents the total field. Coherent interactions including the incident field involve the X directions. Upon interaction, new developed electric field E_z components only include the scattered field.

The result in Fig. 6.11(b) shows the time-averaged E^2 around the BMG hemisphere placed on BMG planar surface for one pulse duration of 50 fs in the XOZ plane. The time-averaged quantity is equivalent to a stationary energy field distribution. The interference between scattered light and incident laser field takes place in the space between the source plane and the surface. The electric field energy distribution arranges stationarily in a regular interference pattern and the periodic energy modulation appears on the surface. The 1D-FFT of energy modulation on surface is given in the inset of Fig. 6.11(b), which shows that the spacing period is 727±20 nm. The period depends slightly on the geometry of the nanoparticle on surface.

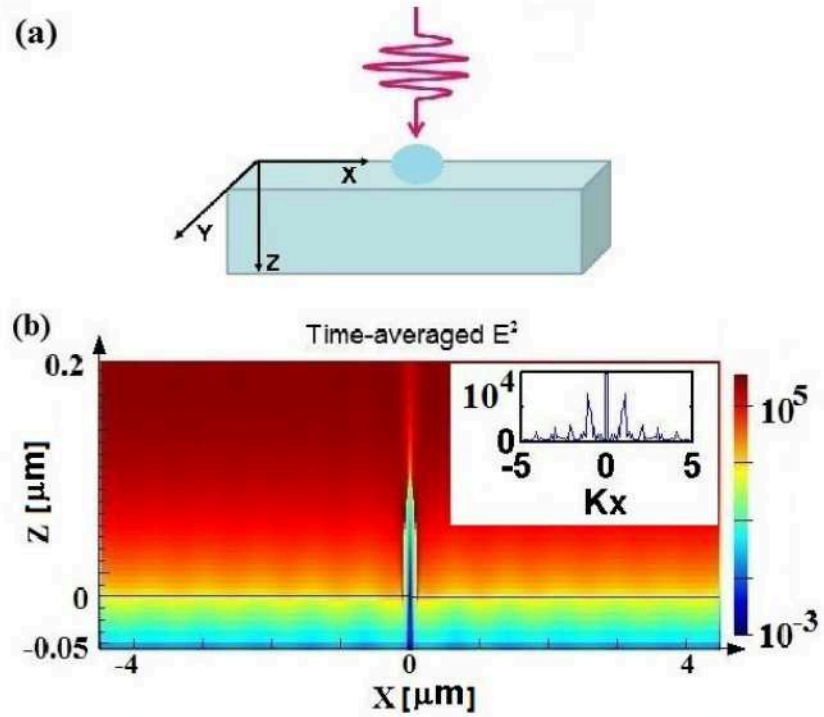

Figure 6.11: (a) Schematic geometry of interaction. (b) Time-averaged E^2 values determined by a BMG hemisphere (radius=0.1 μm) on the BMG surface in XOZ plane. 1D-FFT of E^2 values on surface is inserted in (b). A logarithmic color bar scale was used to emphasize the details. Note that X axis and Y axis are in different scales.

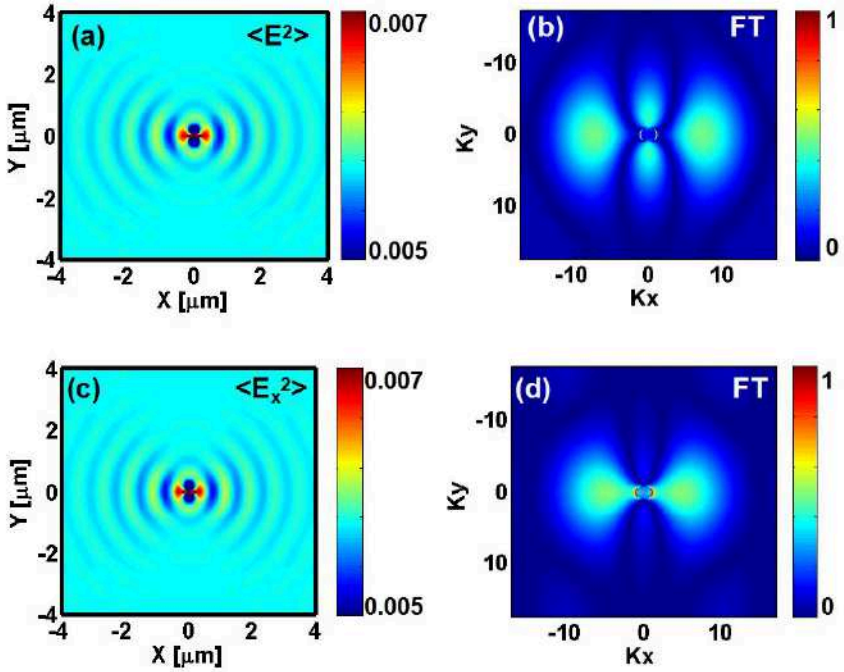

Figure 6.12: (a) Total energy distribution pattern on surface derived from stationary fields (time-averaged E^2) with (b) its Fourier decomposition. (c) Energy distribution of interferential terms pattern (time-averaged E_x^2) on surface with (d) its Fourier (FT) decomposition. Note that laser polarization is along X axis. Identical color bars are used for (b) and (d).

.

We will then focus on the scattering energy and field pattern for the case of a ϕ=100-nm hemisphere on the surface. Fig. 6.12(a) gives the time-averaged E^2 distribution on the surface equivalent to a stationary structured energy pattern. This shows that a main channel in the energy modulation comes from the near-field enhancement at the edge of nano-protuberance. At the same time a larger distance field modulation is observed, driven by scattering patterns and interference with the incident fields. FT analysis in Fig. 6.12(b) shows two main components in the spatial wave-vectors space ($K=2\pi/\lambda$ with λ=800 nm), a component oriented along the K_x axis (and thus corresponding to modulations perpendicular to the polarization axis) and a higher spatial frequency component along the K_y axis (with modulations parallel to the polarization). These are consistent with our previous research work [ZCL+15].

In order to analyze the origin of these modulations, we have verified the E_x^2 component (equivalent to a scalar energy value corresponding to the resulting field component in the vicinity of the surface containing the incident polarization) in Fig. 6.12(c, d). The interferential pattern shows similar amplitude and distributions as the total field, with a difference related to the higher frequency component along K_y (Fig. 6.12(d)). We conclude that the higher spatial frequency component has a mixed origin, scattering in a characteristic pattern and potential interferential interactions along the polarization direction.

To assess conductor and isolator roles and emphasize their specific scattering features, the energy modulation on two materials: Zr-based BMG and silica glass are analyzed by FDTD simulations respectively. The energy modulations are induced by metallic and dielectric scattering centers, equivalent to protuberances and nanoholes in the surface. The same hemisphere model as in Fig. 6.12 is used in 3D-FDTD simulation. To emphasize the linear response, the dielectric constants of silica in non-excited state are chosen. In FDTD simulation, the refractive index of silica glass is $\tilde{n}$=1.45+0i under 800nm-wavelength irradiation.

As the size of the surface nanostructure is comparable to the wavelength of the laser, the scattering light can be associated with Mie scattering, but we observe here a general scattering and interference phenomenon involving incident and scattered fields. The results are analyzed and shown in Fig. 6.13 in terms of surface pattern distribution and field diffusion patterns.

Time-averaged E^2 distributing on surface in XOY plane for the case of BMG material illuminated by 800-nm plane wave is given in Fig. 6.13(a). This shows a stationary spatially modulated pattern.

Time-averaged electric field magnitude E^2 distribution is ripple-like shaped along the polarization direction and the spacing period is 727±20 nm. It is now of interest to observe the near-field diffusion pattern. Fig. 6.13(c) shows the peak electric fields E_z in the XOZ plane. We note that maximum E_z is 1.25, higher than the incident laser field magnitude, indicating an enhancement mechanism. To verify to which extent this is related to the material properties, particularly to the conductive characteristics which may enable collective charge oscillations or to the geometry, we verify the situation in case of a dielectric medium. Fig. 6.13(b) shows time-averaged E^2 distribution on surface in the XOY plane for a silica hemisphere of same size located on silica material and excited by a planewave. Time-averaged E^2 distribution is a mix of patterns with two periodicities given by fields above and below surface, the central spacing periods are 571 nm, 727 nm respectively. The period of 571 nm is related to interference between the refractive wave in silica glass and scattered light. The period of 727 nm is related to interference between incident plane wave and scattered light on the top of the surface. We thus observe space period and pattern of energy modulation dependent on substrate materials. Fig. 6.13(d) shows electric fields E_z in XOZ plane. The maximum E_z is 0.25 in this case.

For comparison with hemispheres on surface, the energy modulations by nanoscale air holes on BMG and silica are also investigated by 3D-FDTD simulation. In the same model conditions as in Fig. 6.13(a) and (b), instead of a hemisphere, an air sphere is considered, that has the radius of 0.1 μm and its center placed on the surface and the results are given in Fig. 6.13(e, f). Fig. 6.13(e) gives time-averaged E^2 in the XOY plane for a hole on BMG, which shows the same pattern as in Fig. 6.13(a). Fig. 6.13 (f) shows time-averaged E^2 in the XOY plane for a hole on silica, which shows the same pattern as in Fig. 6.13 (b). We may conclude that the nanoscale particles or holes on surface play the same role in energy modulation on surface induced by interference between incident laser and scattered light.

Note that the maximum E_z in metal BMG is stronger than the maximum E_z in dielectric material silica glass, as seen in Fig. 6.13(c, d). Such near-field enhancement can likely involve localized surface plasmons (LSP) on metal, namely non-propagating conduction electronic oscillations coupled to the electromagnetic field [Mai07]. LSP are typical product of light excitation of small structure with free mobile electrons and resonant excitation can determine locally field amplification.

The characteristic patterns in Fig. 6.13(a) and near-field enhancement in Fig. 6.13(b) represent potential evidence that LSP excitation occurs on the BMG hemisphere under laser irradiation. LSP enhances the electric field in the near-field zone of BMG hemisphere surface, amplifying thus the yield of scattered light and influencing the energy modulation on surface.

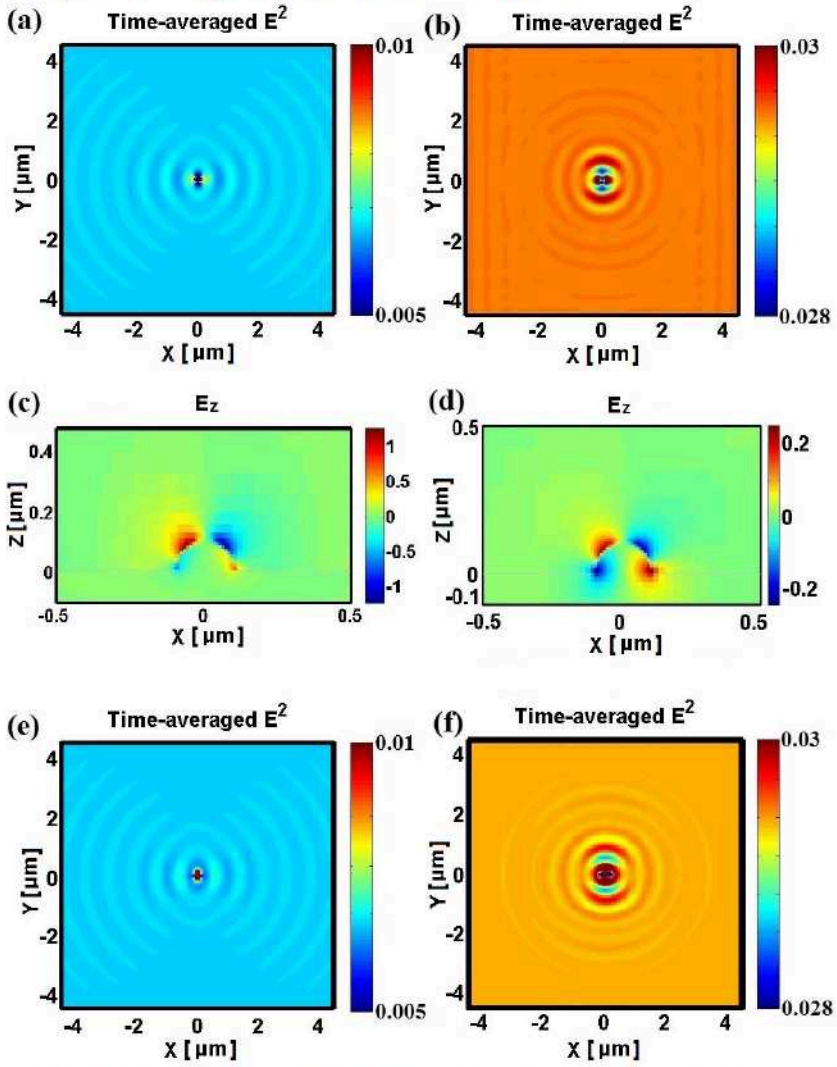

Figure 6.13: (a) Time-averaged E^2 in XOY plane for a hemisphere (radius=0.1 µm) on BMG; (b) Time-averaged E^2 in XOY plane for a hemisphere on silica; (c) Maximum electric field Ez in XOZ plane for a hemisphere on BMG; (d) Maximum electric field Ez in XOZ plane for a hemisphere on silica. (e) Time-averaged E^2 in XOY plane for a hole on BMG, (f) Time-averaged E^2 in XOY plane for a hole on silica.

6.4.3 LSFL formation from multiple scattering centers

Based on the results on single scattering centers, we can discuss field diffusion impact on low spatial frequency LIPSS formation. The N-pulse dependence of the surface topology upon irradiation indicates cumulative effects that can be resumed as follows. When a

few pulses impact on a flat metal surface with low roughness, the sub-wavelength surface structures will be generated, such as nanoscale hemispheres and nanoscale holes. The origin of these structures can be associated with inhomogeneous distribution of phase-transition nucleation centers [AIZ12]. A sub-wavelength surface metallic structure upon irradiation can scatter light assisted by potentially excited LSPs and act as a dipole source. An interference phenomenon between the incident field and the scattered field occurs, with the onset of regular patters at the typical wavelength of ripples. The modulated energy deposition can thus contribute to generation of LIPSS.

In order to evaluate the interaction between multiple dipole sources, cases including two and multiple BMG hemispheres on a planar surface are analyzed by FDTD simulations. In the simulation models, BMG hemispheres on planar surface have the same radius of 0.1 μm. The incident plane wave with 800 nm wavelength propagates along the Z axis, and the polarization lays parallel to the X axis. Simulation results are shown in Fig. 6.14 and Fig. 6.15.

Fig. 6.14(a) shows the time-averaged E^2 distribution induced by two hemispheres separated by a distance of 4 μm. We observe already the superposition of the two individual patterns, leading to the onset of quasi-parallel periodically aligned traces at the intersection point. As the electric field of the incident plane wave is defined in the X-axis: E_x, the electric field E_z components only come from the scattered field. The electric field magnitude E includes three components: E_x, E_y and E_z and we discuss the stationary patterns associated with each of the component via the time-averaged squared component of the field, artificially assimilated to an energy-like component. Fig. 6.14(b) shows the time-averaged E_x^2 distribution, which is similar to Fig. 6.14(a). Fig. 6.14(c) shows the time-averaged E_z^2 distribution with a space period of about 400 nm, which derives from the coherent interaction between two scattering sources, as it will be justified below. Interference effects between incident wave and scattered wave are maximized in the x component, while z component is only originating from scattering.

In order to prove the nature of coherent effects in E_z distribution without involving interaction with the incident wave (given the polarization direction, the interferential action of the incident field does not occur along Z which contains only scattered artefacts), FDTD simulation of the interaction between 2 dipole sources in the absence of the incident plane wave is performed. In this model, two dipole sources with distance of 4 μm are located on the BMG surface

as shown in Fig. 6.14(d). Both the dipole sources have the electric field amplitude of 1 V/m, the wavelength of 800 nm, the pulse period of 50 fs and the polarization along the X axis. Fig. 6.14 (d) shows the time-averaged E^2 distribution induced by the two coherent dipole sources, which is similar to Fig. 6.14(c) in both shape and space period. So the time-averaged E_z^2 distribution arrives from the coherent interaction between two scattering sources, and shows a different periodicity than expected in low spatial frequency LIPSS. In addition, the value of time-averaged E_z^2 is much lower than E_x^2, so the coherent interference between scattering sources doesn't play an important role in initial LIPSS formation in our case, a situation that may evolve as a function of scatterer concentration. The energy distribution pattern defining the regular ripples comes mainly from the interference between scattering wave and the incident laser. Comparing Fig. 6.14(a) with 6.14(b) and 6.14(c), we conclude that the energy modulation induced by two nanostructures comes from the interference between scattered light and incident plane wave, and also from the coherent interaction between all scattered sources, however, the interference between scattered light and incident plane wave plays a primary role in this case.

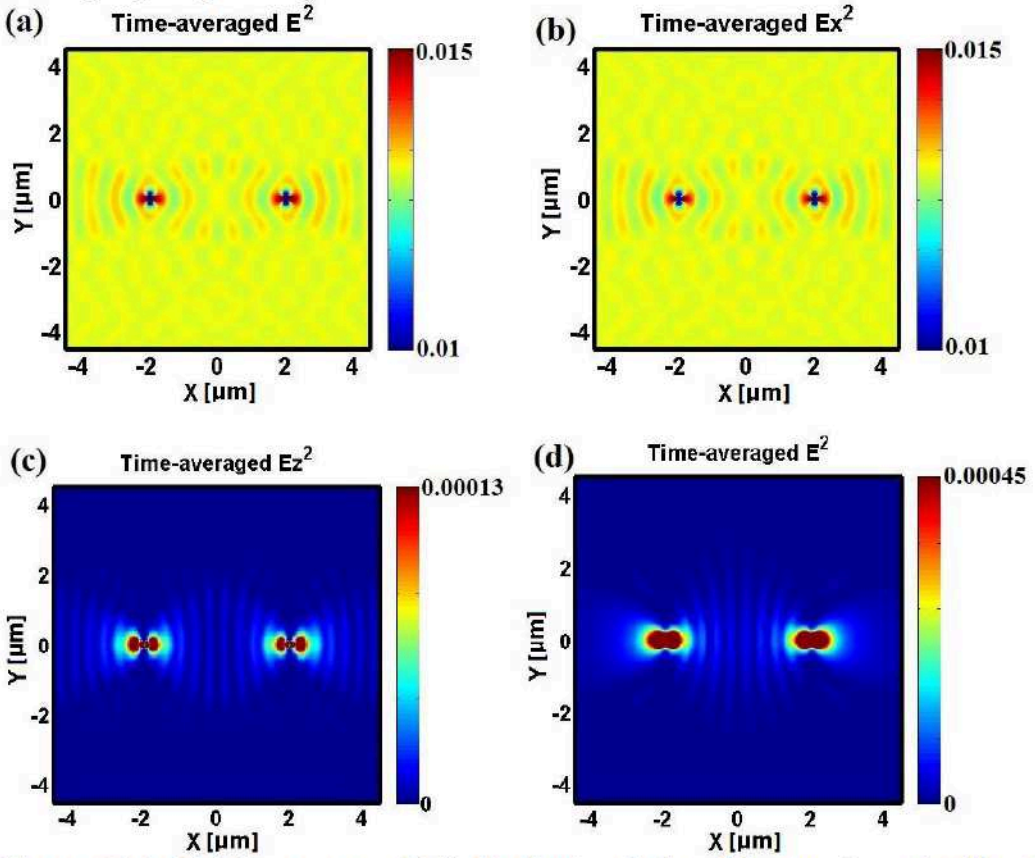

Figure 6.14: (a) Time-averaged E^2 distribution induced by two laser-irradiated hemispheres (radius=0.1 μm) separated by the distance of 4 μm; (b) Time-averaged Ex^2 distribution; (c) Time-averaged Ez^2 distribution; (d)

Time-averaged E^2 distribution induced by the mutual interaction of two coherent dipole sources with the distance of 4 μm.

In order to simulate the rough surface induced by a few laser pulses, the flat surface with 1000 cubic nanoparticles in random distribution on the surface is built for the FDTD simulation model [SRO+12]. The cubic particle size is 40 nm ×40 nm×40 nm. The surface size is 25 μm×25 μm. The incident plane wave propagates along the Z axis. It has the wavelength of 800 nm and the polarization aligned along the X axis.

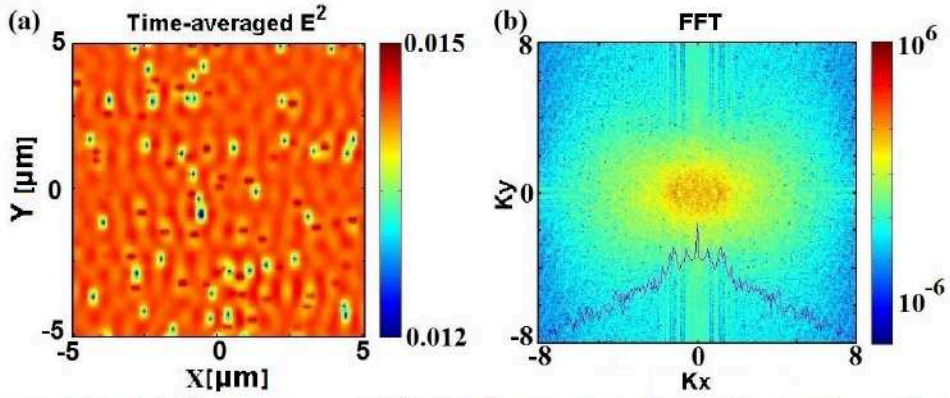

Figure 6.15: (a) Time-averaged E^2 distribution just above the rough surface for an ensemble of scatterers. (b) 2D-FFT of the intensity distribution in (a), the values along Ky=0 is shown at the bottom of Fig. 6.15(b). A logarithmic color bar is used to emphasize the details.

Fig. 6.15 shows the time-averaged E^2 just above the rough surface, and the energy modulation can be seen at this level. The energy on the surface is modulated with a pattern similar to the typical ripples, as shown in Fig. 6.15(a). Fig. 6.15(b) shows the 2D-FFT of the Fig. 6.15 (a), from which the energy modulation distribution has the space period of 769±20 nm with the direction perpendicular to the laser polarization. The theoretical results agree reasonably well with that of the experiments considering that no feedback issues are considered here.

Even though FDTD is not specific to the modulation source, several points can be emphasized. The field enhancement around metallic nanostructures points to a potential LSP involvement. The optical indices can allow SPPs propagation and Composite Diffractive Evanescent Wave (CDEW) can be excited on the Zr-based BMG [GA06, LM7]. However a general scattering and interference model is sufficient to indicate optical modulation on the surface.

6.5 Role of one-dimensional nano/microstructure and topography defects in LIPSS formation

The presence of defects and their role in scattering laser radiation was largely discussed in the literature (with a recent approach in references [MTA+14, MTA+13]) and used as an argument for the involvement of a scattered field. For example, a defect line remarkably changed the direction of a few LSFL ripples near the defect in Fig. 5.8(c). The relation between the geometry of the defect and the laser vectorial field is complex and we observe this relation on the multi-alloy CMSX-4.

6.5.1 Laser pulse exposure with fixed polarization direction

With the intention to study the role of a defect line in Fig. 5.8(c) in LIPSS formation, a sub-micron-sized groove was made on the flat CMSX-4 sample by a mechanical scratch. The AFM image of the groove is shown in Fig. 6.16(a). Fig. 6.16 (b) shows the cross-section size of the groove from AFM. The groove has 600 nm in width, 40 nm in depth and two ridges with height of 75 nm, 150 nm, respectively.

To grasp the features of the interaction between sub-micron-sized groove and laser, the groove is exposed by successive sequences of fs laser pulses at the same laser polarization and with a fluence above the modification threshold. The laser polarization forms an angle of 67.62° with the groove. The time delay between two successive shots is about 1 second. The laser fluence is 1.15 J•cm^{-2}. Fig. 6.16(a) shows the AFM images of the groove irradiated by N=1 pulse, N=2 pulses and N=4 pulses respectively in relation to the topology of the non-irradiated spot. After N=1 pulse, ripples are produced at both sides of the groove, albeit with a large periodicity. With increasing number of pulses the period stabilizes at a slightly subwavelength value, and interestingly, the ripple pattern gradually grows further away from the groove.

We discuss below the pattern evolution. Fig. 6.16(b) shows the cross-section profile of the not irradiated groove. Fig. 6.16(c) shows the cross-section profile of the groove after N=1 pulse. After the first pulse, the ridges of the groove were etched away and the height of the ridges was decreased. Fig. 6.16(d) shows the cross-section profile of groove after N=2 pulses. Now ripples are produced at both sides of the groove and one ripple was produced in the valley within

the groove after N=2 pulses. As the pulse number increases to N=4, the pattern extends spatially with more ripples being produced further away from the ridges as seen in Fig. 6.16(e). The prominent rippled-structure produced in the valley of the groove can be explained assuming localized near-field effects. Localized near-field energy modulation can appear in the scattering pattern around the metal peaks of the ridges leading to an electric field enhancement. A potential involvement of localized surface plasmons (LSP) can contribute to the near-field energy modulation, with plasmonic near-field enhancement [San13, DZP+13, HSR+14, LM07], resulting in two new grooves near ridges in the valley.

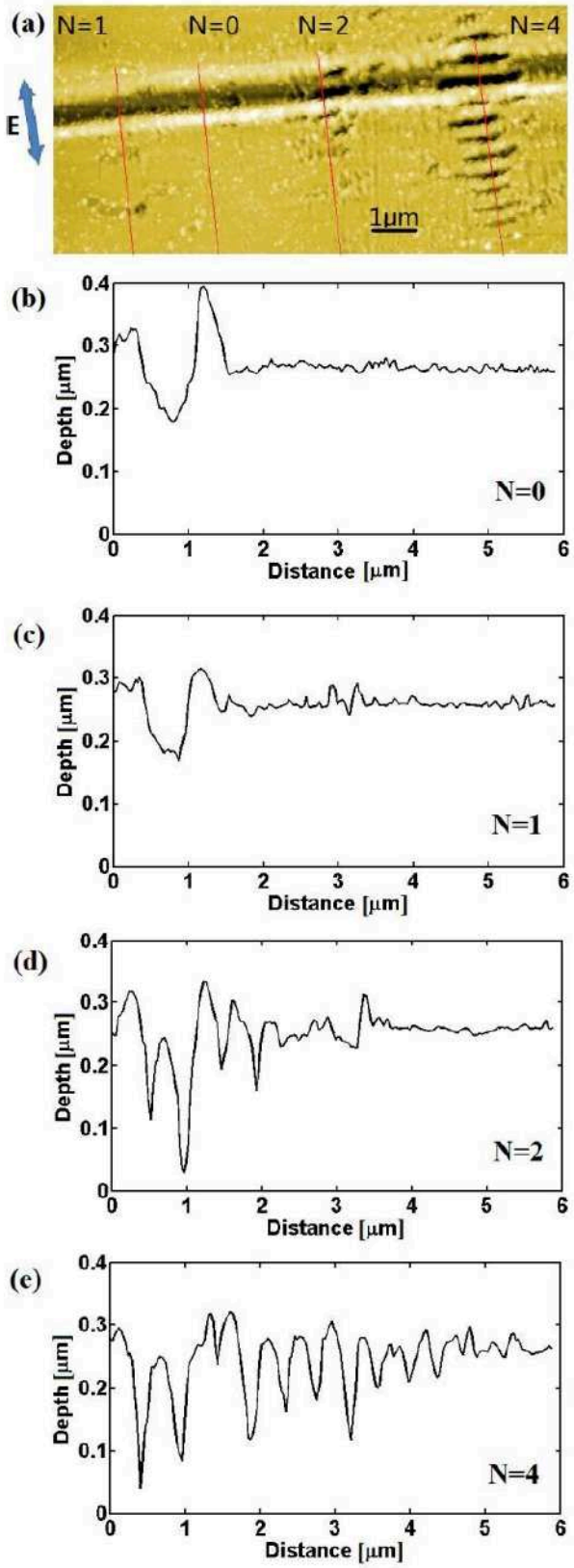

Figure 6.16: (a) AFM image of the groove shot by N=1, 2, and 4 pulses. The laser polarization is indicated by the double-arrow in (a) and the laser fluence is 1.15 J/cm^2; (b-e) cross-section profiles of groove: (b) not irradiated; (c) after N=1 pulse; (d) after N=2 pulses; (e) after N=4 pulses.

6.5.2 Effect of varying polarization direction along the groove

In order to study the effect of fs laser polarization in the presence of defects of anisotropic geometries, the groove is now irradiated by N=4 fs laser pulse sequences with different laser polarizations. The delay between two successive shots was about 1 second. The laser energy is 1.15 J·cm^{-2}. Fig. 6.17 shows SEM images of the groove shot by N=4 pulses employing three polarization directions.

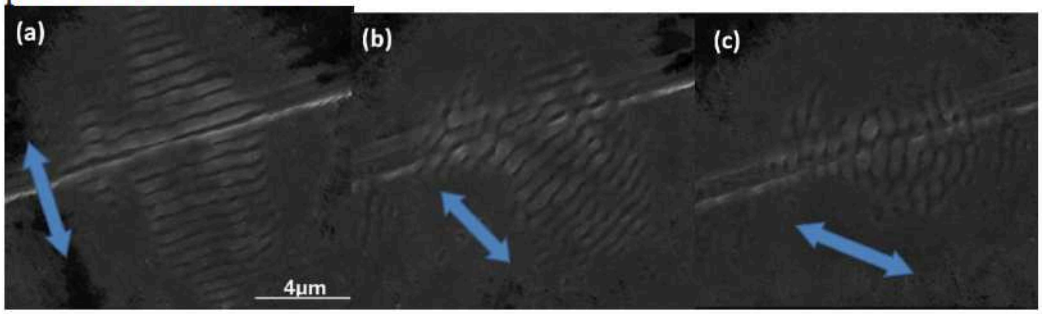

Figure 6.17: SEM photos of the groove shot by N=4 pulses, the angles between linear polarization and groove are the following: (a) 82.38°, (b) 52.38°, (c) 22.38°.Laser polarization axis is shown as double-arrow and laser fluence is 1.15 J • cm^{-2}.

In Fig. 6.17(a), the laser polarization is quasi-perpendicular to the groove, making an angle of 82.38° with the groove axis. In this case ripples are mainly parallel to the groove and distributed in triangle-like shape at two sides of the groove. In Fig. 6.17(b), laser polarization has the angle of 52.38° with groove axis. Some ripples near the groove are distributed parallel to the groove. However, ripples located away from the groove are oriented perpendicular to the laser polarization. In Fig. 6.17(c), laser polarization has the angle of 22.38° with the groove axis and ripples are distributed mainly perpendicular to the laser polarization, however, some ripples in the groove are perpendicular to the groove. This indicates that in the vicinity of the groove the field has a complex structure that need to be elucidated. Typically ripple formation is the related to deposited energy on surface as ablative or phase transition processes are involved. In order to investigate the effect of linear-geometry defects in LIPSS formation, energy modulation is analyzed by FDTD simulations.

6.5.3 FDTD simulations on the effect of a linear groove

FDTD method is used to compute the electric field distribution near the groove. The groove model is built based on the size obtained from Fig. 6.16(b). The refractive index of CMSX-4 is 2.05+4.24i in the model, corresponding to the cold material. The groove is irradiated at normal incidence in air with linearly polarized laser pulses. The laser pulse is modeled with a 50-fs pulse duration FWHM at the wavelength of 800 nm. For convenience, as we are interested in the spatial repartition of energy and in a linear regime, the magnitude of input laser electric field is set to 1 V/m allowing direct observation of field concentration effects with respect to the input. Convolutional perfectly matched layer method is used as absorbing boundary condition.

In order to investigate the effect of polarization in Fig. 6.17, FDTD simulations are performed for one groove with sub-micron section under irradiation with different laser polarizations. For simplicity, a long rectangular hole on the alloy surface is chosen as the groove model. The modeled groove has the width of 600 nm and the depth of 80 nm in a rectangle cross section. In FDTD model, the groove is aligned along the Y axis in the XOY plane and a Gaussian laser beam is used now to give an idea about the dimensional size of the affected area. The incident laser beam propagates along Z axis. The magnitude of laser electric field is set to 1 V/m. The simulation results in different polarization are shown in Fig. 6.18.

Fig. 6.18 shows time-averaged electric field energy E^2 on the surface induced by laser pulses with different polarizations. In Fig. 6.18(a), under a laser polarization perpendicular to the groove, energy modulation outside of the groove is parallel to the groove and distributed in two triangular domains, which are similar to the triangle-like distribution of ripples in Fig. 6.17(a). As the angle between the groove and laser polarization decreases gradually from 90° to 60°, 30° and 0°, energy modulation outside of the groove also decreases gradually (Fig. 6.18(b-c)). The responsible factor is related to the fact that the groove can induce a scattered surface wave propagating perpendicular to the groove, which interferes with the incident laser field, leading to energy modulation parallel to the groove. The scattered surface wave pattern is dependent on the angle between the groove and laser polarization, as only the component of the incident laser with polarization perpendicular to the groove can induce the scattered surface wave. Therefore, as the angle between the groove and laser polarization decreases gradually, the scattered surface wave magnitude decreases as well, hence the energy

modulation perpendicular to the groove decreases. This explains the evolution of the ripples parallel to the groove in Fig. 6.17.

In Fig. 6.17(b) when the groove and polarization are moderately deviating from orthogonality, there are remarkably two different LSFL ripple directions: parallel to groove and perpendicular to laser polarization. The ripples perpendicular to laser polarization can be explained by invoking the interference between incident laser and scattered surface wave induced by surface roughness. The ripples parallel to groove can be explained by the interference between incident laser and scattered surface wave induced by the groove. In Fig. 6.17(a), under a laser polarization perpendicular to the groove, scattered surface waves parallel to groove are excited, mostly by the groove anisotropic topography. Laser polarization is also parallel to the normal vector of the groove, so both laser polarization and scattered surface wave induced by groove contribute to the appearance of ripples in Fig. 6.17(a). In Fig. 6.17(b), laser polarization makes the angle of 52.38° with the groove and scattered surface wave parallel to groove weakens, leading to only few ripples near the groove that are parallel to the groove, however, ripple direction in the zone away from groove is determined by laser polarization [YPD+83, SYP+83]. In Fig. 6.17(c), laser polarization has the angle of 22.38° with the groove, scattered surface wave parallel to groove is too weak for ripple formation, so ripple direction is mainly determined by laser polarization. Remarkably, a few ripples in the groove are perpendicular to the groove, which will be discussed in the following.

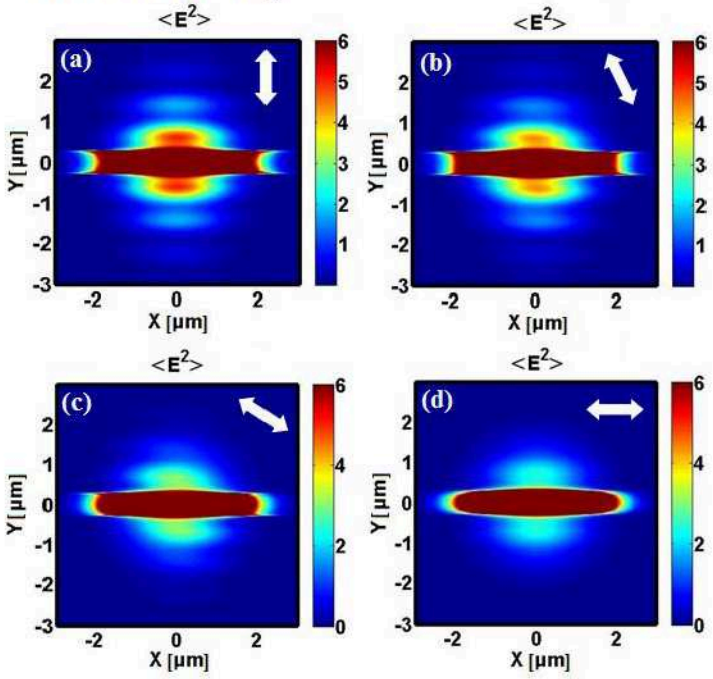

Figure 6.18: Time-averaged electric field energy E^2 on surface induced by (a) 90° polarized laser pulse; (b) 60° polarized laser pulse; (c) 30° polarized laser; (d) 0 ° polarized laser pulse. The laser polarization is indicated with a double-headed arrow.

The question of reorientation of ripples in the groove could be easily understood assuming the existence of defects in the groove. The transverse ripples perpendicular to the groove in Fig. 6.17(c) could therefore be explained by scattered waves in the groove induced by large holes across two ridges of the groove. It is presumable that some nanoholes form at the ridges, with the first pulse induced ablation. After a few pulses, the holes at ridges become larger and deeper. When the large holes are across the two ridges, scattered wave in the groove appear. The groove model with two nanoholes across ridges is used for FDTD simulation, as shown in Fig. 6.19(a). The laser polarization has the angle of 22.38° with the groove. The simulation result is shown in Fig. 6.19 (b).

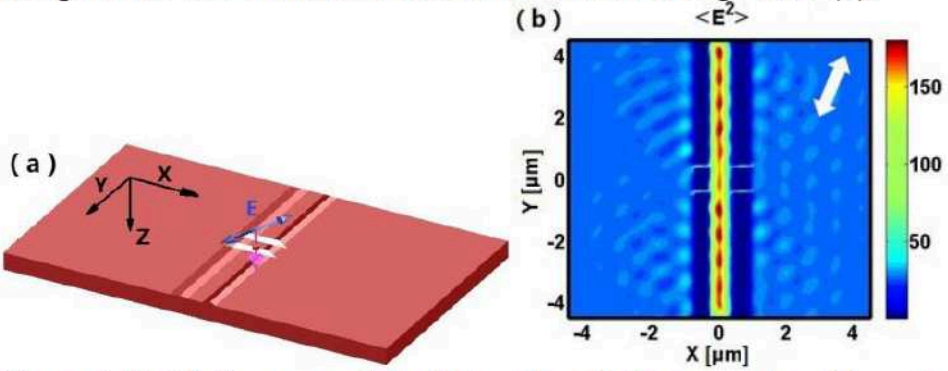

Figure 6.19: (a) Groove model with two large holes across two ridges, two holes are shown in white color; (b) Time-averaged electric field energy E^2 on surface in XOY plane. The laser polarization is indicated with a double-headed arrow.

Fig. 6.19(b) shows time-averaged electric field energy E^2 on surface. Besides the reorientation of ripple patterns outside the groove, we note an observable periodic energy modulation in the groove. The interference between the incident laser and scattered wave in the groove results in the formation of transverse ripples inside the groove. Transverse ripples in the groove could be explained by scattered wave in the groove, which is induced by holes at the ridges.

We observe therefore that the scattered wave induced by nanostructure plays an important role in LIPSS formation, which is consistent with the conclusion in references [MTA+14, MTA+13]. In addition to the case of single-pulse ablation in references [MTA+14, MTA+13], multi-pulse ablation is the feedback process between light and nanostructures. Laser ablation can produce new surface

nanostructures, at the same time, new nanostructures induce different scattered surface wave, leading to a new feedback-driven energy modulation deposited on surface. Therefore ripple formation in multi-pulses is a result of the feedback process between light and nanostructures involving a dynamic evolution in the scattering pattern.

6.6 FDTD simulation for HSFL formation

High-spatial-frequency laser-induced periodic surface structures (HSFL) driven by incident ultrafast laser fields, with their ability to achieve structure resolutions below λ/2, have the potential application in the nano-machining. In Chapter 5, HSFL formations on CMSX-4 (Fig. 5.8) and Zr-CA (Fig. 5.10) have been observed. In this section, the origins of HSFL on CMSX-4 and Zr-CA are investigated respectively in the following.

6.6.1 HSFL(⊥E) on CMSX-4

In order to simulate the rough surface induced by a few laser pulses, the flat surface with 1000 cubic nanoparticles in random distribution on the surface is built as the 3D-FDTD simulation model [SRO+12, SRH+10]. The cubic particle size is 50 nm×50 nm×40 nm. The surface size is 25 μm×25 μm. The incident plane wave propagates along the Z axis. It has the wavelength of 800 nm and the polarization along the X axis.

Fig. 6.20(a) shows the time-integrated square field E^2 standing as an average intensity value for whole pulse duration just below the rough surface. This shows that a standing energy pattern was formed. The energy on the surface is therefore spatially modulated. Fig. 6.20(b) shows the 2D-FFT of the Fig. 6.20(a), from which the energy modulation distribution has the spatial period of 714-769.2 nm with the direction perpendicular to the laser polarization. Simulation results agree well with LSFL ripples in the experiment results in Fig. 5.8(c). In accordance with the precious discussion [LZC+15], it appears that potentially it is the interference between incident laser and scattered wave along the surface that mainly contributes to the energy modulation in Fig. 6.20(a) and which can produce the LSFL ripples perpendicular to laser polarization. Except the interference between incident laser and scattered wave, the interference between scattered sources also plays a role in energy modulation, discussed in the following.

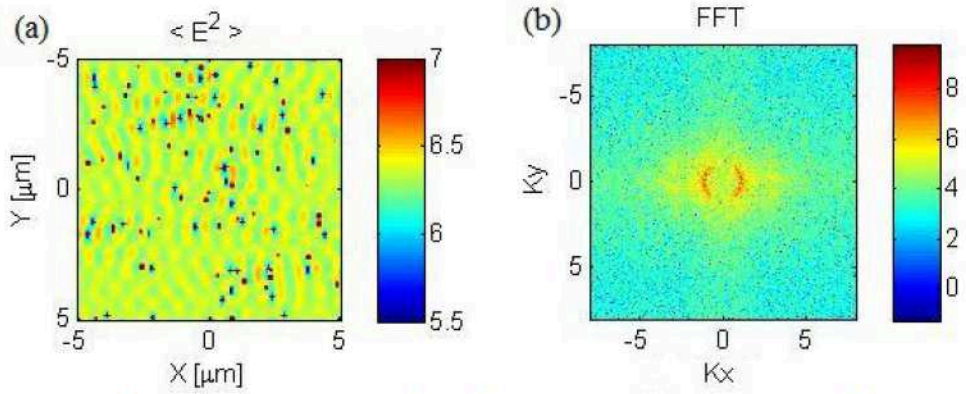

Figure 6.20: (a) Time-integrated E^2 distribution nearly or just below the rough surface. (b) 2D-FFT of the intensity distribution given in (a).

In order to evaluate further subtle effects in the interaction between surface scattered sources, an idealized and simplified model is used to evaluate the interaction in the presence of multiple scatterers. Two hemispheres placed on the planar surface of CMSX-4 illuminated by plane wave are analyzed by 3D-FDTD simulations. In the simulation model, CMSX-4 hemispheres on planar surface have the same radius of 0.1 µm. The incident plane wave propagates along the Z axis and the polarization direction is parallel to the X axis. As the electric field of incident plane wave is polarized along the X axis, only the electric field E_z component originates from the scattered field. Thus, the interference between the incident laser and scattered wave becomes visible in the electric field E_x while the interference between scattered sources can be seen in the electric field component E_z. As the energy stored in the electric field component E_y is much smaller than E_x and E_z cases, the electric field E_y distribution is not discussed in the following. Simulation results are shown in Fig. 6.21.

Fig. 6.21(a) shows the time-integrated E_x^2 distribution induced by two hemispheres separated by a distance of 4 µm, and energy modulation pattern has the periodicity of slightly smaller than 800 nm. The associated spatial energy modulation originates from the interference between incident laser and scattered waves, which, based on the pattern similarity, seem to contribute to LSFL ripple formation. At the same time, Fig. 6.21(b) shows the time-integrated E_z^2 distribution. This shows a space periodicity slightly smaller than 400 nm, which derives from the coherent interaction between two scattering sources (similar to the case of the interference of counter propagating beams giving fringes at $\lambda/2$). In Fig. 6.21(a), the amplitude of the base level of the time-averaged E_x^2 quantity is about 6 $V^2 \cdot m^{-2}$, the amplitude of inhomogeneous time-averaged E_x^2 is about 0.86 $V^2 \cdot m^{-2}$. As a comparison, the amplitude of

time-averaged E_z^2 is about 0.066 $V^2 \cdot m^{-2}$, much smaller than E_x^2. Consequently, when the particle inter-distance is large, the coherent interaction between two scattering sources plays a weak role. However, in the cases of short-range and assemble of nano-structures, the value of time-averaged E_z^2 can get significantly larger. In the same simulation condition, two hemispheres with radius of 0.1μm separated by the distance of 0.67 μm are analyzed in 3D-FDTD. Moreover, six same hemispheres separated by the distance of 0.67 μm are also analyzed. The simulation results are shown in Fig. 6.22.

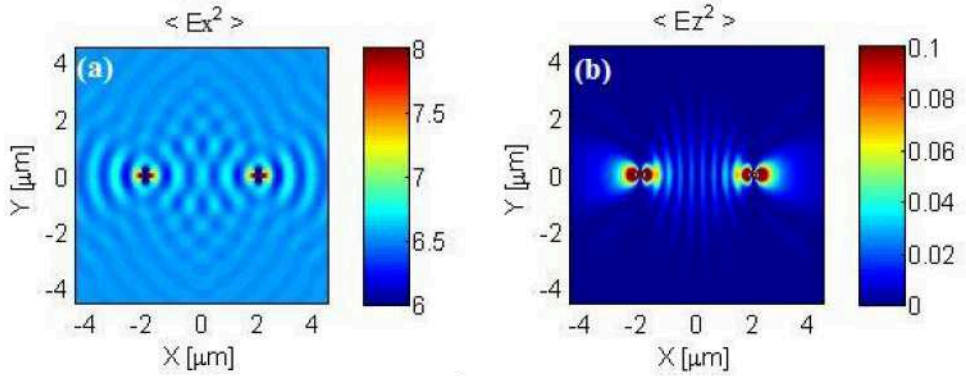

Figure 6.21: (a) Time-integrated E_x^2 distribution induced by two laser-irradiated hemispheres separated by the distance of 4 μm; (b) Time-integrated E_z^2 distribution; Note that the laser polarization is along X axis.

Fig. 6.22(a) shows the time-integrated E_z^2 distribution induced by two hemispheres separated by 0.67 μm and the amplitude of time-averaged E_z^2 is about 0.28 $V^2 \cdot m^{-2}$. Fig. 6.22(b) shows time-integrated E_z^2 distribution induced by six hemispheres separated by 0.67 um and the amplitude of time-averaged E_z^2 is about 0.5 $V^2 \cdot m^{-2}$. Compared with the value of 0.8 $V^2 \cdot m^{-2}$ in the amplitude of inhomogeneous time-averaged E_x^2, E_z^2 also contributes to the energy modulation. The spatial period of energy modulation pattern in Fig. 6.22(b) is about 360 nm as derived from FFT analysis, which is close to the period of HSFL ripples in Fig. 5.8(c). This implies that the coherent interaction between two scattering sources may play an important role in energy modulation in the cases of short-range and assemble of nano-structures. This is a factor that can equally intervene in the formation of HSFL ripples with direction perpendicular to laser polarization.

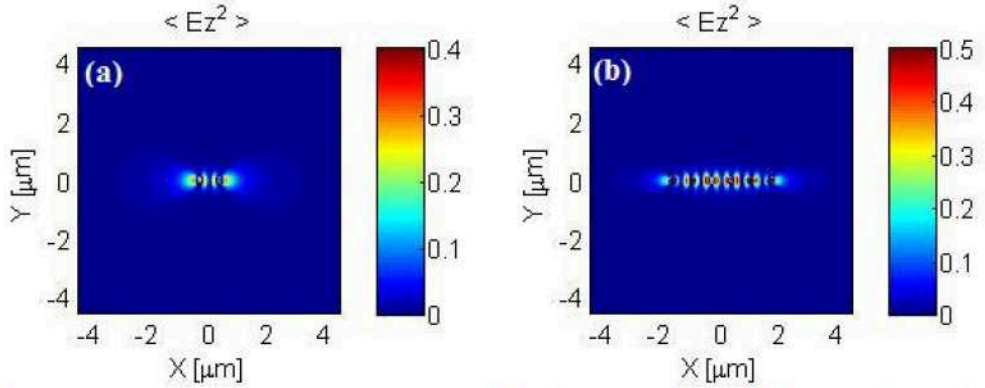

Figure 6.22: (a) Time-integrated Ez^2 distribution induced by two hemispheres separated by the distance of 0.67 µm; (b) Time-integrated Ez2 distribution induced by six hemispheres separated by the distance of 0.67 µm.

In order to investigate the formation of HSFL ripples perpendicular to laser polarization, the rough surface model is built according to the SEM data in Fig. 5.8(c) and the depth of rough surface is set to 100 nm in the 3D-FDTD model. In the same simulation conditions as in Fig. 6.20, FDTD simulation results are given in Fig. 6.23. Fig. 6.23(a) shows the time-integrated E_x^2 distribution, which has the space periodicity of 692 nm. At the same time, Fig. 6.23(b) shows the time-integrated E_z^2 scattering distribution. This indicates a space periodicity of 375 nm, which contributes to the formation of HSFL ripples in Fig. 5.8(d).

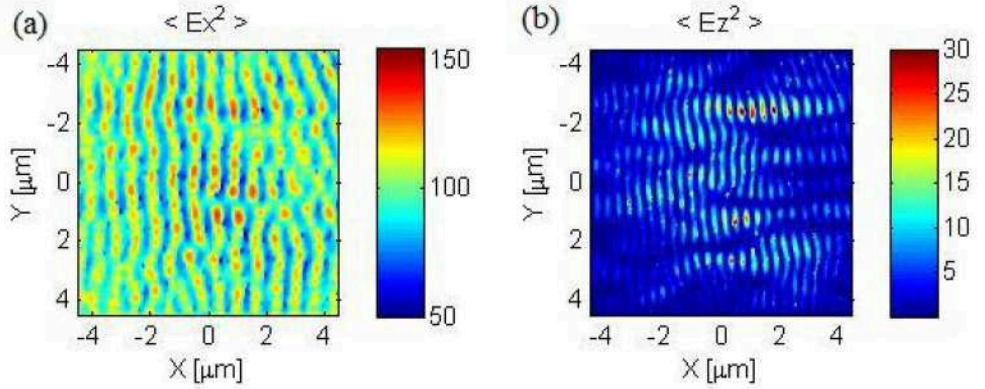

Figure 6.23: Time-averaged electric field energy distribution induced by rough surface from figure 5.8(c): (a) Time-integrated Ex^2 distribution; (b) Time-integrated Ez^2 distribution.

In summary, HSFL ($\perp$E) with the spatial periods close to the half of the LSFL periods can be explained by the coherent interaction between scattering sources in the cases of short-range and assemble of nano-structures from rough surface.

6.6.2 HSFL (∥E) on CA

As LIPSS experiments on Zr-BMG and Zr-CA have been introduced in Chapter 5.1.5, we prepared surfaces showing either smooth appearances on thermoplastic BMG or high-density nano-protuberances from randomly distributed embedded nano-crystallites with average sizes below 200 nm on the recrystallized alloy (Fig. 5.9). While the former material shows a specific high quality arrangement of standard ripples around the laser wavelength, the latter demonstrates strong predisposition to form high spatial frequency rippled structures.

We follow the initial topology changes upon the accumulation of incident pulses. Fig. 6.24 shows the SEM images of LIPSS on Zr-BMG and Zr-CA after irradiation at the fluence ϕ=0.38 J/cm² by linearly polarized 1, 2, and 4 laser pulses respectively, which are the partial enlarged views of Fig. 5.10(a1, a2).

For Zr-BMG, after 4 pulses, there are clear LSFL (⊥E) with a periodicity centered at 742 nm (Fig. 6.24(c)). In contrast, after 4 pulses, there are both LSFL (⊥E) with a periodicity centered at 708 nm and HSFL (∥E) with a periodicity centered at 384 nm on the Zr-CA (Fig. 6.24(f)). In details, after 1 pulse, many nano-scale protrusions appear on the Zr-CA, which are related to the initial nano-particles on Zr-CA surface before experiments. After 2 pulses, some short HSFL ripples parallel to laser polarization appear on the Zr-CA. After 4 pulses, HSFL ripples become longer and LSFL ripples perpendicular to laser polarization also appear on the Zr-CA. From these comparison experiments, HSFL formation on Zr-CA is related to the specific nanostructured surface of Zr-CA with nanoparticles.

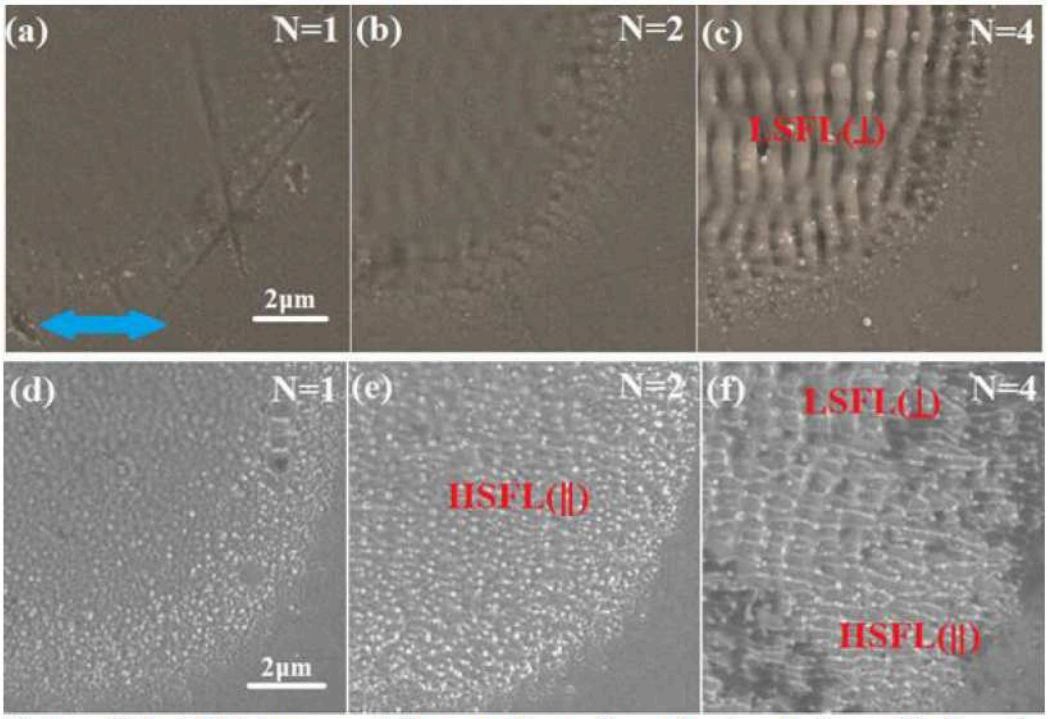

Figure 6.24: SEM images of the sample surface after irradiation with linearly polarized laser pulses at the fluence ϕ=0.38 J/cm^2: (a) Zr-BMG after 1 pulse, (b) Zr-BMG after 2 pulses, (c) Zr-BMG after 4 pulses, (d) Zr-CA after 1 pulse, (e) Zr-CA after 2 pulses, (f) Zr-CA after 4 pulses. The pulse number is shown in every image. The electric polarization direction of the laser beam is indicated with a double-headed arrow in (a). LSFL(⊥) represents LSFL ripples perpendicular to laser polarization. HSFL(∥) represents HSFL ripples parallel to laser polarization.

The electromagnetic solutions of the field distribution are strongly influenced by the surface state [SYP+83, GFS82, SRO+12, ZCL+15, LCC+16]. We have seen that in the Zr-CA case we have an initial inherent roughness while on both BMG and Zr-CA, subsequent laser exposure in the vicinity of the threshold will add new topology features, from localized centers for phase transition [AKO+14] to ordered corrugation. We estimate that the energy distribution following the exposure of rough surfaces is driven by local effects determined by single-nanoparticle scattering and multiple-nanoparticles collective inter-coupling scattering effects. The effect on LSFL being largely discussed and implying stationary structured field distributions involving interference effects, we concentrate here of fine HSFL structures oriented parallel to the field.

At first, the role of the nanoparticle in the electromagnetic energy modulation on Zr-CA surface is investigated by 3D finite-difference time-domain (FDTD) simulations. Using the same FDTD model in Fig. 6.12, with the Zr-CA refractive index ñ

=2.59+3.30i, the scattering energy and field pattern induced by a single nano-protuberance is given in Fig. 6.25 for the case of a ϕ=100-nm hemisphere on flat Zr-CA surface.

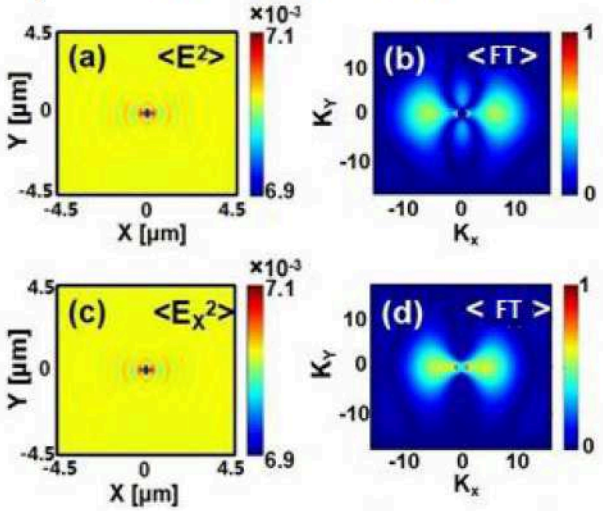

Figure 6.25: Energy distribution patterns around a nanoscale topological feature of a ϕ=100 nm hemisphere on flat Zr-CA surface. (a) Total energy distribution pattern derived from time-averaged E^2 with (b) its Fourier transformation (FT). (c) Insights into the X-component of energy distribution derived from time-averaged E_x^2 with (d) its FT. Note that laser polarization is along X axis. Identical color scales are used for (b) and (d).

Similar to Fig. 6.12, a main channel in the energy modulation comes from the near-field enhancement at the edge of nano-protuberance, while at larger distance field modulation along K_x is driven by scattering patterns and interference with the incident fields (Fig. 6.25(d)). The higher spatial frequency component has a mixed origin, scattering in a characteristic pattern and potential interferential interactions along the polarization direction K_y (Fig. 6.25(b)). The field patterns generated by a single nanoscale topological feature will be amplified and reordered in the case of an ensemble of particles.

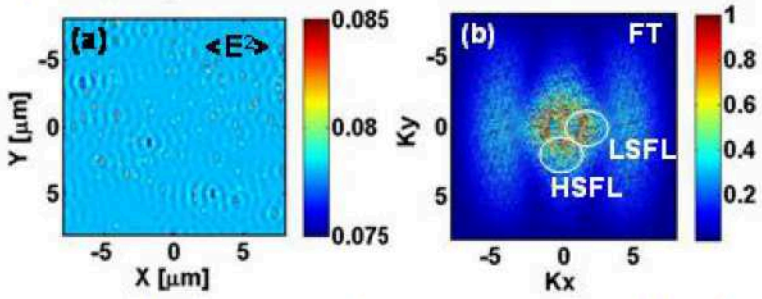

Figure 6.26: Energy distribution patterns for an ensemble of nanoscale topological features of randomly distributed nanoparticles on flat Zr-CA surface. (a) Total energy distribution pattern derived from time-averaged E^2 with (b) its FT. Note that laser polarization is along X axis.

Fig. 6.26 represents modulated energy patterns resulting from structured stationary fields distribution in the case of a high density ensemble of nanoparticles (1000 nanoparticles with the same size of 40 nm × 40 nm × 40 nm are distributed randomly on the flat surface with the size of 25 μm × 25 μm). Fig. 6.26(a) is the time-averaged E^2 distribution at the surface, with its Fourier analysis given in Fig. 6.26 (b). As in the case of a nanoparticle, the real space and K-space analyses in Fig. 6.26 show a periodic spatial feature with its vector aligned on K_x (structures perpendicular to the field). Their K value of about 1.25 (corresponding to λ/1.25) relates the features to LSFL originating from interference between scattered and incident fields. The features along K_y with higher spatial frequencies in the HSFL range and width have a dual nature, originating in both interference and scattering, with a strong inter-particle coupling and mutual coherent interactions. We therefore relate spatial features in the HSFL band to both coherent interactions with the incident field and inter-particles scattering interactions without involving a modulating interaction with the incident field. However, though an electromagnetic (EM) approach satisfies the dimensional analysis, one problem related to the EM interpretation is that the contrasts typically associated to HSFL are significantly smaller than those of LSFL, suggesting a lower probability of formation, somehow in contradiction with the experimental results. These effects depend on the particle size and we therefore take into account the near-field interaction around the nanoparticle.

A complementary analysis of the field interaction with a single nanoscale topography feature shows a singular feature of the structured field in the near-range of the nanoparticle. A localized field enhancement with poles aligned along the polarization becomes visible already in Fig. 6.25(a). The field enhancement factor depends on the geometry and the size of the nano features. Fig. 6.27(a) puts into the evidence of this effect by resuming the dimensional effect of the nanoparticle with the different sizes of ϕ=100 nm, ϕ=200 nm, ϕ=400 nm and ϕ=800 nm on energy redistribution. Observing the time-averaged E^2 distribution along X (at Y=0) in Fig. 6.27(b), we note both a near-field enhancement and an increase of modulation on a larger scale coming from the interference between the incident and the scattered wave. The modulation contrast maximizes when the particle size approaches the incident wavelength suggesting an increase in the scattering efficiency while the field enhancement stays high for subwavelength sizes. We conclude that for nano-particles with the size similar to those observed on the Zr-CA surface, the near-field enhancement may play a role in the

electromagnetic energy modulation. At the same time, as for the bigger size of nanoparticles, the interference between scattered wave and incident laser becomes stronger. This becomes a driving factor in forming the LSFL ripples perpendicular to laser polarization.

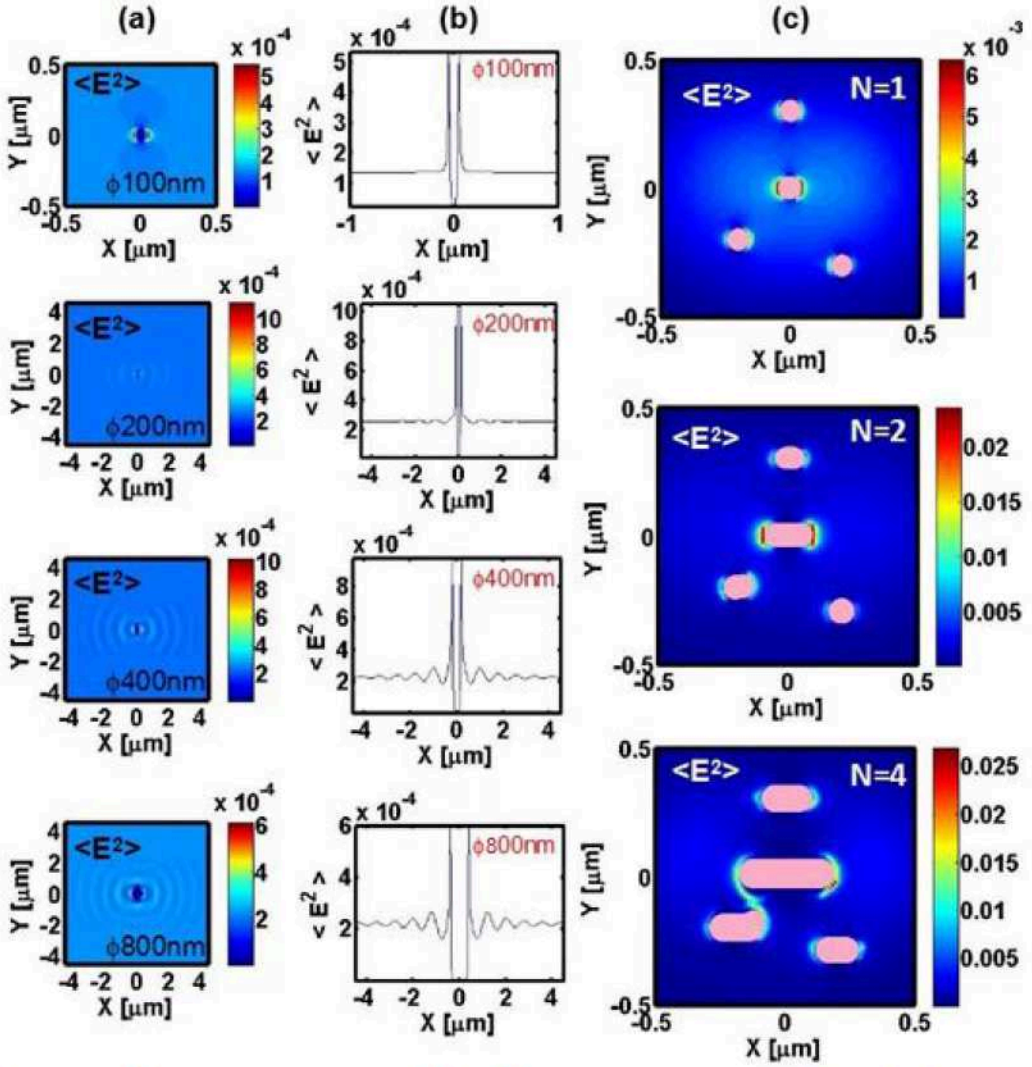

Figure 6.27: (a) Time-averaged E^2 distribution on the surface XOY plane induced by a hemisphere of different diameters: ϕ=100 nm , ϕ=200 nm , ϕ=400 nm, ϕ=800 nm; (b) Time-integrated E^2 distribution along Y=0 axis induced by a hemisphere with different sections: ϕ=100 nm, ϕ=200 nm, ϕ=400 nm, ϕ=800 nm; (c) Time-averaged E^2 distribution on XOY plane induced by four hemispheres of ϕ=100 nm with the number of pulses. Top: a first incident pulse, middle: elongated structures interact with a second pulse, bottom; more elongated ripple in interaction with a forth pulse. The ripple domains are indicated by the pink color. The polarization direction of the incident planewave is along X axis.

We speculate that the field enhancement in the near-field range leads to energy localization at the sides and thus to thermal gradients. Considering the material motion along this direction driven by the

thermal gradients in thermo-capillary convection [VD12], we foresee an anisotropic (linear) growth for the nano-features along the polarization direction. Assuming that the material growth covers the region of field-enhancement at the lower laser fluence below single-shot ablation threshold, we can observe now a feedback mechanism developing with the increase of the number of pulses.

The experimental results depicted in the inset of Fig. 6.24(d-f) shows already a gradual evolution from spherical to elongated forms with N varying from 1 to 4. Already after the 2nd pulse, high frequency short regular structures form along the direction of laser polarization from an ensemble of many nano-particles (Fig. 6.24(e)). After N=4 pulses, the pattern of HSFL becomes fully visible. This supports a hypothesis of HSFL feature being influenced by the feedback process between the surface nanostructures and laser pulses.

We have tried to simulate the process by considering a topological effect of the near-field enhancement. The effect is visualized in the following 3D-FDTD simulations assuming a Zr-CA flat surface with some same hemispheres on surface, built as the surface model, and the results are given in Fig. 6.27(c).The diameter of the hemispheres is set to 100 nm. The results show the time-averaged E^2 distribution on XOY plane with the incoming pulses on a variable topology. Near-field enhancement determines energy modulation, and the maximum energy is distributed at the edge of hemisphere along X axis, consistent with the polarization direction of incident plane wave. It is presumed that the ripple grows at first in the region absorbing maximum energy, so the initial nano-particle becomes longer along X axis after first laser pulse, forming one short ripple. This is related to material flow and assumes that the ablation threshold is not achieved in the enhancement region. According to the maximum energy distribution in the case of N=1 pulse in Fig. 6.27(c), the next short nanostructure model is built in the second step of the FDTD simulation. In the same simulation conditions, after the second pulse, the time-averaged E^2 distribution on XOY plane elongates furthermore, as shown in the case of N=2 pulses in Fig. 6.27(c). Maximum energy gets localized at the two ends of the initial short ripple, contributing to additional enlargement along X axis. This is also confirmed after an irradiation as shown in the case of N=4 pulses in Fig. 6.27(c). This process can thus lead to the development of elongated structures where the inter-distance is given by the initial distribution of nano-particles. The scenario can be applied for the case of many random distributed nano-particles on Zr-CA surface, contributing to

the formation of initial HSFL ripples. Thus, the feedback process that become apparent in the simulations in Fig. 6.27(c) can lead to a polarization-assisted anisotropic grow of the structures in directions parallel to the polarization.

The whole process has equally an influence on the LSFL, as scattering depends on the size of the scatterers. As sizes of initial nano-particles and short ripples enlarge gradually with increasing laser pulses, the contrast of energy modulation originating in the coherent interaction between the incoming field and the scattered waves increases (shown in Fig. 6.27(a, b)), contributing to the enhancement of LSFL ripples perpendicular to laser polarization. The pulse-dependent size effect of surface nanostructures seems consistent with the LIPSS evolution in the experiment in Fig. 6.24(d-f), in which HSFL ripples form in the first several pulses, then LSFL ripples form in the following pulses with bigger size of surface nanostructures. The evolutions of both HSFL and LSFL ripples with the increasing pulses are discussed in the following.

Similar to Fig. 6.27(c), the feedback coupling laser pulses and the rough surface with the nanoparticles including the near-field induced elongation is simulated by FDTD method. In the simulation, the initial rough surface model is a flat surface with an ensemble of nanoparticles (500 nanoparticles with the same size of 100 nm×100 nm×50 nm (length×width×height) are distributed randomly on the flat surface with the size of 10 μm×10 μm). The polarization direction of laser pulses is along X axis. After the rough surface is irradiated by each laser pulse, the elongation of every nanoparticle along the polarization direction occurs according to the near-field energy distribution, leading to the evolution of surface topographies. In the next pulse, the surface model of new topographies is used in the simulation, leading to the new energy modulations. The simulation results are shown in Fig. 6.28, representing the feedbacks between laser pulses and the rough topographies involving the near-field induced elongation. Fig. 6.28(a-d) are respectively the time-averaged E^2 distributions at the pulses of N=1, 2, 3, 4, while the corresponding Fourier transformations are shown in Fig. 6.28(e-h)), which shows the intricate evolution of energy distribution. As the inter-particles distance is comparable to the gradual elongation, narrow HSFL-like lines are becoming apparent via particle interconnection along X axis (Fig. 6.28(d, h)). The mutual influence between topology and field becomes equally visible in the enforcement of LSFL with the number of pulses, in the conditions where the sole topography evolution was related to particle

elongation and interconnection. This indicates a reinforced correlation between scattering and particulates geometries.

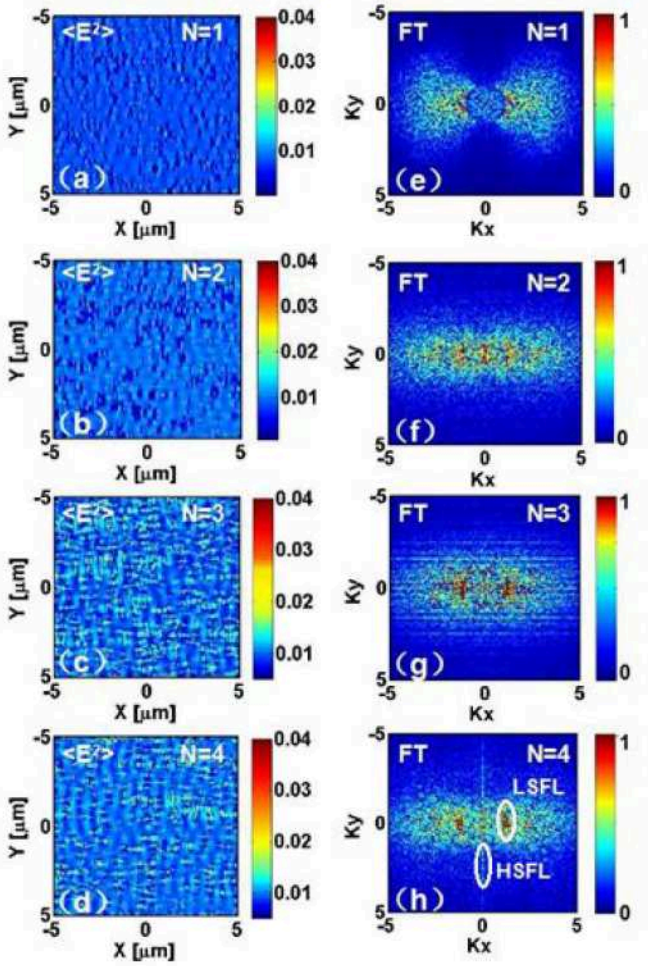

Figure 6.28: Time-averaged E^2 distribution for an ensemble of randomly-distributed nanoparticles subject to near-field induced elongation for the pulses of (a) N=1, (b) N=2, (c) N=3, (d) N=4. The corresponding Fourier transformations are respectively given in (e, f, g, h). The polarization direction of the incident planewave is along X axis.

In summary, we argued that a type of HSFL ($\parallel$E) is intrinsically related to the presence of nano-scaled roughness on surfaces by experiments and simulations. Different from the HSFL ($\perp$E) formation mainly due to the coherent interference between scattered fields, we propose scenarios for HSFL ($\parallel$E) formation relying on individual anisotropic near-field enhancement processes and collective mixed scattering and interference effects driven by the incident field and inter-particle coupling. The near-field enhancement becomes important for particles sizes in the 200-400 nm range and can drive anisotropic structure growth along the polarization direction, giving thus an essential feedback base. We discuss the potential situation where local feedback-driven effects and collective scattering concur to a topology-related evolution of

HSFL. Equally scattering and coherent interaction with the incident field contribute to LSFL formation.

6.7 FDTD simulation for LIPSS formation on fused silica

The electromagnetic solutions of the field distribution are determined by dielectric function of materials. We have seen that the electromagnetic energy distribution induced by a nano-hole on the Zr-BMG and fused silica surfaces are different in Fig. 6.13(e, f), experiencing equally a $\pi/2$ rotation. We also estimated that the energy distribution following the exposure of rough surfaces is driven by local effects determined by single-nanohole scattering and multiple-nanoholes collective inter-coupling scattering effects. We concentrate here on the generation of modulated light patterns in the context of LIPSS on fused silica.

At first, the role of a nanohole in the electromagnetic energy distribution on fused silica surface is investigated by 3D-FDTD simulations. Considering the small changes of optical index in the excited fused silica in the ultrashort pulse duration in Ref. [SCA+14], only unexcited fused silica is simulated here. In the FDTD model, the refractive index of unexcited fused silica is $\tilde{n}$ =1.453+0i [Pal85]. The scattering energy and field pattern induced by a single nano-hole is given in Fig. 6.29 for the case of a ϕ=100-nm hemisphere hole on flat fused silica surface.

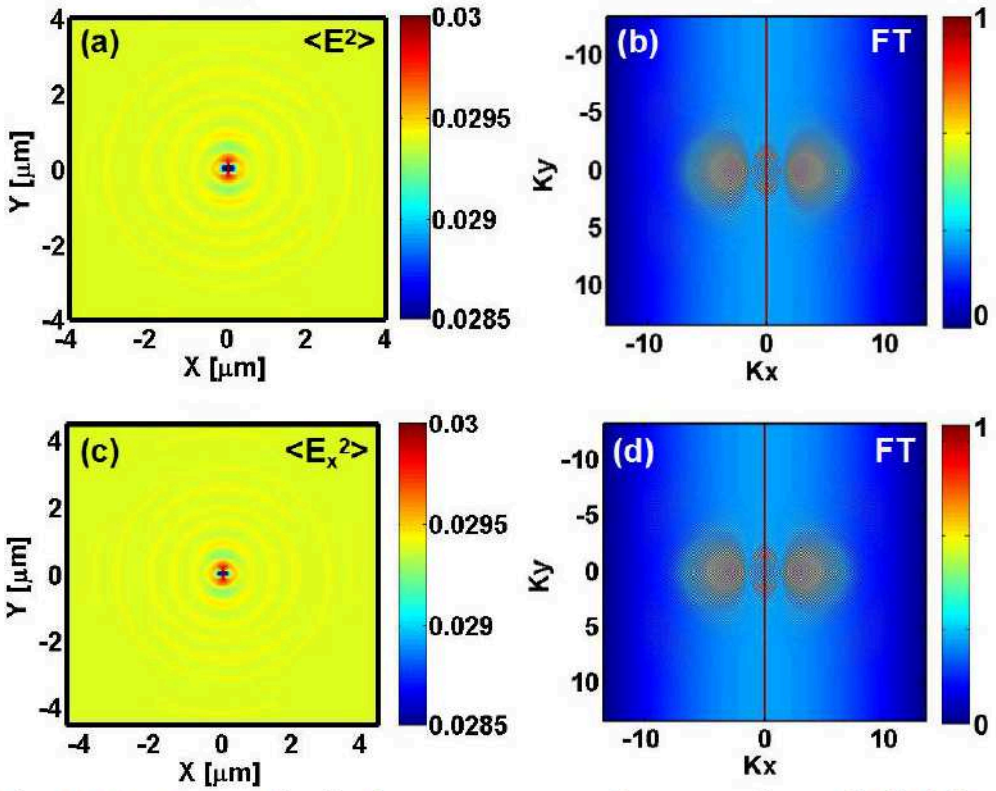

Figure 6.29: Energy distribution patterns around a nanoscale topological feature of a ϕ=100 nm hemisphere hole on flat fused silica surface. (a) Total energy distribution pattern derived from time-averaged E^2 with (b) its Fourier transformation (FT). (c) Insights into the X-component of energy distribution derived from time-averaged Ex^2 with (d) its FT. Identical color bars are used for (b) and (d).

Similar to the mechanism discussed for BMG in Fig. 6.12, the energy distribution mainly comes from the field modulation, driven by scattering patterns and interference with the incident fields (Fig. 6.29(a, c)). The spatial frequency component K_x =3.5 is related to HSFL(⊥E) (Fig. 6.25(b, d)), while the spatial frequency component K_y =1.5 is related to LSFL(∥E) (Fig. 6.25(b, d)). The field patterns generated by a single nanoscale topological feature will be amplified and reordered in the case of an ensemble of particles.

In order to simulate the rough surface induced by a few laser pulses, a flat surface with 1000 cubic nanoholes in random distribution on the surface is built for the FDTD simulation model [SRO+12]. The cubic particle size is 25 nm ×25 nm×50 nm (length×width×height). The surface size is 25 μm×25 μm. The incident plane wave propagates along the Z axis. It has the wavelength of 800 nm and the polarization aligned along the X axis.

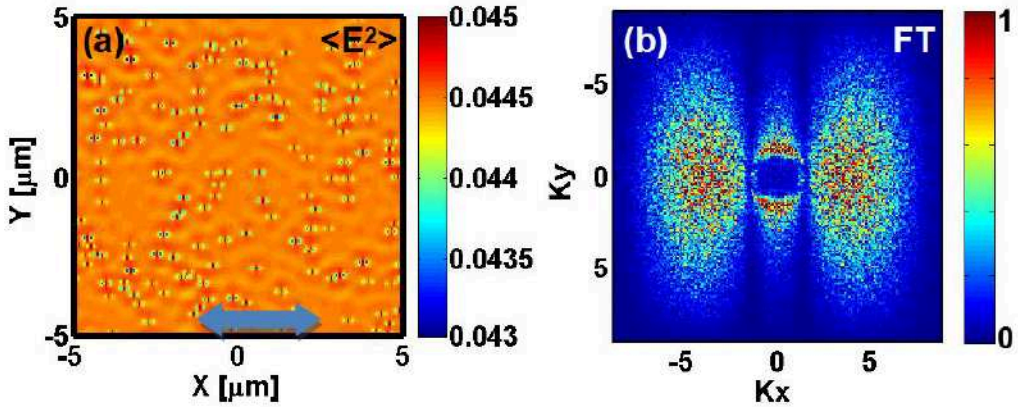

Figure 6.30: (a) Time-averaged E^2 distribution on the surface for an ensemble of randomly-distributed nanoholes. (b) 2D-FFT of the intensity distribution in (a). Note that laser polarization is along X axis.

Fig. 6.30 shows the time-averaged E^2 for whole pulse duration on the rough surface, representing the energy modulation. The energy on the surface is modulated with a pattern similar to the typical ripples, as shown in Fig. 6.30(a). Fig. 6.30(b) shows the 2D-FFT of the Fig. 6.30(a). The energy distribution have the spatial periods of Λ=800/3.5=229 nm ($\perp$E) and Λ=800/1.5=533 nm ($\parallel$E), which respectively agree reasonably well with that of HSFL($\perp$E) and LSFL($\parallel$E) on fused silica in the Chapter 5.1.3. The LIPSS formation on fused silica can be therefore related to the interference between incident laser and surface scattered wave induced by rough surface.

In summary, compared with LSFL($\perp$E) on metals and semiconductors, the direction difference of the LSFL($\parallel$E) on fused silica can be explained by the electromagnetic energy distribution induced by a nanohole, which is intrinsically related to the dielectric function. The LIPSS formation on fused silica can be related to the interference between incident laser and surface scattered wave induced by rough surface.

6.8 Conclusion

We developed an electromagnetic perspective on LIPSS formation. FDTD method is used to compute the energy distribution and stationary patterns of electromagnetic field on the model surfaces where the topography relies on nanoscale roughness. LIPSS formations on aluminum and germanium are analyzed comparatively by the Sipe efficacy theory and FDTD simulations, offering the information about the energy transfer from the electromagnetic field above the surface to the material beneath the rough surface in case of

metallic and semiconducting materials. We draw attention to a gain in accuracy using FDTD.

The application to model surfaces take into account local topographies, simulated as nanoparticles In order to investigate the role of nanostructures in LIPSS formation, the effect of localized surface plasmons (LSP) in Ag nanoparticle and the scattering characteristics of Ag, Ge, silica nanoparticles are respectively investigated by FDTD simulations, revealing that metal nanoparticles on the surface have much stronger scattering enhancement than both semiconductor and dielectric nanoparticles, because of potentially excited LSP on metal nanoscale protrusions.

For LSFL formation mechanism, the initial LIPSS evolutions with increasing number of fs laser pulses are analyzed, taking into account surface topology evolutions. Using FDTD, the electromagnetic calculations show the role of scattering around individual centers at first, indicating that the energy modulation is mainly derived from the interference between incident laser and scattered light. We indicate via a choice of materials that the effect on spacing period and pattern of energy modulation for given surface nanostructure geometries and materials. For metals, LSP can be excited on surface nanostructure, enhancing the electric field in the near-field zone and light scattering. An LSFL formation scenario is thus proposed relying on interference between the incident laser and scattered light, In addition, the effects of one-dimensional nanostructure geometries (submicron-sized groove) on LSFL formation are investigated by FDTD showing the influence on orientation. Specifically here, it was showed that the variable efficiency of ripples parallel to the groove is related to the decreasing amplitude of the scattered surface wave induced by the declining laser component with polarization perpendicular to the groove.

For HSFL ($\perp$E) on CMSX-4, FDTD simulations confirm that the coherent interference between scattered sources plays a role in energy modulation, contributing to the formation of HSFL perpendicular to laser polarization.

For HSFL ($\parallel$E) on Zr-CA, we propose scenarios for HSFL formation relying on individual anisotropic field-enhancement processes and collective mixed scattering and interference effects driven by the incident field and inter-particle coupling. The field enhancement becomes important for particles sizes in the 200-400 nm range and can drive anisotropic structure growth along the polarization direction, giving thus an essential feedback base. We discuss the potential situation where local feedback-driven effects

and collective scattering concur to a topology-related evolution of HSFL.

For HSFL($\perp$E) and LSFL($\parallel$E) on the dielectric fused silica, that are beyond the scope of Sipe theory, we propose scenarios for these formations relying on the interference between incident laser and surface scattered wave induced by rough surface.

Overall, LIPSS formation can be explained by deposited energy modulation on surface via electromagnetic effects. The energy modulation mainly comes from the interference between incident laser and scattered surface wave, being complemented by the interference between scattered surface waves. Scattered surface wave are induced by surface nanostructures, such as surface roughness, defect lines (grooves), nanoholes and nanoparticles on surface. Laser ablation can produce new surface nanostructures, at the same time, new nanostructures induce different scattered surface wave, leading to a new feedback-driven energy modulation deposited on surface.

Chapter 7

Conclusions and perspectives

In the presented work, we have studied fs-LIPSS formation on solids by experiments and FDTD simulations. The aim was to investigate the formation mechanisms of fs-LIPSS relying on features observable in the electromagnetic field domain.

The work discussed in this dissertation explores fs-LIPSS formation mechanisms on several solids, involving metals, multielement alloys, semiconductors and dielectrics. Specifically, it focuses on investigating the roles of surface topologies and the influence of micro/nano-structures in LIPSS formation. Using surfaces of defined topologies, defects of selected geometries and associated FDTD simulations we have explicitated individual and collective roles in LIPSS formation of nano-holes, nano-hemispheres, linear sub-micron grooves, multiple-nanoparticles, rough randomized surfaces. These results are then used to explain the LSFL and HSFL formation on different materials.

The main and original results of the current work are as follows.

7.1 Conclusion

Following the range of processes involved in LIPSS formation we have developed techniques to probe and evaluate the optical response of ultrafast excited materials. The transient optical properties of silicon, tungsten and Zr-BMG excited by ultrafast laser pulses are measured by a single-color two-angle time-resolved ellipsometry respectively. Our measurements show the different complex dynamic processes of optical properties in the metal and

semiconductor excited by ultrafast pulses. Thus we have indicated Drude-like reponse in case of Si, non-plasmonic to plasmonic transitions in W in the vicinity of the damage threshold, but equally a certain constancy of the optical properties of multielement alloy in view of their specific density of states. Above threshold, rapid transitions towards lower-density ionized sates were observed. The transient measurements were complemented with aposteriori analysis of rippled zones from a topology and structural/compositional point of view.

Experiments of fs-LIPSS on six different materials were carried out, and analyzed by SEM and AFM, showing the different LIPSS on metal tungsten, semiconductor silicon, dielectric fused silica, single-crystal superalloy CMSX-4, amorphous alloy Zr-BMG and its corresponding crystal alloy Zr-CA respectively, providing the experimental results for the investigating the LIPSS formation mechanism. Except the widely existent LSFL($\perp$E) on the semiconductor silicon, metal tungsten, alloy CMSX-4, Zr-BMG and Zr-CA, the special HSFL($\perp$E) on CMSX-4 and HSFL($\parallel$E) on Zr-CA are observed. Different from the widely existent LSFL($\perp$E) on the semiconductors and metals, the LSFL($\parallel$E) exist on the dielectric fused silica, revealing the role of dielectric function in the direction of LSFL. By EDX, the analysis of the chemical composition along the ripple lines on Zr-BMG led to believe that a mechanism of selective vaporization is at work. The analysis of the lattice structures shows that Zr-BMG stays amorphous after irradiation, exceptionally with some local crystallization elements under high doses, checked by EBSD.

To investigate LIPSS formation mechanisms, FDTD method is used to compute the energy distribution of electromagnetic field on the surface model with different nano-structures. In comparison with Sipe theory, FDTD simulations precisely offer the information about the energy transfer from the electromagnetic field above the surface to the material beneath the rough surface. To investigate the effect of nanoparticles in the scattering field, the scattering characteristics of Ag, Ge, silica nanoparticles are respectively analyzed, revealing that metal nanoparticles on the surface have much stronger scattering enhancement than both semiconductor and dielectric nanoparticles, because of potential excitation of LSP on metal nanoprotuberances. LIPSS formation can be explained by deposited energy modulation on surface via electromagnetic effects. The energy modulation mainly comes from the interference between incident laser and scattered surface wave (for LSFL($\perp$E)), being complemented by the interference between scattered surface waves (for HSFL($\perp$E)),

revealing that LSFL and HSFL have different formation mechanisms. Scattered surface wave are induced by surface nanostructures, such as surface roughness, defect lines (grooves), nanoholes and nanoparticles on surface. Specially, for HSFL (∥E) on Zr-CA, we argued that the scenarios for HSFL (∥E) formation rely on individual anisotropic field-enhancement processes, intrinsically related to the presence of nano-scaled roughness on Zr-CA surfaces and collective mixed scattering and interference effects driven by the incident field and inter-particle coupling. The evolving surface topology leads to a feedback-driven energy modulation deposited on surface. Compared with LSFL(⊥E) on metals and semiconductors, the direction difference of the LSFL(∥E) on fused silica can be explained by the electromagnetic energy distribution induced by a nanohole, which is intrinsically related to the dielectric function. The LIPSS formation on fused silica can be related to the interference between incident laser and surface scattered wave induced by rough surface.

The presented formation mechanism of LIPSS has nevertheless applicability limits. The model is only applicable for surface structures of different materials in the electromagnetic field domain and does not include the complex processes, such as incubation effects, harmonic generation and the thermodynamics of molten or ablated materials. The model neglects the effect of ablation plasmas on the LIPSS formation. The model focuses the electromagnetic origin of LIPSS formation and reveal however a potential primary factor for energy modulation and formation of LIPSS.

7.2 Perspectives

The performed works have many perspectives. From the fundamental point of view, the following improvements and extensions can be done. Extended knowledge on ultrafast material excitation and structural evolutions in the conditions of LIPSS can be obtained by developing large band time-resolved ellipsometry methods (e.g. using supercontinuum probes) or by implementing the latest advances in terms of probing electronic and structural effects (from time-resolved diffraction to core-level absorption).

These can be complemented by experiments following the LIPSS growth dynamics. For the experiments of LIPSS formation, the performed investigations are based on the resulting topography of LIPSS by SEM and AFM to elucidate the LIPSS formation mechanism. These can be extended with a dynamic component. On a fundamental level, other types of experiments are needed to

elucidate the LIPSS formation mechanisms, for example, time- and space-resolved pump-probe microscopy image [RDS+13], pump-probe shadowgraphic images [MMP+08]. The dynamics of LIPSS formation can be observed at fs–ns time scale after excitation by these experiments.

From the calculation point of view, the present work mainly focus on the linear interaction of electromagnetic fields, so future work will involve nonlinear effects in the FDTD simulations, such as transient optical properties, harmonic generation, optical Kerr effect and so on. Besides the effects of electromagnetic fields, thermodynamics of molten or ablated materials and plasma also affect the LIPSS formations, so the complex models including the electromagnetic fields, thermodynamics of molten or ablated materials and their hydrodynamic evolutions will be investigated in the future work for LIPSS formation.

Another challenging work would be the investigation of the physical nature of radiation remnants on semiconductors in Sipe theory, as well as the relationship between radiation remnants and localized surface plasmons. We will use quantum mechanics to reveal the physical nature of radiation remnants and its relationship with localized surface plasmons.

Finally, future studies will include the application of LIPSS and transient optical properties of excited materials. LIPSS provides a fast, precise and low-cost tool for surface micro/nano-structuring. Except the traditional applications, such as surface wetting, tribology, dye-free coloring, marking and coding, a remarkable application of LIPSS is the high-efficiency substrates for surface-enhanced Raman spectroscopy (SERS) [MDL+14]. Another promising application of LIPSS is the phase-matching grating for surface plasmonic waveguide [HZC+09]. On the other hand, transient optical properties of excited materials by ultrafast laser have the potential applications in photonic devices and optical switching. For example, the ultrafast switch of surface plasmons could be designed according to the nonplasmon-to-plasmon transition in excited tungsten by femtosecond laser pulse in Chapter 4.

Despite the recent advances in the understanding of fs-LIPSS formations on solids, of which a small range of questions was approached in the present work. We confirm that there are still a lot of answered questions and a great number of unrevealed mysteries amongst themselves. We will insist on researching.

Bibliography

[ACS84] R. A. Abram, G. N. Childs, and P. A. Saunderson. *Band gap narrowing due to many-body effects in silicon and gallium arsenide*. Journal of Physics C: Solid State Physics, **17**(34): 6105-6126, 1984.

[AIZ12] S. I. Ashitkov, N. A. Inogamov and V. V. Zhakhovskii. *Formation of nanocavities in the surface layer of an aluminum target irradiated by a femtosecond laser pulse.* JETP Letters, **95**(4): 176-181, 2012.

[AK01] T. Abeln, and U. Klink, Laser strukturieren zur Verbesserung der tribologischen Eigenschaften von Oberflächen, in Proc. of Stuttgarter Lasertage, 2001.

[AKO+14] S. I. Ashitkov, P. S. Komarov, A. V. Ovchinnikov, E. V. Struleva, V. V. Zhakhovskii, N. A. Inogamov, M. B. Agranat. *Ablation and nanostructuring of metals by femtosecond laser pulses.* Quantum Electronics, **44**(6):535–539, 2014.

[AKP74] S. I. Anisimov, B. Kapeliov, and T. L. Perelman. *Electron-Emission from Surface of Metals Induced by Ultrashort Laser Pulses*. Soviet Journal of Experimental and Theoretical Physics, **39**:375-377, 1974.

[And78] P. W. Anderson. *Local Moments and Localized States.* Science, **201**(4353):307-316, 1978.

[ARL+15] S. I. Ashitkov，S. A. Romashevskiy，P. S. Komarov，A. A. Burmistrov，V. V. Zhakhovsky, N. Inogamov, and N. B. Agranat. *Formation of nanostructures under femtosecond laser ablation of metals.* Quantum Electronics, **45**(6):547-550, 2015.

[AS71] N. W. Ashcroft and K. Sturm. *Interband absorption and the optical properties of polyvalent metals.* Physical Review B, **3**(6):1898–910, 1971.

[AT02] F. V. Anantha and A. Taflove. *Efficient modeling of infinite scatterers using a generalized total-fieldscatteredfield FDTD boundary partially embedded within PML*. IEEE Transactions on Antennas and Propagation. **50**(10):1337–1349, 2002.

[BA82] R. Biswas and V. Ambegaokar. *Phonon spectrum of a model of electronically excited silicon*. Physical Review B, **26**(4):1980-1988, 1982.

[BBK+02] J. Bonse, S. Baudach, J. Krüger, W. Kautek, and M. Lenzner. *Femtosecond laser ablation of silicon-modification thresholds and morphology*. Applied Physics A. **74**(1):19–25, 2002.

[BBK99] S. Baudach, J. Bonse, and W. Kautek. *Ablation experiments on polyimide with femtosecond laser pulses*. Applied Physics A. **69**(Suppl.):S395–S398, 1999.

[BCR+14] E. Bévillon, J. P. Colombier, V. Recoules, and R. Stoian. *Free-electron properties of metals under ultrafast laser-induced electron-phonon nonequilibrium: A first-principles study*. Physical Review B, **89**(11):115117, 2014.

[BCR+16] E. Bévillon，J. P. Colombier，V. Recoules，H. Zhang，C. Li，R. Stoian. *Ultrafast Surface Plasmonic Switch in Non-Plasmonic Metals*. Physical Review B, **93**(16):165416, 2016.

[BH03] A. Borowiec and H. K. Haugen. *Subwavelength ripple formation on the surfaces of compound semiconductors irradiated with femtosecond laser pulses*. Applied Physics Letters, **82**(25): 4462-4464, 2003.

[BH88] R. M. Bradley and J. M. E. Harper. *Theory of ripple topography induced by ion bombardment*. Journal of Vacuum Science & Technology A, **6**:2390, 1988.

[Bir65] M. Birnbaum. *Semiconductor surface damage produced by ruby lasers*. Journal of Applied Physics, **36**(11):3688-3689, 1965.

[BKG+97] T. D. Bennett, D. J. Krajnovich, C.P. Grigoropoulos, P. Baumgart and A.C. Tam. *Marangoni Mechanism in Pulsed Laser Texturing of Magnetic Disk Substrates*. J. Heat Transfer, **119**(3):589-596, 1997.

[BKH+12] J. Bonse, J. Krüger, S. Höhm, and A. Rosenfeld. *Femtosecond laser-induced periodic surface structures*. Journal of Laser Applications, **24**(4):042005, (2012).

[BKH+15] J. Bonse, R. Koter, M. Hartelt, D. Spaltmann, S. Pentzien, S. Höhm, A. Rosenfeld, and J. Krüger. *Tribological performance of femtosecond laser-induced periodic surface structures on titanium and a high toughness bearing steel*. Applied Surface Science, **336**: 21–27, 2015.

[Blo03] R. Blossey. *Self-cleaning Surfaces-virtual Realities*. Nature Material, **2**(5):301-306, 2003.

[BLZ+11] S. Beckford, N. Langston, M. Zou and R. Wei. *Fabrication of durable hydrophobic surfaces through surface texturing*. Applied Surface Science, **257**:5688–5693, 2011.

[BMJ+14] R. Buividas, M. Mikutis, S. Juodkazis. *Surface and bulk structuring of materials by ripples with long and short laser pulses: Recent advances*. Progress in Quantum Electronics, **38**(3): 119-156, 2014.

[BMS05] J. Bonse, M. Munz, and H. Sturm. *Structure formation on the surface of indium phosphide irradiated by femtosecond laser pulses*. Journal of Applied Physics, **97**(1), 013538, 2005.

[BRK09] J. Bonse, A. Rosenfeld, and J. Krüger. *On the role of surface plasmon polaritons in the formation of laser-induced periodic surface structuresupon irradiation of silicon by femtosecond-laser pulses*. Journal of Applied Physics, **106**(10):104910, 2009.

[BRK11] J. Bonse, A. Rosenfeld, and J. Krüger. *Implications of transient changes of optical and surface properties of solids during femtosecond laser pulse irradiation to the formation of laser-induced periodic surface structures*. Applied Surface Science, **257**:5420–5423, 2011.

[BRŠ+11] R. Buividas, L. Rosa, R. Šliupas, T. Kudrius, G. Šlekys, V. Datsyuk, and S. Juodkazis. *Mechanism of fine ripple formation on surfaces of (semi)transparent materials via a half-wavelength cavity feedback*. Nanotechnology, **22**(5):055304, 2011.

[BSC+10] J. Byskov-Nielsen，J. M. Savolainen，M. S. Christensen，and P. Balling. *Ultra-short pulse laser ablation of metals: threshold fluence, incubation coefficient and ablation rates*. Applied Physics A, **101**(1):97-101, 2010.

[BSS+11] E. V. Barmina, A. A. Serkov, E. Stratakis, C. Fotakis, V. N. Stolyarov, I. N. Stolyarov, and G. A. Shafeev. *Nano-textured W shows improvement of thermionic emission properties*. Appl. Phys. A, **106**(1):1-4, 2011.

[BZS+09] M. Barberoglou, V. Zorba, E. Stratakis, E. Spanakis, P. Tzanetakis, S. Anastasiadis, C. Fotakis. *Bio-inspired water repellent surfaces produced by ultrafast laser structuring of silicon*. Applied Surface Science, **255**(10):5425–5429, 2009.

[CBB+02] D. L. Cochran, D. Buser, C. M. ten Bruggenkate, D. Weingart, T. M. Taylor and J. P. Bernard. *The Use of Reduced Healing Times on ITI Implants with a Sandblasted and Acid-Etched (SLA) Surface: Early Results from Clinical Trials on ITI SLA Implants*. Clinical Oral Implants Research, **13**(2):144-153, 2002.

[CC88] M. L. Cohen, J. R. Chelikowsky. *Electronic Structure and Optical Properties of Semiconductors*. Springer, Berlin, 1988.

[CCA+12] J. P. Colombier, P. Combis, E. Audouard, R. Stoian. *Guiding heat in laser ablation of metals on ultrafast timescales: an adaptive modeling approach on aluminum*. New Journal of Physics, **14**:013039, 2012.

[CCTR11] J. Chen, W. Chen, J. Tang, and P. M. Rentzepis. *Time-resolved structural dynamics of thin metal films heated with femtosecond optical pulses*. PNAS, **108**(47):18887-18892, 2011.

[CFW+77] A. H. Clauer, B.P. Fairand, and B.A. Wilcox. *Laser shock hardening of weld zones in aluminum alloys*. Metallurgical and Materials Transactions A, **8**(12):1871–1876, 1977.

[CGB+12] J. P. Colombier, F. Garrelie, P. Brunet, A. Bruyère, F. Pigeon, R. Stoian, O. Parriaux. *Plasmonic and Hydrodynamic Effects in Ultrafast Laser-Induced Periodic Surface Structures on Metals*. Journal of Laser Micro/Nanoengineering, **7**(3):362-368, 2012.

[CGF+12] J. P. Colombier, F. Garrelie, N. Faure, S. Reynaud, M. Bounhalli, E. Audouard, R. Stoian, and F. Pigeon. *Effects of electron-phonon coupling and electron diffusion on ripples growth*

on ultrafast-laser-irradiated metals. Journal of Applied Physics, **111**(2):024902, 2012.

[CKR04] F. Costache, S. Kouteva-Arguirova, and J. Reif. *Sub-damage-threshold femtosecond laser ablation from crystalline Si: surface nanostructures and phase transformation*, Applied Physics A, **79**(4):1429–1432, 2004.

[CMN+96] B. N. Chichkov, C. Momma, S. Nolte, F. von Alvensleben, and A. Tünnermann. *Femtosecond, picosecond and nanosecond laser ablation of solids*. Applied Physics A, **63**(2):109–115, 1996.

[CNM+13] T. V. J. Charpentier, A. Neville, P. Millner, R. W. Hewson, A. Morina. Development of anti-icing materials by chemical tailoring of hydrophobic textured metallic surfaces. *Journal of Colloid and Interface Science,* **394**:539-544, 2013.

[CSP+05] S. J. Clark, M. D. Segall, C. J. Pickard, P. J. Hasnip, M. J. Probert, K. Refson, M. C. Payne. *First principles methods using CASTEP.* Zeitschrift fuer Kristallographie, **220**(5-6):67-570, 2005.

[DIT+13] T. J. Y. Derrien, Tatiana E. Itina, Rémi Torres, Thierry Sarnet, and Marc Sentis. *Possible surface plasmon polariton excitation under femtosecond laser irradiation of silicon.* Journal of Applied Physics, **114**:083104, 2013.

[DRD+09] D. Dufft, A. Rosenfeld, S. K. Das, R. Grunwald, and J. Bonse. *Femtosecond laser-induced periodic surface structures revisited: a comparative study on ZnO.* Journal of Applied Physics, **105**(3):034908, 2009.

[DRW+03] G. Dumitru, V. Romano, H.P. Weber, M. Sentis, and W. Marine. *Ablation of carbide materials with femtosecond pulses.* Applied Surface Science, **205**:80–85, 2003.

[DSS+10] B. Dusser, Z. Sagan, H. Soder, N. Faure, J. P. Colombier, M. Jourlin, and E. Audouard. *Controlled nanostructures formation by ultra fast laser pulses for color marking*. Optics Express, **18**(3):2913–2924, 2010.

[DTS+12] T. J. Y. Derriena, R. Torres, T. Sarnet, M. Sentis, T.E. Itina. *Formation of femtosecond laser induced surface structures on silicon: Insights from numerical modeling and single pulse experiments.* Applied Surface Science, **258**:9487–9490, 2012.

[DWC+15] A. Dunn, K. L. Wlodarczyk, J. V. Carstensen, E. B. Hansen, J. Gabzdyl, P. M. Harrison, J. D. Shephard, and D.P. Hand. *Laser surface texturing for high friction contacts.* Applied Surface Science, **357**:2313-2319, 2015.

[DZP+13] C. Deeb, X. Zhou, J. Plain, G. P. Wiederrecht, R. Bachelot, M. J. Russell, and P. K. Jain. *Size-Dependence of the Plasmonic Near-Field Measured via Single-Nanoparticle Photoimaging.* The Journal of Physical Chemistry C, **117**(20):10669–10676, 2013.

[EHH+09] R. Ernstorfer, M. Harb, C.T. Hebeisen, G. Sciaini, T. Dartigalongue, and R.J.D. Miller. *Experimental Evidence for Electronic Bond Hardening of Gold. Science*, **323**(5917): 1033–1037, 2009.

[EKK+14] A. V. Emelyanov, M. V. Khenkin, A. G. Kazanskii, P. A. Forsh, P. K. Kashkarov, M. Gecevicius, M. Beresna, and P. G. Kazansky.

Femtosecond laser induced crystallization of hydrogenated amorphous silicon for photovoltaic applications. Thin Solid Films, **556**: 410–413, 2014.

[FDD+14] C. Fourment, F. Deneuville, D. Descamps, F. Dorchies, S. Petit, O. Peyrusse, B. Holst and V. Recoules. *Experimental determination of temperature-dependent electron-electron collision frequency in isochorically heated warm dense gold*. Physical Review B, **89**(16):161110(R), 2014.

[FFH+01] D. Fisher, M. Fraenkel, Z. Henis, E. Moshe, and S. Eliezer. *Interband and intraband (Drude) contributions to femtosecond laser absorption in aluminum*. Physical Review E, **65**(2):016409, 2001.

[FS82] P. M. Fauchet and A. E. Siegman. *Surface Ripples On Silicon And Gallium Arsenide Under Picosecond Laser Illumination*. Applied Physics Letters, **40**(9):824-826, 1982.

[GA06] G. Gay and O. Alloschery. *Surface Wave Generation and Propagation on Metallic Subwavelength Structures Measured by Far-Field Interferometry*. Physical Review Letters, **96**:213901, 2006.

[GAA+09] X. Gonze, B. Amadon, P.-M. Anglade, J.-M. Beuken, et al.. *ABINIT: First-principles approach to material and nanosystem properties*. Computer Physics Communications, **180**:2582, 2009.

[GCP+11] F. Garrelie, J. P. Colombier, F. Pigeon, S. Tonchev, N. Faure, M. Bounhalli, S. Reynaud, and O. Parriaux. *Evidence of surface plasmon resonance in ultrafast laser-induced ripples*. Optics Express, **19**(10):9035–9043, 2011.

[GDJ04] M. E. Garcia, T. Dumitrică, and H.O. Jeschke. *Laser-induced coherent phonons in graphite and carbon nanotubes: model and simulations*. Applied Physics A, **79**(4):855-857, 2004.

[GEI+09] E. V. Golosov, V. I. Emel'yanov, A. A. Ionin, Y. R. Kolobov, S. I. A. E. Ligachev, Y. N. Novoselov, L. V. Seleznev, and D. V.Sinitsyn. *Femtosecond laser writing of subwave one-dimensional quasiperiodic nanostructures on a titanium surface*, JETP Letters, **90**(2):107-110, 2009.

[Get98] A. V. Getling. *Rayleigh-Bénard convection: structures and dynamics*. World Scientific, Singapore, 1998.

[GFS82] Z. Guosheng, P. M. Fauchet, and A. E. Siegman. *Growth of Periodic Surface Structures On Solids During Laser Illumination*. Physical Review B, **26**(10):5366, 1982.

[GIK+11] E. V. Golosov, A. A. Ionin, Y. R. Kolobov, S. I. Kudryashov, A. E. Ligachev, S. V. Makarov, Y. N. Novoselov, L. V. Seleznev, and D. V. Sinitsyn. *Formation of periodic nanostructures on aluminum surface by femtosecond laser pulses*. Nanotechnologies in Russia, **6**:237–243, 2011.

[Gra14] F. Graziani et al. (eds.). *Frontiers and Challenges in Warm Dense Matter*. Lecture Notes in Computational Science and Engineering **96**, Springer, Berlin, 2014.

[GVM+12] E. Gamaly, A. Vailionis, V. Mizeikis, W. Yange, A.Rode, and S.Juodkazis. *Warm dense matter at the bench-top:*

Fs-laser-induced confined micro-explosion. High Energy Density Physics, **8**(1):13-17, 2012.

[GX14] L. Guo, X. Xu. *Ultrafast Spectroscopy of Electron-Phonon Coupling in Gold.* Journal of Heat Transfer. **136**:122401, 2014.

[Ham04] C. R. Hammond. *The Elements*, in Handbook of Chemistry and Physics (81st ed.). CRC press, 2004.

[HCT+07] E. M. Hsu, T. H. R. Crawford, H. F. Tiedje, and H. K. Haugen. *Periodic surface structures on gallium phosphide after irradiation with 150 fs - 7 ns laser pulses at 800 nm*. Applied Physics Letters, **91**:111102, 2007.

[HDS+08] P. E. Hopkins, J. C. Duda, J. L. Salaway, R. N. and. Smoyer, and P. M. Norris. *Effects of Intra- and Interband Transitions on Electron-phonon Coupling and Electron Heat Capacity after Short-pulsed Laser Heating*. Nanoscale and Microscale Thermophysical Engineering, **12**(4):320-333, 2008.

[HG10] T. Y. Hwang and C. Guo. *Angular effects of nanostructure-covered femtosecond laser induced periodic surface structures on metals*. Journal of Applied Physics, **108**(7):073523, 2010.

[HHR+15] S. Höhm, M. Herzlieb, A. Rosenfeld, J. Krüger and J. Bonse. *Dynamics of the formation of laser-induced periodic surface structures (LIPSS) upon femtosecond two-color double-pulse irradiation of metals, semiconductors, and dielectrics*. Applied Surface Science, in Press, 2015.

[HRK+12] S. Höhm, A. Rosenfeld, J. Krüger, and J. Bonse. *Femtosecond laser-induced periodic surface structures on silica.* Journal of Applied Physics, **112**:014901, 2012.

[HSR+14] T. Hoheisel, F. Selzer, M. Riede and K. Leo. *Direct Electrical Evidence of Plasmonic Near-Field Enhancement in Small Molecule Organic Solar Cells.* The Journal of Physical Chemistry C. **118**:15128-15135, 2014.

[Hua97] Li Huang. *Semiconductors under Ultrafast Laser Excitation: Optical Studies of the Dynamics.* Harvard University, Cambridge, Massachusetts, 1997.

[HVG12]T. Y. Hwang, A. Y. Vorobyev, Chunlei Guo. *Formation of solar absorber surface on nickel with femtosecond laser irradiation.* Applied Physics A, **108**(2):299-303, 2012.

[HWG+00] J. Hohlfeld, S. S Wellershoff, J. Gudde, U. Conrad, V. Jahnke, and E. Matthias. *Electron and Lattice Dynamics Following Optical Excitation of Metals.* Chemical Physics, **251**(1–3):237–258, 2000.

[HZC+09] M. Huang, F. Zhao, Y. Cheng, N. Xu, and Z. Xu. *Origin of laser-induced near-subwavelength ripples: interference between surface plasmons and incident laser*. ACS Nano, **3**:4062–4070, 2009.

[IHW+13] E. P. Ivanova, J. Hasan, H. K. Webb, G. Gervinskas, S. Juodkazis, V. K. Truong, A. H. F. Wu, R. N. Lamb, V. Baulin, G.S. Watson, J. A. Watson, D. E. Mainwaring, R. J. Crawford. *Bactericidal activity of black silicon.* Nature Communications, **4**:2838, 2013.

[IKM+15] A. A. Ionin, S. I. Kudryashov, S. V. Makarov, N. N. Mel'nik, P. N. Saltuganov, L. V Seleznev and D. V. Sinitsyn. *Ultrafast femtosecond laser ablation of graphite*. Laser Physics Letters, **12**(7):075301, 2015.

[IZA15] N. A. Inogamov, V. V. Zhakhovsky, S. I. Ashitkov, et al. *Surface Nanodeformations Caused by Ultrashort Laser Pulse*. Engineering Failure Analysis, **47**:328-337, 2015.

[Jac75] J. D. Jackson. *Classical Electrodynamics*. Wiley & Sons, Incorporated, John, 1975.

[KCB+04] A. Khakbaznejad, B. Chehroudi, D.M. Brunette, J. Biomed. *Effects of titanium-coated micromachined grooved substrata on orienting layers of osteoblast-like cells and collagen fibers in culture*. Journal of Biomedical Materials Research Part A, **70**(2): 206-218, 2004.

[KIA+11] S. Kaneko, T. Ito, K. Akiyama, M. Yasui, C. Kato, S. Tanaka, Y. Hirabayashi, A. Mastuno, T. Nire, H. Funakubo, and M. Yoshimoto. Nano-strip grating lines self-organized by a high speed scanning CW laser. Nanotechnology, **22**:175307, 2011.

[Kok12] A. A. Kokhanovsky. *Light Scattering and Remote Sensing of Atmosphere and Surface*. Light Scattering Reviews, Vol. 6, Springer, 2012.

[KT76] Y. Kuramoto, T. Tsuzuki. *Persistent Propagation of Concentration Waves in Dissipative Media Far from Thermal Equilibrium*. Progress of Theoretical Physics, **55**(2):356-369, 1976.

[Lan11] Sébastien LANDON. Micro- and nano-processing using ultrafast lasers: all-optical enhancing. Doctor thesis. Université Jean Monnet, Saint-Etienne. France, 2011.

[LCC+16] C. Li, G. Cheng, J. P. Colombier, N. Faure, S. Reynaud, H. Zhang, D. Jamon, and R. Stoian. *Impact of evolving surface nanoscale topologies in femtosecond laser structuring of Ni-based superalloy CMSX-4*. Journal of Optics, **18**(1):015402, 2016.

[LHW+15] Z. Li, Y. Hu, T. Wen, J. Zhai, and T. Lai. *Femtosecond laser-induced crystallization of amorphous N-doped Ge8Sb92 films and in situ characterization by coherent phonon spectroscopy*. Journal of Applied Physics, **117**(13):347-352, 2015.

[LL84] L.D. Landau and E.M. Lifshitz. Electrodynamics of Continuous Media. Pergamon Press, Oxford, 1984.

[LLM03] Patrick Lorazo, Laurent J. Lewis, Michel Meunier. *Short-Pulse Laser Ablation of Solids: From Phase Explosion to Fragmentation*. Physical Review Letters. **91**(22):225502, 2003.

[LLS+05] A. M. Lindenberg, J. Larsson, K. Sokolowski-Tinten, K. J. Gaffney, C. Blome, O. Synnergren et al. Atomic-scale visualization of inertial dynamics, Science, **308**(5720):392-395, 2005.

[LM07] G. Lévêque and O. J. F. Martin. Transient behavior of surface plasmon polaritons scattered at a subwavelength groove. Physical Review B, **76**(15):155418, 2007.

[LSF88] P. R. Smith， D. H. Auston， M. C. Nuss. *Subpicosecond*

photoconducting dipole antennas. IEEE Journal of Quantum Electronics, **24**(2):255-260, 1988.

[LZC+15] C. Li, H. Zhang, G. H. Cheng, N. Faure, J.P. Colombier, D. Jamon, R. Stoian. *Initial Cumulative Effects in Femtosecond Pulsed Laser-induced Periodic Surface Structures on Bulk Metallic Glasses.* The 7th International Congress on Laser Advanced Materials, Kitakyushu, Japan, **15**:20, 2015.

[Mai07] S. A. Maier, Plasmonics: Fundamentals and Applications, Springer, Chapter 5, p65, 2007.

[Mai60] T. H. Maiman. *Stimulated optical radiation in ruby.* Nature, **187**(4736):493-494, 1960.

[MCR98] X. L. Mao, A.C. Ciocan, and R.E. Russo. *Preferential vaporization during laser ablation inductively coupled plasma atomic emission spectroscopy*. Applied Spectroscopy, **52**(7):913-918, 1998.

[MDL+14] H. Messaoudi, S.K. Das, J. Lange, F.Heinrich, S. Schrader, M. Frohme, and R. Grunwald. *Femtosecond-laser induced nanostructuring for surface enhanced Raman spectroscopy.* Proc. SPIE, **8972**:17, 2014.

[Mis12] K. Mishchik. *Ultrafast laser-induced modification of optical glasses: a spectroscopy insight into the microscopic mechanisms.* Ph.D. thiesis. Université Jean Monnet, Saint-Etienne, France, 2012.

[MJ58] N. F. Mott, and H. Jones. *The Theory of Properties of Metals and Alloys.* Dover Publications Inc., New York, 1958.

[MM08] G. Miyaji and K. Miyazaki. *Origin of periodicity in nanostructuring on thin film surfaces ablated with femtosecond laser pulses.* Optics Express, **16**(20):16265-16271, 2008.

[MMP+08] J.P. McDonald, S. Ma, T. M. Pollock, S. M. Yalisove, and J. A. Nees. *Femtosecond pulsed laser ablation dynamics and ablation morphology of nickel based superalloy CMSX-4.* Journal of Applied Physics, **103**(9):093111, 2008.

[MMT+07] S. Ma, J.P. McDonald, B. Tryon, S.M. Yalisove, T.M. Pollock. *Femtosecond Laser Ablation Regimes in a Single-Crystal Superalloy.* Metallurgical and Materials Transactions A, **38**:2349-2357, 2007.

[MNK+98] C. Momma, S. Nolte, G. Kamlage, F. von Alvensleben, and A. Tunnermann. *Beam delivery of femtosecond laser radiation by diffractive optical elements.* Applied Physics A, **67**(5):517-520, 1998.

[MR13] B. Y. Mueller and B. Rethfeld. *Relaxation dynamics in laser-excited metals under nonequilibrium conditions*. Physical Review B, **87**(3):035139, 2013.

[MSS+09] K. F. MacDonald, Z. L. Samson, M. I. Stockman and N. I. Zheludev. *Ultrafast active plasmonics.* Nature Photonics, **3**(1):55-58, 2009.

[MTA+13] R. D. Murphy, B. Torralva, D. P. Adams, and S. M. Yalisove. *Laser-induced periodic surface structure formation resulting from*

single-pulse ultrafast irradiation of au microstructures on a si substrate. Applied Physics Letters, **102**(21):211101, 2013.

[MTA+14] R. D. Murphy, B. Torralva, D. P. Adams and S. M. Yalisove. *Polarization dependent formation of femtosecond laser-induced periodic surface structures near stepped features.* Applied Physics Letters, **104**(23):231117, 2014.

[NKN71] L. V. Nomerovannaya，M. M. Kirillova，M. M. Noskov. *Optical Properties of Tungsten Monocrystals.* Soviet Journal of Experimental and Theoretical Physics, **33**(2):405-409, 1971.

[NNI16] U.S. National Nanotechnology Initiative website: http://www.nano.gov/nanotech-101/ what/manufacturing.

[OHM+10] M. Okamuro, M. Hashida, Y. Miyasaka, Y. Ikuta, S. Tokita, and S.Sakabe. *Laser fluence dependence of periodic grating structures formed on metal surfaces under femtosecond laser pulse irradiation.* Physical Review B, **82**(16):165417, 2010.

[Ojo04] M. I. Ojovan. *Glass formation in amorphous SiO2 as a percolation phase transition in a system of network defects.* Journal of Experimental and Theoretical Physics Letters, **79**(12):632–634, 2004.

[OTN+11] G. Obara, Y. Tanaka, N. N. Nedyalkov, M. Terakawa, and M. Obara. Direct observation of surface plasmon far field for regular surface ripple formation by femtosecond laser pulse irradiation of gold nanostructures on silicon substrates. Applied Physics Letters, **99**(6): 061106, 2011.

[Pal85] E. D. Palik. *Handbook of Optical Constants of Solid,* New York, Academic Press, Orlando, 1985.

[PCO+09] Y. Ping, A. A. Correa, T. Ogitsu et al. *Warm dense matter created by isochoric laser heating.* International Conference on High Energy Density Physics, Austin, United States, 2009.

[PER+91] S. Petzoldt， A.P. Elg， J. Reif， and E. Matthias. *Shockwave Detection, An Efficient Way to Determine Multiple-Pulse Damage Thresholds.* STP1117, 1990. DOI: 10.1520/STP26485S.

[PIM13] Y. Petrov, N. Inogamov, and K. Migdal. *Thermal conductivity and the electron-ion heat transfer coefficient in condensed media with a strongly excited electron subsystem,* JETP Letters, **97**(1):20-27, 2013.

[PL03] D. Perez, and L. J. Lewis. *Molecular dynamics study of ablation of solids under femtosecond laser pulses.* Physical Review B, **67**(18):184102, 2003.

[Qio16] French Qiova company website: http://www.qiova.fr.

[Rae88] H. Raether. Surface Plasmons on Smooth and Rough Surfaces and on Gratings. Springer Tracts in Modern Physics 111. New York: Springer-Verlag, 1988.

[RCB06] J. Reif, F. Costache, M. Bestehorn, Chapter 9 in Recent Advance in Laser Processing of Materials, ed. by J. Periere, E. Millon, E. Fogarassy. Elsevier, Amsterdam, p275, 2006.

[RCH+02] J. Reif, F. Costache, M. Henyk, S.V. Pandelov. *Ripples revisited: non-classical morphology at the bottom of femtosecond*

laser ablation craters in transparent dielectrics. Applied Surface Science, **197**: 891-895, 2002.

[RCZ+06] V, Recoules，J, Clérouin，G, Zérah，PM Anglade，S, Mazevet. *Effect of Intense Laser Irradiation on the Lattice Stability of Semiconductors and Metals.* Physical Review Letters, **96**(5):055503, 2006.

[RD96] L. A. Romero and F. Dickey. *Lossless laser beam shaping.* Journal of the Optical Society of America A, **13**(4):751–760, 1996.

[RDH+11] M. Rohloff, S. K. Das, S. Höhm, R. Grunwald, A. Rosenfeld, J. Krüger, and J. Bonse. *Formation of laser-induced periodic surface structures on fused silica upon multiple cross-polarized double-femtosecond-laserpulse irradiation sequences.* Journal of Applied Physics, **110**(1): 014910, 2011.

[RDS+13] S. Rapp, M. Domke, M. Schmidt, and H.P. Huber. *Physical mechanisms during fs laser ablation of thin SiO2 films.* Physics Procedia, **41**:734 – 740, 2013.

[RGN07] E. Ricci, D. Giuranno, R. Novakovic. *Density, Surface Tension, and Viscosity of CMSX-4 Superalloy.* International Journal of Thermophysics, **28**:1304–1321, 2007.

[RKC+03] C. A. D. Roeser, A. M.-T. Kim, J. P. Callan, L. Huang, E. N. Glezer, Y. Siegal, and E. Mazur. *Femtosecond time-resolved dielectric function measurements by dual-angle reflectometry.* Review of Scientific Instruments, **74**(7):3413–3422, 2003.

[RR12] A. Rosenfeld and M. Rohloff. *Formation of laser-induced periodic surface structures on fused silica upon multiple parallel polarized double-femtosecond-laser-pulse.* Applied Surface Science, **258**:9233–9236, 2012.

[RSL+02] B. Rethfeld, K. Sokolowski-Tinten, D. von der Linde, and S. I. Anisimov. *Ultrafast thermal melting of laser-excited solids by homogeneous nucleation.* Physical Review B, **65**(9):092103, 2002.

[RSL+04] B. Rethfeld, K. Sokolowski-Tinten, D. von der Linde, and S. I. Anisimov. *Timescales in the response of materials to femtosecond laser excitation.* Applied Physics A, **79**(4-6):767, 2004.

[RVV+11] J. Reif, O. Varlamova, S. Varlamov, and M. Bestehorn. *The role of asymmetric excitation in self-organized nanostructure formation upon femtosecond laser ablation.* Applied Physics A, **104**(3): 969-973, 2011.

[RZW+90] D. H. Reitze, T. R. Zhang, Wm. M. Wood, and M. C. Downer. *Two-photon spectroscopy of silicon using femtosecond pulses at above-gap frequencies.* Journal of the Optical Society of America B, 7(1): 84-89, 1990.

[San13] T. Sandu. *Eigenmode decomposition of the near-field enhancement in localized surface plasmon resonances of metallic nanoparticles.* Plasmonics, **8**:391-402, 2013.

[SBC+98] K. Sokolowski-Tinten, J. Bialkowski, A. Cavalleri, D. von der Linde,A. Oparin, J. Meyer-ter Vehn, and S.I. Anisimov. *Transient states of matter during short pulse laser ablation.* Physical Review Letters, **81**(1):224-227, 1998.

[SBJ+03] K. Sokolowski-Tinten, C. Blome, J. Blums, A. Cavalleri, C. Dietrich, A. Tarasevitch, I. Uschmann, E. Förster, M. Kammler, M. Horn-von Hoegen, and D. von der Linde. *Femtosecond x-ray measurement of coherent lattice vibrations near the Lindemann stability limit.* Nature, **422**(6929):287-289, 2003.

[SCA+14] P. K. Singh, G. Chatterjee, A. Adak, A.D. Lad, P. Brijesh, and G. R. Kumar. *Ultrafast optics of solid density plasma using multicolor probes.* Optics Express, **22**(9):22320, 2014.

[SDJ+03] B. J. Siwick, J. R. Dwyer, R. E. Jordan, and R. J. D. Miller. *An atomic-level view of melting using femtosecond electron diffraction.* Science, **302**(5649):1382-1385, 2003.

[SF86] A. E. Siegman and P. M. Fauchet. *Stimulated Wood's Anomalies On Laser-Illuminated Surfaces.* IEEE Journal of Quantum Electronics, **22**:1384 -1403, 1986.

[SHT+09] S. Sakabe, M. Hashida, S. Tokita, S. Namba, and K. Okamuro. *Mechanism for self-formation of periodic grating structures on a metal surface by a femtosecond laser pulse.* Physical Review B, **79**(3):033409, 2009.

[SHA+05] N. Sanner, N. Huot, E. Audouard, C. Larat, J.P. Huignard, and B. Loiseaux. *Programmable focal spot shaping of amplified femtosecond laser pulses.* Optics Letters, **30**(12):1479-1481, 2005.

[SHT+09] S. Sakabe, M. Hashida, S. Tokita, S. Namba, and K. Okamuro. *Mechanism for self-formation of periodic grating structures on a metal surface by a femtosecond laser pulse.* Physical Review B, **79**(3):033409, 2009.

[Siv79] G.I. Sivashinsky. *On self-turbulization of a laminar flame.* Acta Astronautica, **6**(5):569-591, 1979.

[SLV+08] Q. Sun, F. Liang, R. Vallee, and S. L. Chin. *Nanograting formation on the surface of silica glass by scanning focused femtosecond laser pulses.* Optics Letters, **33**(22):2713–2715, 2008.

[SM02] S. K. Sundaram and E. Mazur. *Inducing and probing non-thermal transitions in semiconductors using femtosecond laser pulses*, Nature Material, **1**(4): 217-224, 2002.

[SMA+96] F. Sánchez, J.L. Morenza, R. Aguiar, J.C. Delgado, and M. Varela. *Whiskerlike structure growth on silicon exposed to ArF excimer laser irradiation.* Applied Physics Letters, **69**(5):620, 1996.

[SMG+14] X. Sedao, C. Maurice, F. Garrelie, J. Colombier, S. Reynaud, R. Quey, G. Blanc, F. Pigeon. *Electron backscatter diffraction characterization of laser-inducedperiodic surface structures on nickel surface.* Applied Surface Science, **302**:114–117, 2014.

[SMP10] Koji Sugioka, Michel Meunier, Alberto Piqué (Editors). *Laser Precision Microfabrication.* Springer Series in Materials Science, Volume **135**, Chapter 4, 2010.

[SMZ+13] A. Schulze, M.F. Maitz, R. Zimmermann, B. Marquardt, M. Fischer, C. Werner, M. Went, and I. Thomas. *Permanent surface modification by electron-beam-induced grafting of hydrophilic polymers to PVDF membranes.* Rsc Advances, **3**:22518-22526, 2013.

[SNK+07] J. Schroers, T. Nguyen, S. O'Keeffe and A. Desai. *Thermoplastic forming of bulk metallic glass-Applications for MEMS and microstructure fabrication.* Materials Science and Engineering: A, **449**:898-902, 2007.

[SRH+10] Skolski J, Römer G, Huis in't Veld A, Mitko V, Obona J, Ocelik V and De Hosson. *Modeling of Laser Induced Periodic Surface Structures.* Journal of Laser Micro/Nanoengineering, **56**(3):1325–1333, 2010.

[SRO+12] J. Z. P. Skolski, G. R. B. E. Römer, J. V. Obona, V. Ocelik, A. J. Huis in't Veld, and J. Th. M. De Hosson. *Laser-induced periodic surface structures: Fingerprints of light localization.* Physical Review B, **85**(7):075320, 2012.

[SRO+13] J. Z. P. Skolski, G. R. B. E. Römer, J. V. Obona, V. Ocelik, A. J. Huis in't Veld, and J. Th. M. De Hosson. *Inhomogeneous absorption of laser radiation: Trigger of LIPSS formation.* Journal of Laser Micro/Nanoengineering, **8**(1):1-5, 2013.

[SRO+14] J. Z. P. Skolski, G. R. B. E. Römer, J. V. Obona, and A. J. Huis in't Veld. *Modeling laser-induced periodic surface structures: Finite-difference time-domain feedback simulations*. Journal of Applied Physics, **115**(10):103102, 2014.

[SSB+98] K. Sokolowski-Tinten, J. Solis, J. Bialkowski, J. Siegel, C. N. Afonso, and D. von der Linde. *Dynamics of ultrafast phase changes in amorphous GeSb films.* Physical Review Letters, **81**(17):3679-3682, 1998.

[SW79] L. Schlessinger, J. Wright. *Inverse-bremsstrahlung absorption rate in an intense laser field.* Physical Review A, **20**(5):1934-1945, 1979.

[SWC+05] M. A. Sheehy, L. Winston, J. E. Carey, C. M. Friend, and E. Mazur. *Role of the background gas in the morphology and optical properties of laser-microstructured silicon.* Chemistry of Materials, **17**:3582-3586, 2005.

[SYP+83] J. E. Sipe, J. F. Young, J. S. Preston, and H. M. van Driel. *Laser-induced periodic surface structure. I. Theory.* Physical Review B, **27**:1141–1154, 1983.

[Sze81] S. M. Sze. *Physics of Semiconductor Devices.* John Wiley & Sons, p45, 1981.

[TAN+06] M. Tsukamoto, K. Asuka, H. Nakano, M. Hashida, M. Katto, N. Abe, and M. Fujita. *Periodic microstructures produced by femtosecond laser irradiationon titanium plate.* Vacuum, **80**(11):1346–1350, 2006.

[TH05] A. Taflove and S. C. Hagness, *Computational Electrodynamics*: The Finite-Difference Time-Domain Method, 3rd ed, Artech House, Norwood, 2005.

[TNA+09] V. V. Temnov, K. Nelson, G. Armelles, A. Cebollada, T. Thomay, A. Leitenstorfer and R. Bratschitsch. *Femtosecond surface plasmon interferometry.* Optics Express, **17**(10): 8423-8432, 2009.

[VD12] M. R. S. Vincent, and J. P. Delville. *Thermocapillary migration in small-scale temperature gradients: Application to optofluidic drop*

dispensing. Physical Review E, **85**(2):026310, 2012.

[VG07] A.Y. Vorobyev and C. Guo. *Femtosecond laser structuring of titanium implants*. Applied Surface Science, **253**:7272–7280, 2007.

[VG08a] A.Y. Vorobyev, G. Chunlei. *Spectral and polarization responses of femtosecond laser-induced periodic surface structures on metals*. Journal of Applied Physics, **103**(4):043513, 2008.

[VG08b] A Y Vorobyev and C Guo. *Femtosecond laser-induced periodic surface structure formation on tungsten*. Journal of Applied Physics, **104**(6):063523, 2008.

[VG10] A. Y. Vorobyev, C. Guo. *Laser turns silicon superwicking*. Optics Express, **18**(7):6455–6460, 2010.

[VG13] A. Y. Vorobyev, C. Guo. *Femtosecond laser surface structuring technique for making human enamel and dentin surfaces superwetting*. Applied Physics B, **113**(3):423-428, 2013.

[VJL+01] F. Vidal, T. W. Johnston, S. Laville, O. Barthélemy, M. Chaker, B. Le Drogoff, J. Margot, and M. Sabsabi. *Critical-point phase separation in laser ablation of conductors*. Physical Review Letters, **86**(12):2573-2576, 2001.

[VMG07] A. Y. Vorobyev, V. S. Makin, and C. Guo. *Periodic ordering of random surface nanostructures induced by femtosecond laser pulses on metals*. Journal of Applied Physics, **101**(3):034903, 2007.

[VMG09] A. Y. Vorobyev, V. Makin, C. Guo. *Brighter Light Sources from Black Metal: Significant Increase in Emission Efficiency of Incandescent Light Sources*. Physical Review Letters, **102**(23):234301, 2009.

[VRR10] O. Varlamova, M. Ratzke, and J. Reif. *Feedback Effect on the Self-Organized Nanostructures Formation on Silicon upon Femtosecond Laser Ablation*. Solid State Phenomena, **156**:535-540, 2010.

[VRV+15] O. Varlamova, J. Reif, S. Varlamov and M. Bestehorn: "Progress in Nonlinear Nano-Optics (ed. By Sakabe, Shuji, Lienau, Christoph, Grunwald and Rüdiger), Springer, p4, 2015.

[Wan02] W. H. Wang. *Crystallization of ZrTiCuNiBe metallic glasses*. Annales de Chimie Science des Matériaux, **27**(5):99-105, 2002.

[Wan09] J. Wan. *Tunable thermal emission at infrared frequencies via tungsten gratings*. Optics Communications, **282**(8):1671-1675, 2009.

[Wan11] G. Wang. *Photonic Manufacturing Science & Technology : Overview and Outlook*. Journal of mechanical engineering, **47**(21):157-169, 2011.

[WD04] M. Weikert and F. Dausinger. *Surface structuring*, in Femtosecond Technology for Technical and Medical Applications, ed. F. Dausinger, F. Lichtner, and H. Lubatschowski, Springer-Verlag, Berlin, p117-129, 2004.

[WDS04] W. H. Wang, C. Dong, and C. H. Shek. *Bulk metallic glasses*. Materials Science and Engineering: R, **44**(2):45-89, 2004.

[WG05] J. Wang, C. Guo. *Ultrafast dynamics of femtosecond laser-induced periodic surface pattern formation on metals*. Applied Physics Letters, **87**(25):251914, 2005.

[WG07] J. Wang, C. Guo. *Numerical study of ultrafast dynamics of femtosecond laser-induced periodic surface structure formation on noble metals*. Journal of Applied Physics, **102**(5):053522, 2007.

[WG07] R. Wagner and J. Gottmann. *Sub-wavelength ripple formation on various materials induced by tightly focused femtosecond laser radiation*. J. Phys.: Conf. Ser. **59**:333–337, 2007.

[WMF+03] Q. Wu, Y. Ma, R. Fang, Y. Liao, Q. Yu, X. Chen, and K. Wang. *Femtosecond laser-induced periodic surface structure on diamond film*. Applied Physics Letters, **82**(11):1703-1705, 2003.

[WOL75] J. H. Weaver, C. G. Olson, and D. W. Lynch. *Optical properties of crystalline tungsten*. Physical Review B, **12**(4):1293-1297, 1975.

[Yee66] K. S. Yee. *Numerical solution of initial boundary value problem involving Maxwell's equations in isotropic media*. IEEE Transactions on Antennas and Propagation, **14**(3):302–307, 1966.

[YPD+83] J. F. Young, J. S. Preston, H. M. van Driel, and J. E. Sipe. *Laser-induced periodic surface structure. II. Experiments on Ge, Si, Al, and brass*. Physical Review B, **27**(2):1155–1172, 1983.

[YUK10] M. Yamaguchi, S. Ueno, R. Kuma. *Raman spectroscopic study of femtosecond laser-induced phase transformation associated with ripple formation on single-crystal SiC*. Applied Physics A, **99**(1):23–27, 2010.

[ZCF+11] W. Zhang, G. H. Cheng, Q. Feng, L. Cao, F. Wang, R. Hui. *Abrupt transition from wavelength structure to subwavelength structure in a single-crystal superalloy induced by femtosecond laser*. Applied Surface Science, **257**(9):4321-4324, 2011

[ZCF+12] W. Zhang, G. H. Cheng, Q. Feng, L. Cao. *Picosecond laser-induced formation of spikes in a single crystal superalloy*. Applied Surface Science, **258**:9452– 9456, 2012.

[ZCL+15] H. Zhang, J.P. Colombier, C. Li, N. Faure, G. Cheng, and R. Stoian. *Coherence in ultrafast laser-induced periodic surface structures*. Physical Review B, **92**(17):174109, 2015.

[ZFS82] G. S. Zhou, P. M. Fauchet, and A. E. Siegman. *Growth Of Periodic Surface Structures On Solids During Laser Illumination*. Physical Review B, **26**(10):5366, 1982.

[ZLB+16] H. Zhang, C. Li, E. Bevillon, G. Cheng, J. P. Colombier, and R. Stoian. *Ultrafast transformations of laser-irradiated tungsten*. Physical Review Letters, (In press), 2016.

[ZLZ+15] Y. Zhang, L. Liu, G. Zou, N. Chen, A. Wu, H. Bai, and Y. Zhou. *Femtosecond laser-induced phase transformations in amorphous $Cu_{77}Ni_6Sn_{10}P_7$ alloy*. Journal of Applied Physics, **117**(2):023109, 2015.

[ZMW07] Q. Z. Zhao, S. Malzer, and L. J. Wang. *Formation of subwavelength periodic structures on tungsten induced by ultrashort laser pulses*. Optics Letters, **32**(13):1932–1934, 2007.

[ZSB+08] V. Zorba, E. Stratakis, M. Barberoglou, E. Spanakis, P. Tzanetakis, C. Fotakis. *Tailoring the wetting response of silicon surfaces via fs laser structuring.* Applied Physics A, **93**(4):819, 2008.

List of publications

Publications in refereed journals

C. Li, G. Cheng, J. P. Colombier, N. Faure, S. Reynaud, H. Zhang, D. Jamon, and R. Stoian. *Impact of evolving surface nanoscale topologies in femtosecond laser structuring of Ni-based superalloy CMSX-4*, Journal of Optics, **18**(1):015402, 2016.

C. Li, G. Cheng, X. Sedao, W. Zhang, H. Zhang, N. Faure, D. Jamon, J. P. Colombier, and R. Stoian. *Scattering effects and high-spatial-frequency nanostructures on ultrafast laser irradiated surfaces of Zirconium metallic alloys with nano-scaled topographies*, Optics Express, **24**(11):11558-11568, 2016.

H. Zhang, J. P. Colombier, C. Li, N. Faure, G. Cheng, R. Stoian. *Coherence in ultrafast laser-induced periodic surface structures*, Physical Review B, **92**(17):174109，2015.

E. Bévillon, J. P. Colombier, V. Recoules, H. Zhang, C. Li, and R. Stoian. *Ultrafast switching of surface plasmonic conditions in nonplasmonic metals,* Physical Review B, **93**(16):165416, 2016.

Publications in proceedings

C. Li, H. Zhang, G. H. Cheng, N. Faure, J. P. Colombier, D. Jamon, and R. Stoian. *Initial cumulative effects in femtosecond pulsed laser-induced periodic surface structures on bulk metallic glasses*, the 7th International Congress on Laser Advanced Materials Processing (LAMP2015), Kitakyushu, Japan, 2015.

C. Li, G. Cheng, J. P. Colombier, and R. Stoian, *Femtosecond Laser-induced periodic surface structures at tight focusing at big incident angle on bulk metallic glass,* the 17th International Symposium on Laser Precision Microfabrication (Proceedings of LPM2016), in press, Xi'an, China, 2016.

H. Zhang, C. Li, J. P. Colombier, G. Cheng, and R. Stoian. *Dynamics of optically excited Tungsten and Silicon for ripples formation*, SPIE Proceedings, 93510H, Photonics West, 2015.

J. P. Colombier, E. Bévillon, H. Zhang, C. Li, X. Sedao, C. Maurice, S. Reynaud, F. Garrelie, and R. Stoian, *Dynamics of nanostructure formation on metal surfaces induced by ultrashort laser irradiation,* the 13th Conference on Laser Ablation (COLA-2015), Cairns, Australia, 2015.

Participation in conferences

LAMP2015, oral presentation, *Initial cumulative effects in femtosecond pulsed laser-induced periodic surface structures on bulk metallic glasses*, Kitakyushu, Japan, 2015.

LPM2016, poster presentation, *Femtosecond Laser-induced periodic surface structures at tight focusing at big incident angle on bulk metallic glass*, Xi'an, China, 2016.